Summer 2019

Wavelength-selective metamaterial absorber and emitter

Zhigang Li

Department: Mechanical and Aerospace Engineering

Recommended Citation

Li, Zhigang, "Wavelength-selective metamaterial absorber and emitter" (2019). *Doctoral Dissertations*. 2891.
https://scholarsmine.mst.edu/doctoral_dissertations/2891

WAVELENGTH-SELECTIVE METAMATERIAL ABSORBER AND EMITTER

by

ZHIGANG LI

A DISSERTATION

Presented to the Faculty of the Graduate School of the

MISSOURI UNIVERSITY OF SCIENCE AND TECHNOLOGY

In Partial Fulfillment of the Requirements for the Degree

DOCTOR OF PHILOSOPHY

in

MECHANICAL ENGINEERING

2019

Approved by:

Jie Gao, Advisor
Heng Pan
Xiaodong Yang
Lianyi Chen
Jie Huang

PUBLICATION DISSERTATION OPTION

This dissertation consists of the following three articles that have been published or submitted for publication as follows:

Paper I, pages 27-44 have been published in Optics Express.

Paper II, pages 45-76 have been published in Optics Express.

Paper III, pages 77-101 have been prepared to Optics Express.

Paper IV, pages 102-116 have been published in Optics Letter.

Paper V, pages 117-135 have been prepared to Optics Express.

ABSTRACT

Electromagnetic absorbers and emitters have been attracting interest in lots of fields, which are significantly revitalized because of the novel properties brought by the development of the metamaterials, the artificially designed materials. Metamaterials broadens the approaches to design the electromagnetic absorbers and emitters, making it possible to obtain the perfect absorption or emission at the wavelengths covering a wide range. Metamaterial absorbers and emitters are promising for various applications, including solar thermal-photovoltaics and thermal-photovoltaics for energy harvesting, chemical and biomedical sensors, nanoscale imaging and color printing. This work focuses on three aspects (materials, structures and design methods) to improve the experiment realizations of visible and infrared absorbers and emitters. Firstly, this work investigates simple structures based on aluminum and tungsten materials for the metamaterial absorber and emitter, which results in the realization of the all-metal visible color printing with square resonators and wavelength selective mid-infrared absorber (emitter) with cross resonators, respectively. Secondly, we explore the thermal emission properties of the quasi-periodic metal-dielectric multilayer metamaterials, which show the ability of engineering emissivity by different lattice structures. Finally, this work demonstrates the use of micro-genetic algorithm to realize efficient design and optimization for broadband metasurface absorbers, as well as wavelength-selective metasurfaces with giant circular dichroism. This work is believed to facilitate the development and application of metamaterial absorbers and emitters.

ACKNOWLEDGMENTS

Thanks for the guidance and help from Prof. Jie Gao.

Thanks for the guidance and help from Prof. Xiaodong Yang.

Thanks for the guidance and help from committee members of my Ph.D. project: Prof. Jie Huang, Porf. Lianyi Chen and Prof. Heng Pan.

Thanks for the help from the students and colleagues who have ever worked and been working in the lab, especially Lei Sun, Huixu Deng, Wei Wang.

Thanks for the help from the Professors, staffs and advisors working on campus.

Thanks for the funding organizations and departments.

Thanks for the support from my family members.

Thanks for the support from my wife.

TABLE OF CONTENTS

SECTION

PAPER

LIST OF ILLUSTRATIONS

SECTION Page

PAPER I

PAPER II

PAPER III

PAPER IV

PAPER V

LIST OF TABLES

PAPER II Page

1. INTRODUCTION

The field of electromagnetic (EM) absorber and emitter has been receiving interest for a long history, due to its intrinsic bountiful physical mechanisms and important practical applications over a wide range of frequencies, from visible and infrared range to THz and GHz in the electromagnetic spectrum shown in Figure 1.1. Electromagnetic absorber and emitter are believed to be of great interest to a vast of applications such as energy harvesting, imaging, sensor, and optical communication [1,2].

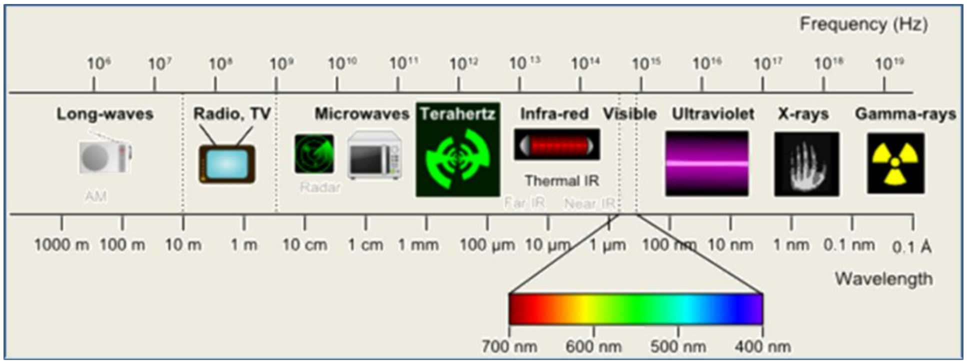

Figure 1.1. Electromagnetic spectrum from long-waves to Gama-rays [3].

The electromagnetic absorbers refers to devices selectively absorbing incident radiation with certain wavelength and then transforming into another forms of energy (e.g. ohmic heat) [2]. According to mechanism of absorption, there are generally two types of absorber: resonant absorber (narrow band) which depends on the material interaction at specific frequency and broadband absorber which depends on various methods (e.g. mixing multiple resonators, exciting phase resonance and slow light modes in the tapered anisotropic metamaterial waveguides) but not on materials frequency dependent properties [1]. The metamaterial based absorbers possessing the ability to arbitrarily design the effective permeability and permittivity with subwavelength unites are one new branch of electromagnetic absorber since 2008 [4]. Then, various metamaterial absorbers are reported towards the narrow band absorber and broad band absorber from visible and infrared range to THz and GHz [4–8]. Figure 1.2 presents the

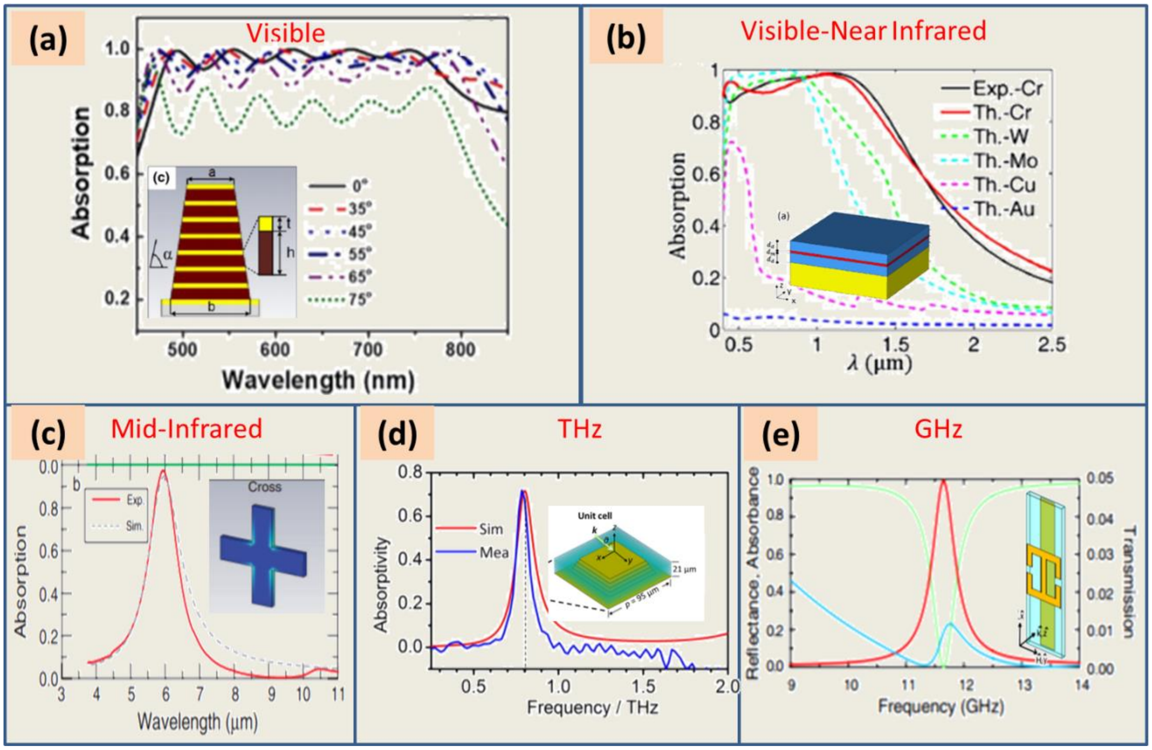

Figure 1.2. Examples of various metamaterials with excellent absorption. (a) Broadband absorption at visible range and the unit cell of the absorber with Au-Si multilayered conical frustums [8]. (b) Broadband absorption extended from visible to near-infrared range demonstrated by the planar thin film with various metals [7]. (c) Near Perfect absorption at mid-infrared range demonstrated by the Au-Al2O3-Au sandwiched layers [5]. (d) Narrowband absorption at THz demonstrated from the Cr-polymer multilayer stack [6]. (d) Perfect absorption at GHz demonstrated by the sandwiched structure of electric resonator and cut wire [4].

represented metamaterial absorbers with either narrow or broad absorption band at the wavelength range of interest.

In order to achieve a complete understanding on the EM absorbers, two aspects are reviewed in this work to fully describe the design and development of EM absorbers. One aspect is attached on the underlying mechanisms of the narrow band absorber; another aspect is focused on the mechanisms of broad band absorbers. In addition, it provides the promising applications of the EM absorbers (emitters), including the solar thermal-photovoltaics and thermal-photovoltaics, sensors, imaging and color printing.

1.1. DESIGN OF NARROWBAND ELECTROMAGNETIC ABSORBER

Narrowband EM absorbers have been studied for a long history and are used as the elementary structure to investigate the physical mechanisms of the light-material interactions. The narrowband absorption is found to be generated through numerous approaches: surface plasmon polaritons (SPPs) in metallic grating [2,9], magnetic resonance [4,10,11], ENZ/ENP [12] and MNZ [13], bandgap engineering [14–16] and other approaches (such as Inter band transition [17], phonon polaritons [18]). In this work, we focus on the former four main mechanisms. Different mechanisms are closely related with the materials and geometries of the nanostructure of the absorbers, which will be discussed in the following sections.

Surface Plasmon Polaritons (SPPs). Metallic gratings attracted people’s attention since the observation of the obvious dips in the reflection spectra in 1902, which is called Wood’s anomalies [19]. With the throughout investigations in the past years, this curious absorption is now found to be closely related with the excitation of the SPPs in the periodic structures [20]. SSPs are known as the coupling surface wave between the external incident electromagnetic wave and collective oscillation of surface charges at metal-dielectric interface [9]. Figures 1.3(a-b) schematically shows the SSPs propagating as the surface waves along the metal-dielectric interface and decaying in the direction perpendicular to the interface. The dispersion relation of the SPPs generated at the interface of non-magnetic metal and dielectric is described as $|\mathbf{k}_{\mathrm{spp}}| = (\omega/c)\sqrt{\varepsilon_1\varepsilon_2/(\varepsilon_1+\varepsilon_2)}$, where ε_1 and ε_2 denotes the permittivity function of metal and dielectric, respectively, and c represents the light speed in the free space (or air).

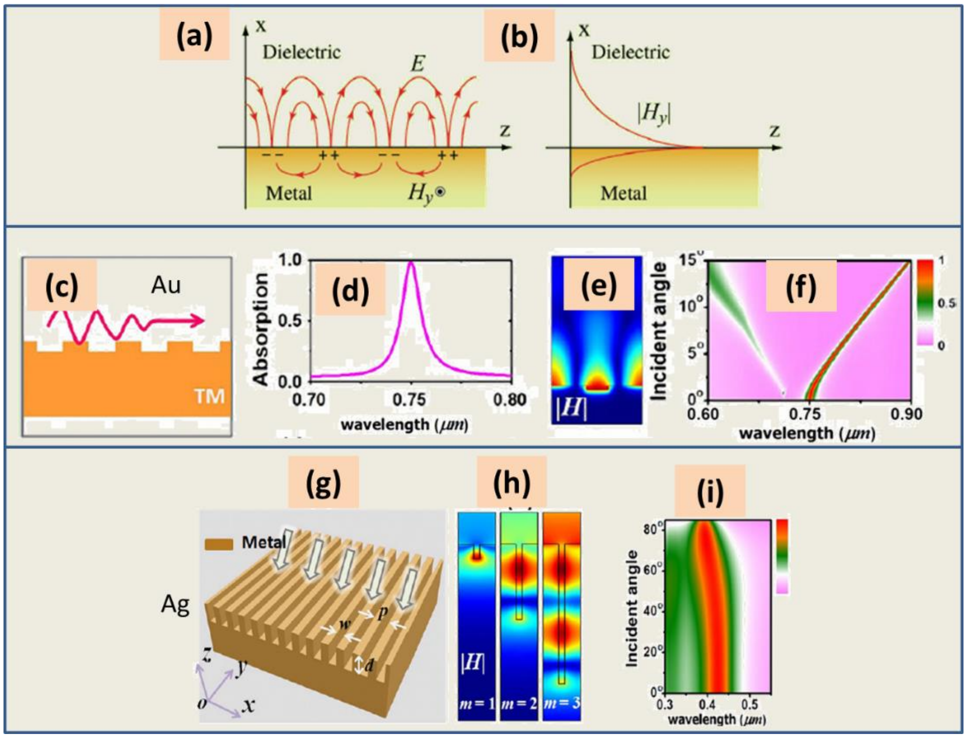

Figure 1.3. Examples of surface plasmon polaritons (SSPs). Schematic of (a) the surface SPPs excited at the interface between metal and dielectric and (b) decay of the electromagnetic filed [9]. (c) Schematic of the SPPs propagation at the periodic metallic grating. (d) Absorption spectrum with perfect absorption at 0.75 µm. (e) Magnetic field at the resonant wavelength. (e) Absorption performance with varying incident angle [2].

Due to the fact that wave vector of SPPs (k_{spp}) is almost always larger than the incident wave vector (k_{inc}) in the free space or air, SPPs are difficult to be directly excited with non-structured materials. However, SPPs are capable of trapping light in the periodic structures and are simply categorized into planar SPPs and localized SPPs according to their different behaviors in the light confinement [2]. Planar SPPs are easily excited in one dimensional metallic gratings when the momentum match condition is satisfied at a specific wavelength, namely, $\mathbf{k}_{spp} = \mathbf{k}_{||,\ inc} + \mathbf{k}_g$, where $\mathbf{k}_g$ denotes the reciprocal lattice vector of the Bloch wave in the periodic structure. In Figures 1.3(c-f), it schematically shows 1D metallic grating with the total absorption spectra under transverse magnetic (TM) polarization, as well the magnetic field distribution with the excited SPPs mode. The SPPs mode is confined in the groves and exhibits strong sensitivities with the changes of the parallel component of the incident wave vector, $\mathbf{k}_{||,\ inc}$, which is an angle dependent quantity and reads, $\mathbf{k}_{||,\ inc} = (\omega/c)\sin\theta\hat{\boldsymbol{x}}$ for SPPs only along $\hat{\boldsymbol{x}}$ direction. In contrast, metallic gratings with modified design are almost insensitive to the incident angles as the excited SPPs have light confinement for at least 2D modes. In Figures 1.3(g-i), metallic gratings with deep groves are able to confine the light and allow the SPPs propagating inside the groves, known as gap SPPs. With the waveguide theory, it supports multiple propagating modes in the deep groves, which leads to mode m=1, 2 and 3 in the magnetic field shown in Figure 1.3(h).

Magnetic Resonance. Metamaterial absorbers attract lots of interest since the first demonstration of the perfect absorption for the microwaves [4]. In Figures 1.4(a-c), it schematically shows the metamaterial absorber consisted of two parallel metal layers sandwiched with one dielectric layer. The absorber was fabricated with standard optical lithography processes and measured to perfectly absorb the electromagnetic wave at the frequency of 11.25 GHz as shown in Figure 1.4(d). The electrical ring resonator and the background metal layer support the coupling between the incident field and the circulating charges effect in the absorber. Later, this resonance is called magnetic resonance since magnetic moment resulting from surface charges with anti-parallel directions are excited in the metal-dielectric-metal (MIM) absorbers and a strong light confinement is created inside the absorber [4].

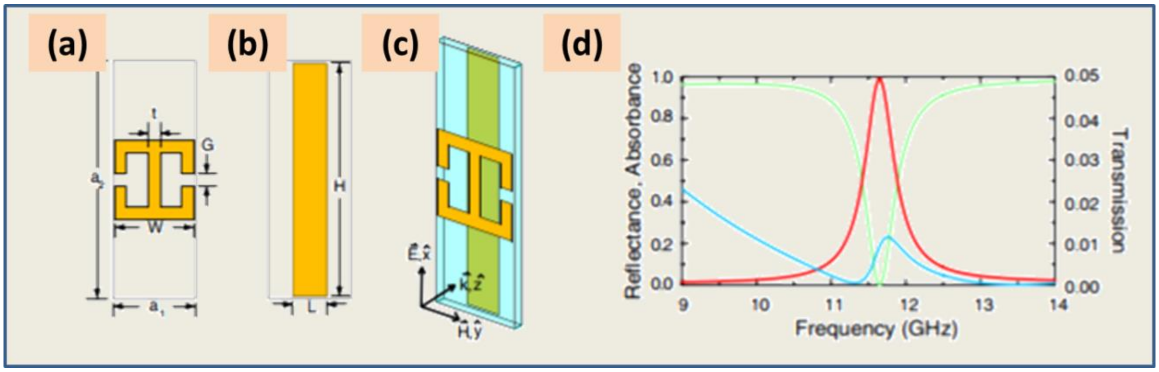

Figure 1.4. Electric resonator and its absorption. Schematic of (a) electric resonator, (b) cut wire and (c) unit cell of the absorber, which generates perfect absorption at 11.6 GHz (red line for absorption, green line for reflection, blue line for transmission) [4].

Inspired by this design, a vast of metal-dielectric-metal (MIM) absorbers are developed to achieve the perfect absorption. The top metallic layer is usually patterned to realize special absorption or polarization target. Two typical patterns, grating [10] and square [11] patch, are shown in Figure 1.5, as well as their absorption spectrum. In Figure 1.5(b), it finds the grating structure generates perfect absorption at the wavelength around 1.8 um, explained as the magnetic resonance supported by the magnetic field enhancement in Figure 1.5(c). Similarly, the metamaterial absorber with the pattern of square patch leads to the almost same perfect absorption due to the magnetic resonance. What's more, the coupled magnetic resonance is employed to understand another resonance peak. In Figure 1.5(f), it shows that two types of current loops excited and coupled to confine the incident wave.

ENZ/ENP and MNZ. There are designs of perfect absorption with narrow band using materials with epsilon-near-zero (ENZ), epsilon-near-pole (ENP) or mu-near-zero (MNZ). These designs utilize the advantages of the metamaterial by flexibly tailor the permittivity and permeability parameters.

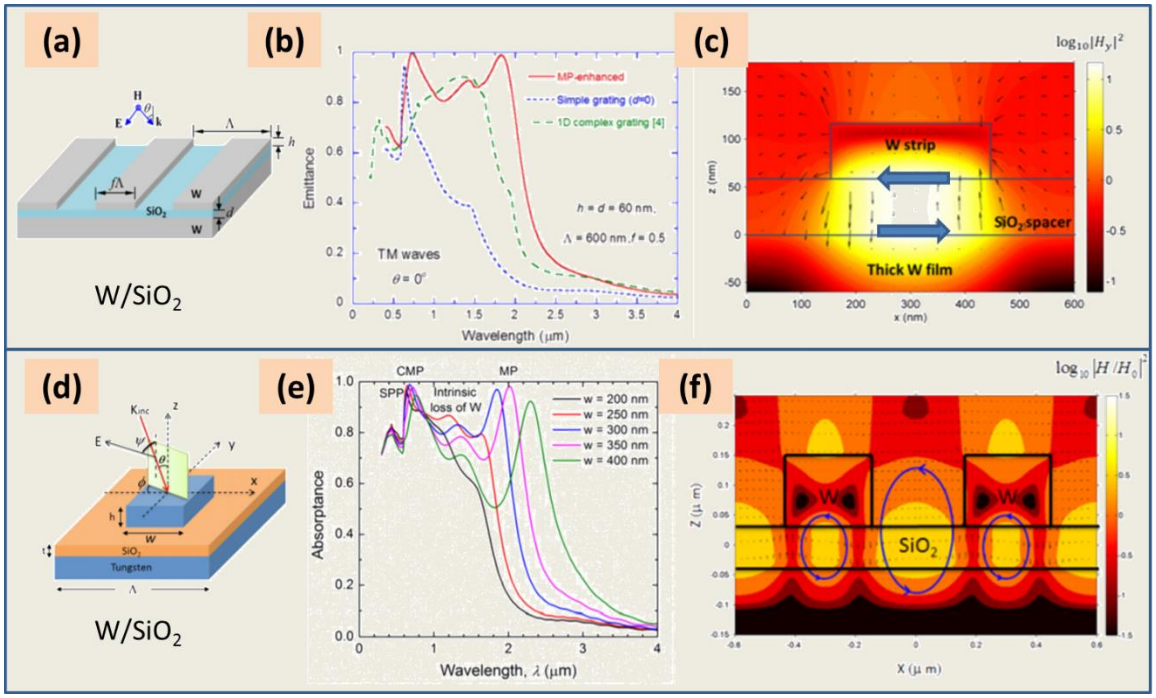

Figure 1.5. Examples of two types of gratings. Schematic of the (a) 1D tungsten grating shows (b) strong absorption in the wavelength range from visible to near-infrared, supported by (c) the magnetic resonance in the magnetic field distribution [10]. Similarly, schematic of the (d) 2D tungsten grating shows (e) strong absorption in the wavelength range from visible to near-infrared, generated by (f) the magnetic resonance in the magnetic field distribution in 2D array [11].

The 1D epsilon-near-zero (ENZ) and 2D epsilon-near-pole (ENP) metamaterials are investigated for narrowband absorbers and emitters [12]. In Figure 1.6(a), the ENZ metamaterial is realized by multilayers composed of the alternating metal and dielectric layers, whose effective permittivity can be formulated in the vertical and parallel direction by $\epsilon_{\parallel} = \epsilon_m \rho + \epsilon_D (1-\rho)$ and $\epsilon_{\perp} = \frac{\epsilon_m \epsilon_D}{\epsilon_D \rho + \epsilon_m (1-\rho)}$, where ρ is the relative fill factor of metal in the unit cell, ϵ_m is the permittivity of metal and ϵ_D is the permittivity of dielectric.. The ENZ resonance comes from the displacement field boundary condition $\epsilon_1 E_{1\perp} = \epsilon_2 E_{2\perp}$, which means if $\epsilon_2 \to 0, E_{2\perp} \to \infty$, a large electric field enhancement and perfect absorption will appear as shown in In Figure 1.6(c).

In contrast, as shown in Figure 1.6 (b), ENP metamaterial can be achieved with the nanowire embedded in the dielectric structure, whose effective permittivity is described by $\epsilon_{\parallel} = \epsilon_D [\frac{\epsilon_m (1+\rho) + \epsilon_D (1-\rho)}{\epsilon_m (1-\rho) + \epsilon_D (1+\rho}]$ and $\epsilon_{\perp} = \epsilon_m \rho + \epsilon_D (1-\rho)$, where $\rho, \epsilon_m\ \epsilon_D$ are the same notes as above. The ENP resonance comes from the condition of an ideal pole of the dielectric constant, $Re(\epsilon) \to \pm\infty$. In Figure 1.6(d), the metamaterial absorber with ENP resonance exhibits the needle like absorption with almost no sensitivities to incident angles. By comparison, ENP structure can exhibit a narrower spectral window with relatively lower material losses as compared to ENZ resonance. Basing on this theory, another calculation for the nanowire metamaterial was also realized in Reference [21]. The narrow band perfect absorption is the ideal candidate for the thermos-photovoltaic applications.

The mu-near-zero (MNZ) design is theoretically studied by assuming a thin MNZ layer with thickness d on the perfect electric conductor as substrate as shown in Figure

1.6(e) [13]. The dielectric layer and the MNZ layer are denoted as 0 and 1, respectively, as well as the permittivity and permeability symbols, By applying the boundary conditions at the interfaces and assuming a thin layer of MNZ, for normal incidence, the reflection coefficient of the absorber is approximately given by $r = \frac{1+ik_0u_{1y}d}{1-ik_0u_{1y}d}$. Therefore, the perfect absorption is achieved if $u_{1y} = i\lambda_0/(2\pi d)$, where λ_0 is the wavelength in free space. Basing on this theory, the MNZ absorber is experimentally realized with the double-layered spiral shaped rings as shown in Figure 1.6(f-h) [22]. As shown in Figure 1.6(g), the permeability curves show the characters as predicted by the previous

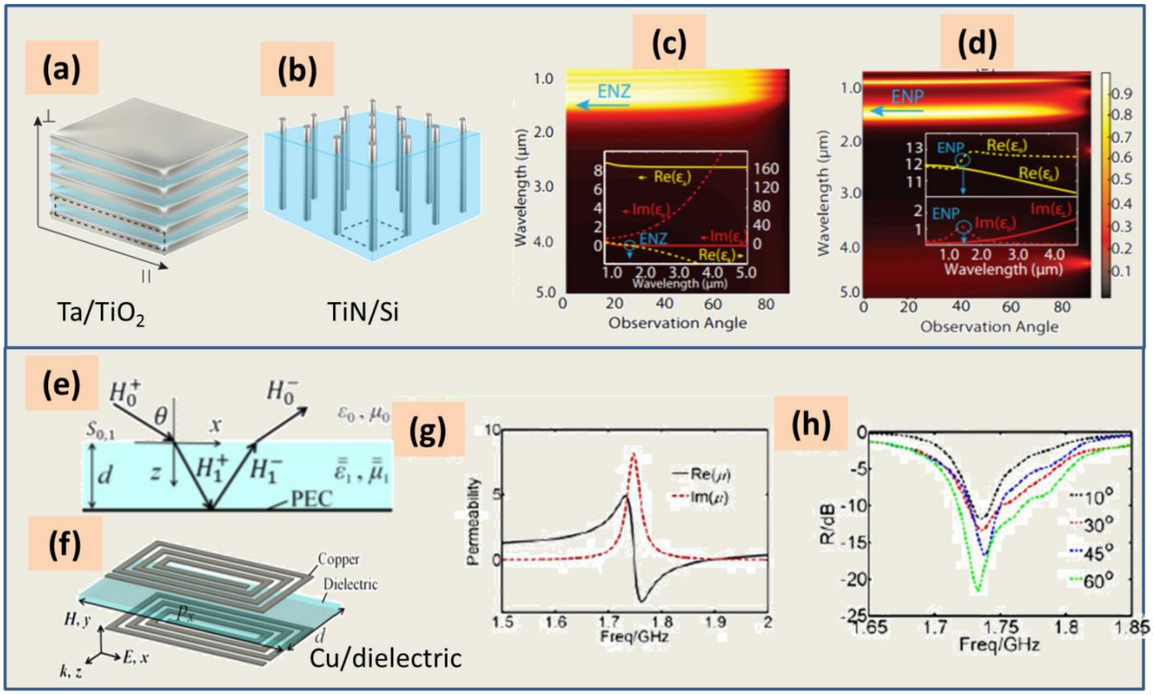

Figure 1.6. Example of ENZ and ENP metamaterial. (a) ENZ metamaterial with multilayers composed of the alternating metal and dielectric layers, showing (c) perfect absorption at the wavelength around ENZ [12]. (b) ENP metamaterial with nanowire embedded in the dielectric structure, showing (d) needle like absorption [12]. Schematic of (e-f) MNZ metamaterial with double-layered spiral shaped rings which produces the permeability curves in (g) and demonstrates (h) near perfect absorption at the frequency of 1.74 GHz [22].

theoretical analysis. MNZ is shown at the frequency of 1.74 GHz, where perfect absorption appears and exhibits insensitive to the incident angle in a wide range. What's more, combining the advantages of both ENZ and MNZ, perfect absorption can even be achieved by arbitrary thin absorber at certain incident angle for thin layer standing on the mirror substrate [13].

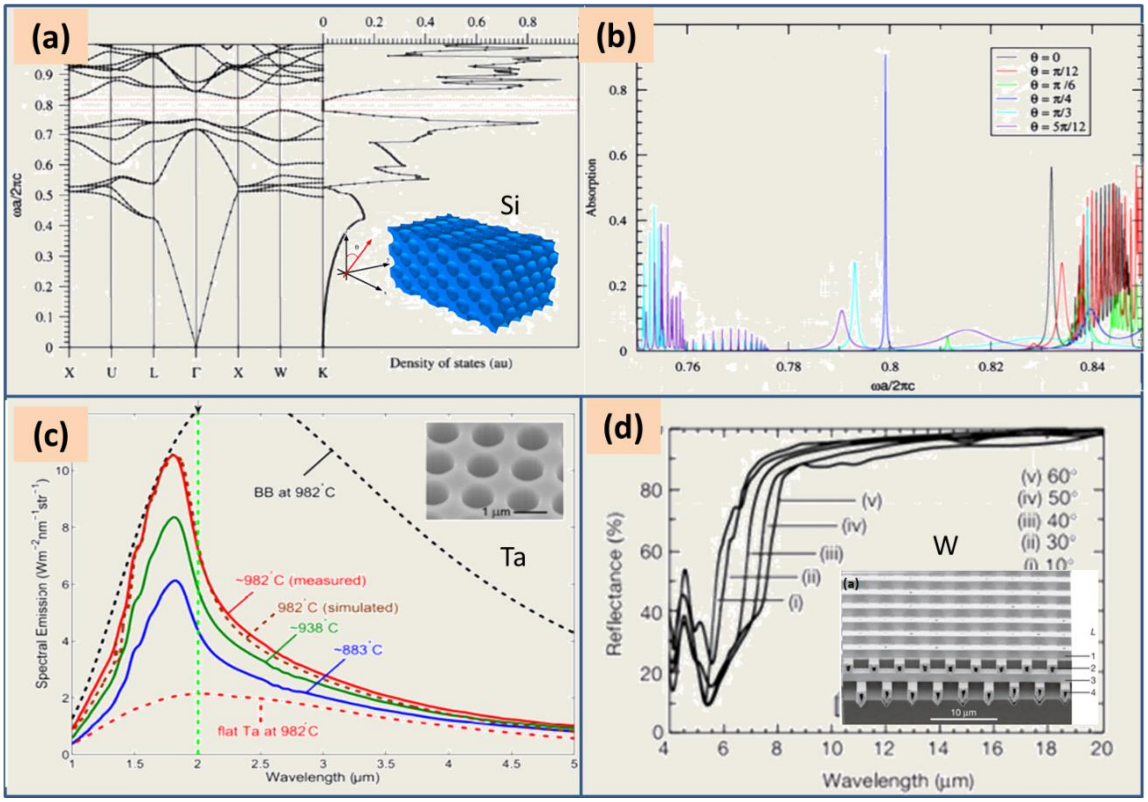

Figure 1.7. Examples of photonic crystals. (a) Band structure and density of states distribution of the 3D photonic crystal structure [16]. (b) The absorption performance of the 3D photonic structure [16]. (c) Narrowband emission at near-infrared range from the 2D photonic crystal in holes array [15]. (d) Narrowband absorption property at mid-infrared range from the 3D photonic crystal [14].

Bandgap Engineering. Photonic band-gap materials are famous for the generation of band gap for the electromagnetic wave propagating in the periodic photonic structures, which an analogy to the electronic band gap in semiconductors. Photonic band-gap materials are found to be capable of absorbing light within a narrow wavelength due to the band edge effect [14,16]. In Figure 1.7(a), it shows the band structure and corresponding density of stages (DOS) for the closed-packed FCC lattice of air spheres embedded in the silicon substrate. Sharp absorption peaks can be observed in Figure 1.7(b) for different incident angles. It is noted that a strong absorption peak at the incident angle of $45°$ appears around $\omega a/(2\pi c)=0.8$. This sharp absorption peak is generated since the group velocity ($d\omega/dk$) approaches to 0 at the Brillouin zone boundary and the number of available electromagnetic modes changed sharply as the density of states ($\rho(\omega) \propto dk/d\omega$) approaches to infinity. Thus the photonic crystals with narrow band absorption are suitable for the thermal TPV design [15], where emission equals absorption at equilibrium state according to the Kirchhoff's law (to be introduced latter) [23]. Figure 1.7(c) shows the 2D photonic crystal in holes array made of Ta, exhibiting a narrow band emission (absorption) peak with the intensity approaches to the blackbody emission limit. Similarly, in Figure 1.7(d), the design of 3D tungsten photonic crystal is also realized to be competitive in near perfect absorption performance at mid-infrared range with almost insensitivities to the incident angles [14].

1.2. DESIGN OF BROADBAND ELECTROMAGNETIC ABSORBER

Narrow band absorbers have been widely investigated and proved to be promising in lots of applications, however, the absorbers with absorption in wide wavelength range is still in need for applications such as the solar thermos-photovoltaic (TPV) system, infrared radiation energy collection, electromagnetic wave screening detections.

Investigations on the broadband absorber have explored a wide wavelength range, in which visible, near-infrared, and infrared absorbers will be introduced in this work. A vast of mechanisms are proposed to design the functional absorbers, mainly including impedance match for ultra-thin absorbers, nano-focusing of gap plasmon modes in metallic gratings, resonators mixing in 1D (vertical or horizontal direction), 2D, and 3D.

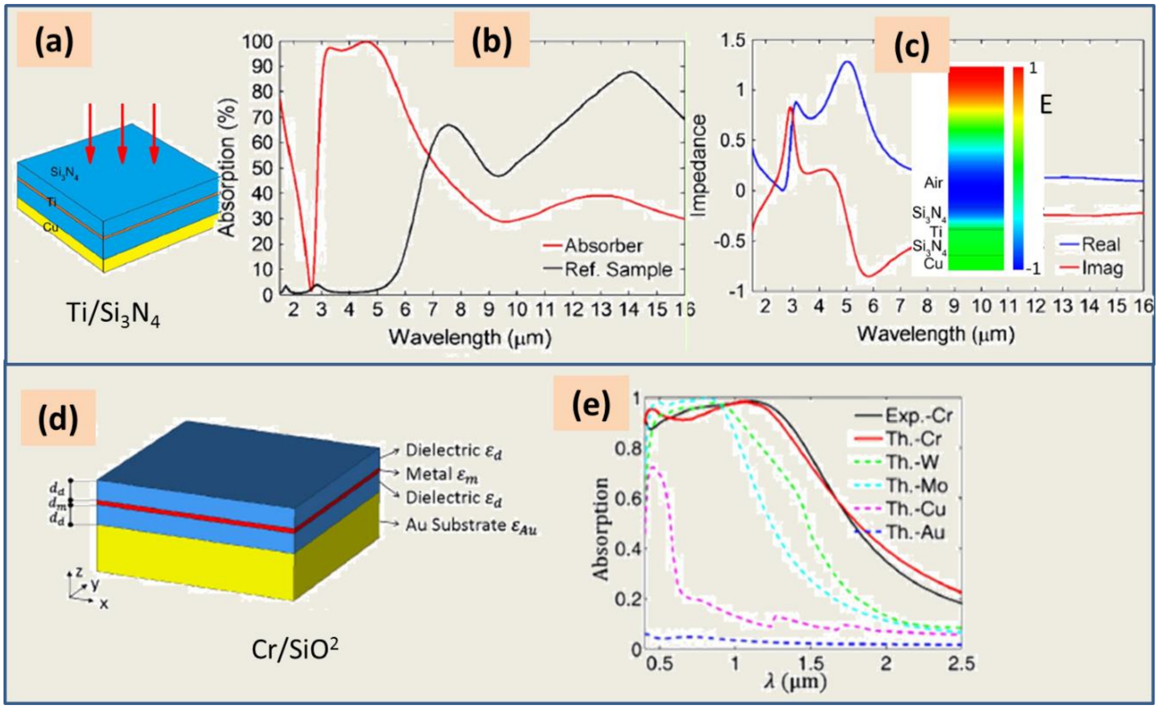

Figure 1.8. Examples of impedance matched absorbers. Schematic of (a) absorber with planar thin film, (b) operating at mid-infrared range and (c) based on the impedance match theory [24]. Illustration of (d) alternative absorber with planar thin film, (e) operating from visible to near-infrared range [7].

Ultra-thin Absorbers with Impedance Match. Among various broadband absorbers, ultra-thin absorbers are always the pursuit of researchers [7,24]. Figure 1.8(a) shows the design of thin film mid-infrared absorber made of Ti and silicon nitride (Si_3N_4) as well as a copper substrate as mirror [24]. The thicknesses of the Ti and Si_3N_4 layers are adjusted to match the impedance of the free space, such that the near perfect absorption band is realized at the range of 3-5 μm (see Figure 1.8(b)). The calculated impedance is shown in Figure 1.8(c), in which it finds that the normalized impedance is close to 1 in the region of the interest. It means the impedance of the designed absorber is close to that of the free space. This conclusion is further verified when observing the electric field distribution. The wave front of the incident light is found to keep the same propagating direction into the designed absorber with almost no signature of reflection observed from

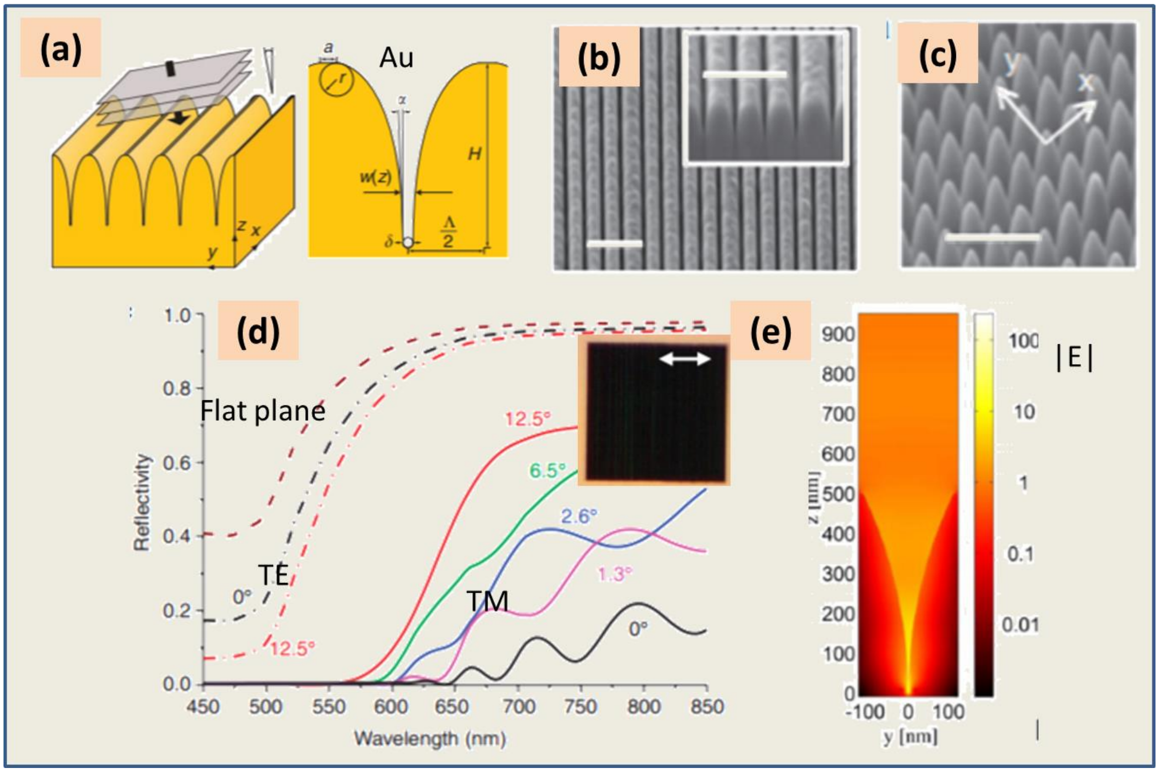

Figure 1.9. Nano-focusing of gap plasmon modes. Schematic of (a) the ultra-sharp convex grating. Fabricated samples with SEM images for (b) 1D grating and (c) 2D grating. (d) Reflectivity spectra for sample of flat plane and 1D grating under TE and TM polarization at different incident angles. (e) The electric field distribution of the ultra-sharp grating [25].

the absorber. Similarly, basing on the impedance match theory, another thin absorber with constitutes of Cr and SiO_2 is schematically shown in Figure 1.8(d) [7]. As shown in Figure 1.8(e), the designed absorber exhibits the near perfect absorption of light in the wavelength range from visible to near infrared, which is superior to other materials due to the well-designed absorber possessing impedance match property, making a near perfect absorption.

Nano-focusing of Gap Plasmon Modes in Metallic Gratings. Metallic gratings support versatile design not only in narrow band absorption but also in broadband absorption. Surface plasmon polaritons (SPPs) modes can be easily excited for periodic structures, but difficult to be absorbed into the structures. One solution is to use adiabatic nano-focusing design with ultra-sharp convex gratings as shown in Figure 1.9(a) [25]. Both 1D and 2D gratings with period of 250 nm and depth of 500 nm are fabricated in gold film and their SEM images are shown in Figures 1.9(b-c), respectively. These sharp groves are able to capture the SPPs modes which are termed as the gap SPPs because of the narrow distance between two neighbor gratings. Figure 1.9(d) shows the spectra of the 1D gratings with perfect absorption at visible range for the TM polarized normal incident light (solid line). Due to the difficulty in exciting the gap SPPs for 1D grating at TE polarization, the absorption spectra (dashed lines) shows worse absorption performance compared with TM polarization. Also, the absorption performance will degrade further for gold film with flat surface. Furthermore, in Figure 1.9(e), the electric magnitude distribution within the grooves reveals the absorption of light is due to the adiabatic nano-focusing gap SPPs mode. The incident light is almost totally confined into the groves.

Resonators mixing in 1D, 2D and 3D. Inspired by the aforementioned absorbers with narrow band absorption, the design of broadband absorbers extends to the approach of mixing resonators in different dimensions within the unit cell. The super-unit cell may contain multi-sized resonators with the same type or different types, supporting multiple resonances at different wavelengths and ultimately realizing the multi bands or broadband absorption within the target range. What's more, MIM structures are widely

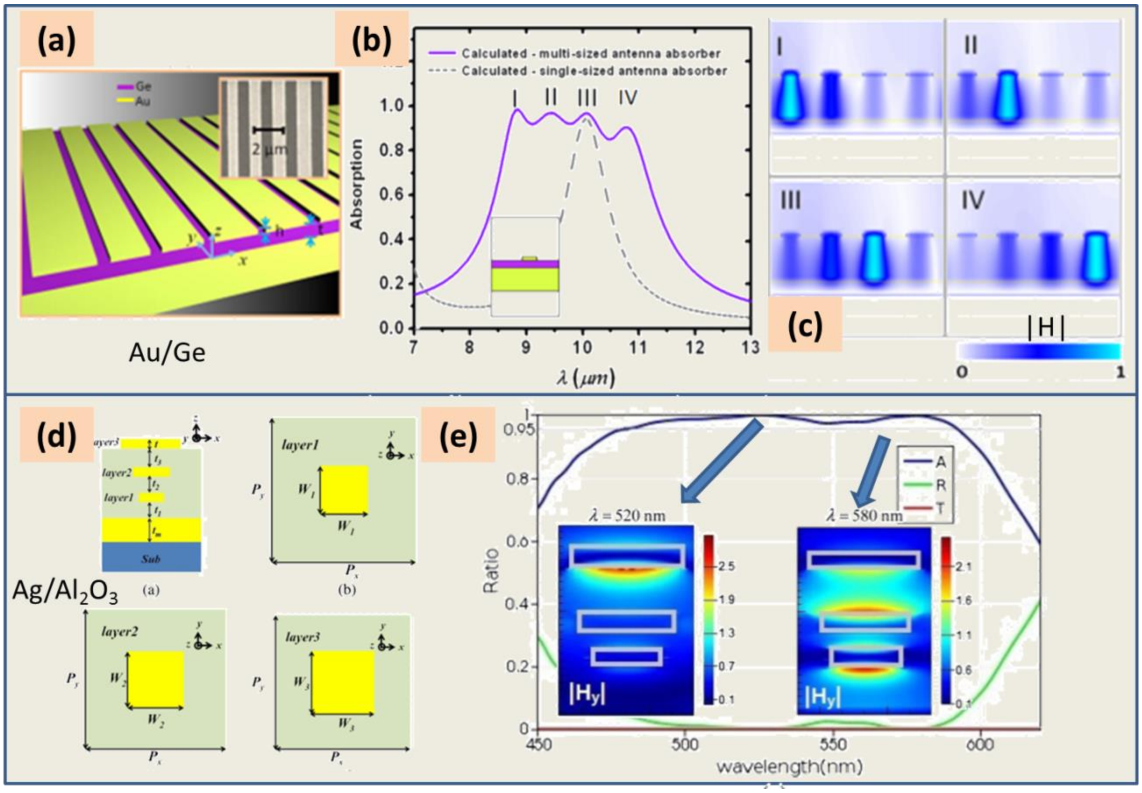

Figure 1.10. Examples of gratings with 1D and 2D structures for near perfect absorption performance. (a) Schematic of the 1D grating with multiple widths arranged in the horizontal direction and (b) the absorption spectrum with near perfect absorption, supported by the resonant electromagnetic field shown in (c) [26]. (d) Schematic of the absorber with three square patches with different sizes arranged in the horizontal direction, showing perfect absorption at visible range and the resonant electromagnetic field in (e) [27].

employed for the resonators mixing in 2D due to the simple configuration and direct patterns fabrication in the top layer as well as the interesting optical performances they are possessing.

With regard to the resonators mixing in 1D, the design with vertical or horizontal arrangement of resonators is presented in Figure 1.10 [26,27]. One super unit cell of 1D gratings with different width are shown in Figure 1.10(a) [26]. Since the width of grating is critical for the resonant wavelength, a combination of gratings with multiple widths leads to the broadband absorption if the resonant wavelengths are close to each other. Figure 1.10(b) shows the near perfect broadband absorption in the range of 8.7 -11μm. The normalized magnetic field distribution is given in Figure 1.10(c) for each resonant peak. As for the resonators arranged in the vertical direction, the absorber with three square patches with different sizes is shown in Figure 1.10(d) [27]. The corresponding absorption spectrum (blue line) with perfect broadband absorption is presented in Figure 1.10(e). The perfect absorption is mainly contributed by two resonant wavelengths, 520 nm and 580 nm, considered in the article. The absorption mechanism is explained as the localized field energy within different layers through the distribution of the magnetic field.

With regard to the resonators mixing in 2D, it allows the integration of multi-sized resonators with the same geometric type or the different types in the 2D plane within the super unit cell. Figure 1.11(a) shows the super unit cell with four square patches [28]. Since the resonant wavelength is correlated with the size of square patch, multi band absorption can be obtained through a carefully designed combination of the patches with different sizes. In Figure 1.11(b), four resonant peaks appear with strong absorption in the infrared range for both TM and TE polarizations. The magnetic field at each resonance is given in Figure 1.10(c), in which the magnetic field intensity is obviously enhanced in the corresponding square patch. As for the integration of different types of resonators, the super unit cell of mixing crosses and circles with 16 elements is schematically shown in Figure 1.11(d) [29]. The absorber with mixed cross and circle

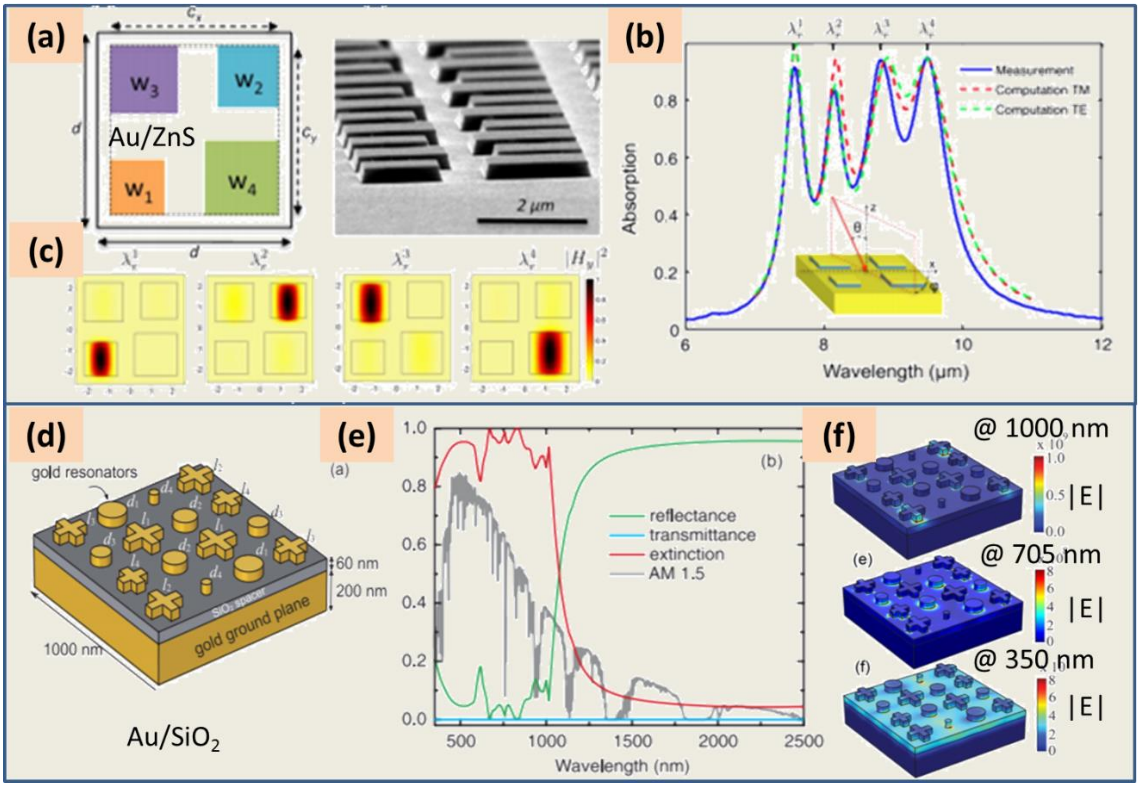

Figure 1.11. Examples of multi-sized gratings with different structures toward near perfect absorption. (a) Schematic of multi-sized resonators in the 2D plane within the super unit cell and the SEM image. (b) The multi-band absorption spectrum with four resonant peaks, supported by resonant field at each peak shown in (c) [28]. (d) Schematic of the mixed multi-sized cross and circle resonators, showing near perfect absorption from visible to near-infrared range shown in (e). The electric filed distribution at three resonant wavelengths, respectively, showing the arising of the excellent absorption performance in the optical response at three different resonance wavelength from visible to infrared. [29].

resonators leads to the near perfect absorption from visible to near infrared wavelength as observed in Figure 1.11(e), which matches well for the absorption of the nature sunlight in achieving the ideal solar energy conversion efficiency. In Figure 1.11(f), the electric field distribution at resonance is given for wavelength at 1000 nm, 705 nm and 350 nm,

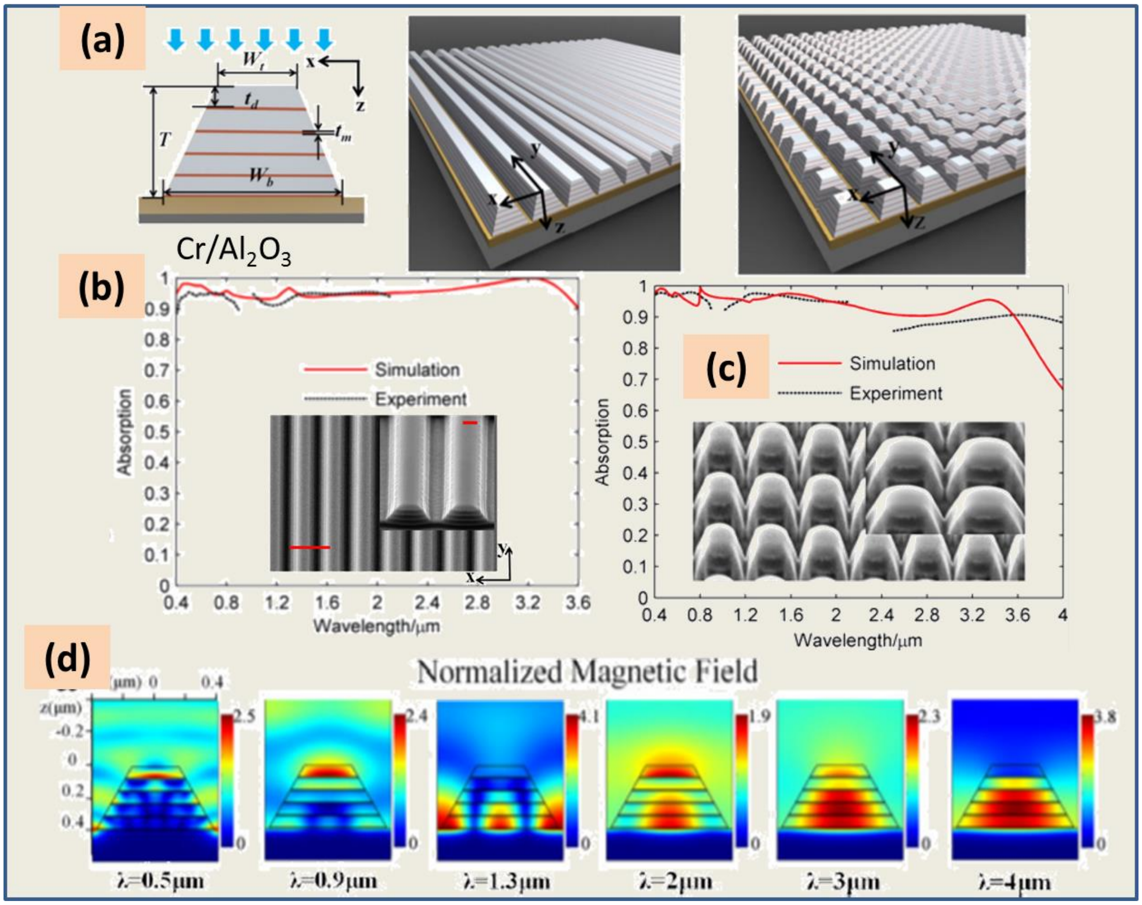

Figure 1.12. Examples of multilayered gratings. (a) Schematic of the multilayered gratings in 1D and 2D. (b) Absorption spectra obtained in experiment and simulation of the 1D grating showing near perfect absorption with the inserted SEM image. (c) Absorption spectra obtained both in experiment and simulation of the 2D grating showing the broadband absorption performance with the inserted SEM images taken at the inclined view. (d) Magnetic field distribution of the grating at different resonant wavelengths from visible to mid-infrared range plotted at the side cross section positions of the grating [30].

respectively. It reveals the variation in contribution to the absorption performance from the different resonators at the corresponding resonant wavelength.

With regard to the resonators mixing in 3D, multilayered metamaterial absorbers (or the so called anisotropic metamaterials) extend the design freedom to obtain the broadband and even ultra-broadband absorption performance [30,31]. In Figure 1.12(a), it schematically shows the multilayered gratings in 1D and 2D which are composed of 5 pairs of the alternately arranged Cr (10 nm thick) and Al_2O_3 (70 nm thick) layers [30]. The spectra of the multilayered structures are shown in Figures 1.12(b-c) for two types of gratings, respectively. It observes the near perfect absorption spectra from visible to mid-infrared range for the normally x polarized 1D multilayered grating; the similar

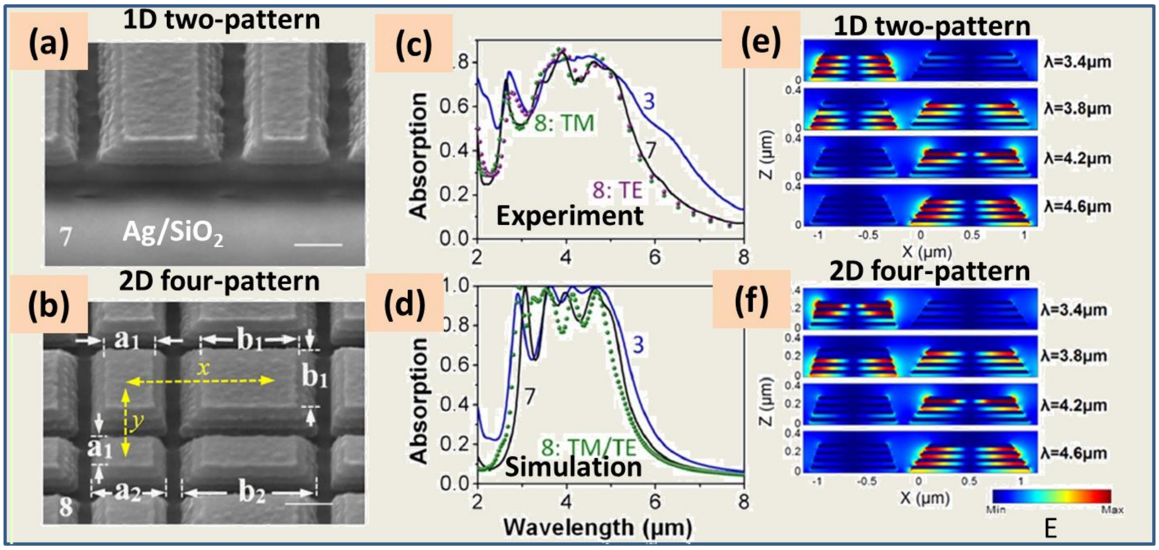

Figure 1.13. Examples of multilayered and tapered gratings. SEM images of the multilayered (a) 1D two-pattern grating and (b) 2D four-pattern grating with multiple sizes in the super unit cell. Absorption spectra obtained from (c) experiment and (d) simulation under TM and TE polarization, respectively. Electric field distribution for (e) 1D two pattern grating and (f) 2D four-pattern grating at different resonant wavelengths [31].

absorption performance is also achieved for the 2D gratings with normal incidence and arbitrary polarization. To understand the mechanism behind the broadband absorption, the normalized magnetic field is given in Figure 1.12(d). With the assumption of waveguide theory, multiple waveguide modes are allowed within the taper multilayered grating. Furthermore, the multilayered gratings with multiple sizes in the super unit cells are designed and fabricated as shown in Figures 1.13(a-b) [31]. The multilayered waveguide structures are made of four pairs of Ag and SiO_2 films with thickness of 35 nm for each layer. The experimental absorption spectra of the 1D two-pattern absorber and 2D four-pattern absorber are shown in Figure. 1.13(c) for both TM and TE polarizations. The excellent absorption performance can be observed in the mid-infrared range. The absorption spectra are also modeled and simulated in Figure 1.13(d). The electric field distribution of the cross-sectional modes is shown in Figures 1.13(e-f) for two types of absorbers, respectively. The broadband absorption is also ascribed to the guided modes supported in the taper multilayers as well as the effect of multi-sized resonators supporting the resonances at different wavelengths.

1.3. APPLICATIONS

With the ability to flexibly control the spectral behavior and electromagnetic field confinement, electromagnetic wave absorbers have been widely studied and found to be promising in a vast of applications. Four typical applications will be introduced in this work, including the full color imaging in the visible range, solar energy harvesting through visible and near-infrared range, refractive index sensing in the infrared range and spatial light modulator in the THz range. With the advantages of the novel properties from metamaterials, the traditional approaches or limits in applications can be extended or improved to a new era.

Color Imaging. In the visible range, the resolution of the printed color images is usually limited by the diffraction limit of the visible light. By assuming the center wavelength of the visible image as 500 nm, the minimum resolvable distance between two pixels is half of the center wavelength, namely, 250 nm. This limit seriously impedes the resolution improvement for traditional color printing approaches with depositing materials, for instance, dyes or quantum emitters. Recently, the color printing with plasmonic metamaterials is used to print the full color image with resolution up to the diffraction limit [32]. In Figure 1.14(a), it presents the full color image printed with 250 nm-pitch pixels formed by the MIM cavities. With tuning the diameters of the nano-disks and gap distances between two neighboring nano-disks, a wide range of colors are obtained and then utilized to print color images with an extremely high resolution. Furthermore, the high resolution color printing techniques are realized not only with the MIM structures, but also with one-step direct printing on metallic materials. With the assistance of plasmonic metamaterials, a variety of colors are achieved both in bright field and dark field, obviously extending the imaging techniques based applications [33].

Solar Energy Harvesting. Solar energy harvesting has been earning interests for a long time, since the solar energy belongs to unlimited energy stored in nature. However, energy conversion efficiency has always been an important factor preventing the utilization of the solar energy, which is given as the Shockley-Queisser limit (31%) for traditional solar cells [34]. Fortunately, the appearance of the metamaterial absorber and emitter bring the new breakthroughs to the energy conversion efficiency. A schematic of the solar cell composed of absorber and emitter is shown Figure 1.14(b) [35]. The employment of the absorber is capable of absorbing the solar energy in the range from visible to near infrared range, which takes up a larger amount of the solar energy over the electromagnetic spectrum. Through the emitter, the absorbed energy is selectively emitted into a narrow frequency range, designed to match the band gap of the semiconductors in the thermos-photovoltaic cells. Due to the existence of the absorber and emitter, the electromagnetic waves are tailored artificially to improve the performance of the solar cells, leading to the high energy conversion efficiency equaling or even beyond the Shockley-Queisser limit. What’s more, as the target frequency can be intentionally designed, heat sources can be extended to a vast of range, including high temperature frames, furnaces and even waste energies in the manufacture industries and applications.

Sensors in Refractive Index Sensing. Sensors with high sensitivity are gaining growing interest along with the sensor design using metamaterials, which are found to bring novel approaches to facilitate the sensing applications in chemicals and bio-medicals [9,36,37]. In Figure 1.14(c), it shows a typical infrared perfect absorber used as the refractive index sensing [36]. The perfect absorber employs the MIM structure with gold and MgF_2 and shows sensitivities to the environmental refractive index changes by exciting the SPPs. The experimental results show a blue shift for the resonant dips in the reflectance spectra with the increase of indices of the glucose solution. Moreover, absorber or emitters with narrow or ultra-narrow band width are also proposed to detections in the infrared range, which contains bountiful signature information for chemicals and bio-medicals.

Spatial Light Modulator. The emergence of metamaterials provides the alternative technology to shape the special distribution of electromagnetic radiation pattern. As for compressive sensing at THz range, spatial light modulator (SLM) is essentially important to manipulate and process information of electromagnetic waves [38,39]. In Figure 1.14(d), it presents the metamaterial absorbers based design of one 6 by 6 pixel array of

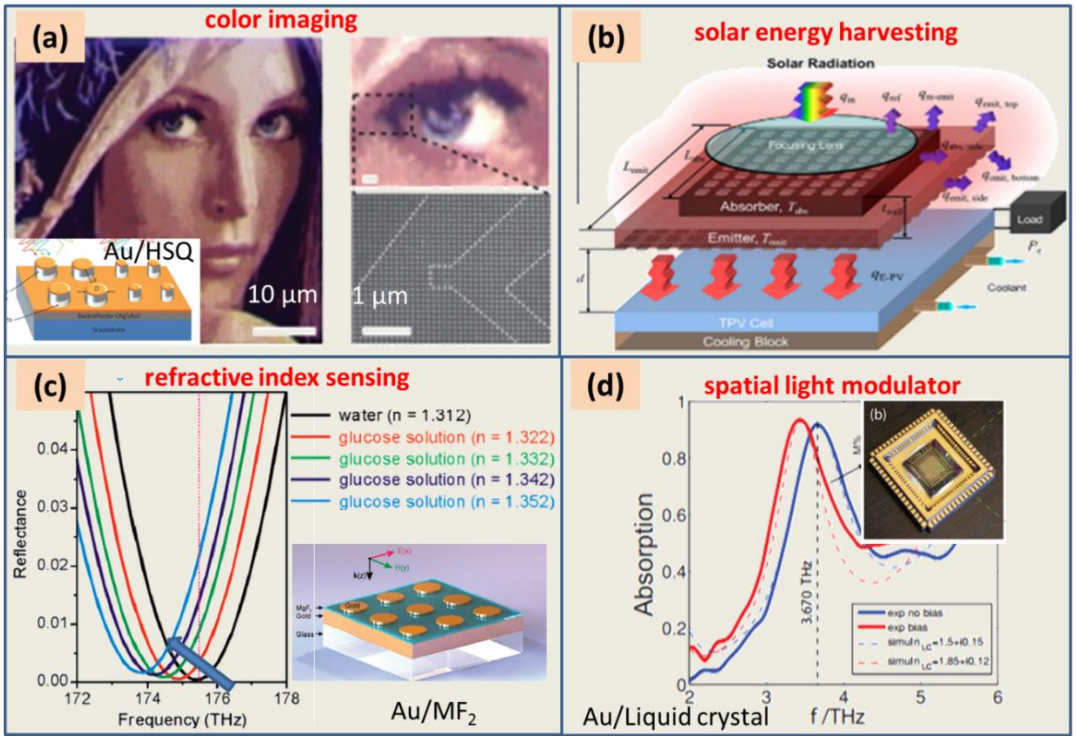

Figure 1.14. Examples of applications. (a) Full color image with resolution up to the diffraction limit through printed plasmonic metamaterial. It also shows the schematic of the nano-disk structure and the SEM image [32]. (b) Schematic of the solar energy harvesting system design with metamaterial absorber and emitter [35]. (c) Metal-dielctric-metal metamaterial absorber designed for refractive index sensing [36]. (d) Spatial light modulator realized with near perfect absorber at THz range [39].

SLM, which is allowed to be electronically manipulated because of the employment of the liquid crystals [39]. The refractive index of the liquid crystals will significantly influence the absorption behaviors or the designed structure and hence leads to resonance shift as shown in Figure 1.14(d). It can result in the redshift if the SLM is loaded with certain bias. In addition, with the ability to control the electromagnetic filed dynamically, SLM is also promising in numerous applications such as spectroscopy and imaging [38].

1.4. RESEARCH OBJECTIVE

Although EM absorbers (emitters) have been widely studied, there are still some spaces to improve, such as the structure design, materials section and mechanism understanding in specific situations. Thanks to the rapid development in the field of metamaterials, new designs are allowed to be realized with modifying the geometry and hence the effective permittivity and permeability of the materials. The unprecedented electromagnetic properties, beyond the nature materials, can be achieved with metamaterials. Therefore, this work focuses on three aspects: (1) the simple structure design with aluminum and tungsten materials for the metamaterial absorbers and emitters through periodic structures, (2) engineering the thermal emission properties via the quasi-periodic metal-dielectric multilayer metamaterials, (3) improve the design method beyond the traditional design method toward broadband metasurface absorber and metasurface with giant circular dichroism by the micro genetic algorithm.

Simple structure design to realize the expected electromagnetic property is always attractive, not only in explaining the underlying physical mechanism, but also in industrial applications for large scale production. For applications in the industry, it needs a balance between the complexities in structure design and the final properties. Also, simple structure design can be more competitive due to a short period in fabrication and relatively low requirement in fabrication precision. In addition, suitable materials are determined for specific applications in most situations. Noble metals (such as Au, Ag) are prevailing in the metamaterials design, however, more chemical and temperature stable and less expensive materials are favored for real applications with requirement of high temperature environment or large-scale production.

The properties of periodic metamaterials have been widely investigated, however, the quasi-periodic metamaterials are still worthy of more attentions due to their similar but novel properties in some extent. Quasi-periodic metamaterials are appealing to be used for tailoring the electromagnetic properties since the specific arrangement of the geometries are able to generate special interference and interactions with materials different from the periodic situations. It provides alternative approaches to the design of the metamaterial absorber and emitter.

The last but not the least attention focuses on the design method. In traditional design of metamaterial absorber and emitters, it initializes the design progress with the experience of researchers and follows by sweeping the parameters step by step using repeated attempts. Though the traditional design will finally generate the design result, it is obvious to see the limitations. It is not only less efficient in design progress, but also easily to be misled or miss the optimal design. Thus, the optimization method with efficiency is attractive in metamaterial design.

In conclusion, this work will investigate the design of metamaterial absorber and emitter both in theory and experiment. The simple structure with aluminum and tungsten materials will be developed for specific application in color imaging and energy harvesting. Also, this work will conduct the comparison between the periodic and quasi-periodic metal-dielectric multilayer metamaterials, as well as the development of the efficient design method of metamaterials using micro genetic algorithm for the geometric optimization, which will facilitate the development and promising applications in the field of metamaterials.

PAPER

I. ALL-METAL STRUCTURAL COLOR PRINTING BASED ON ALUMINUM PLASMONIC METASURFACES

Zhigang Li,[1,†] Wei Wang,[1,†] Daniel Rosenmann,[2] David A. Czaplewski,[2]
XiaodongYang,[1,3] and Jie Gao [1,*]

[1]Department of Mechanical and Aerospace Engineering, Missouri University of Scienceand Technology, Rolla, MO 65409, USA

[2]Center for Nanoscale Materials, Argonne National Laboratory, Argonne, IL 60439, USA. [†]These authors contributed equally to this work.

ABSTRACT

An all-metal structural color printing platform based on aluminum plasmonic metasurfaces is proposed and demonstrated with high color performance using only one-step etching process on aluminum surface. A wide visible color range is realized with the designed metallic square-shaped disk arrays by simply adjusting geometrical parameters of the disk etching depth, disk width and unit cell period. The demonstrated all-metal microscale structural color printing on aluminum surface offers great potential for many practical color related applications.

1. INTRODUCTION

Over the past decade, different kinds of structural color filtering and printing techniques have been used to reproduce vivid colors in nature with great advantages over conventional colorant-based pigmentation [1-3]. In particular, plasmonic metamaterials and metasurfaces are receiving more attention for the next generation structural color applications due to their capability of controlling the light intensity, phase and polarization effectively [41–45]. Plasmonic nanostructures with various geometries have been developed for structural color generation with high resolution including one dimensional gratings [46–48], hole arrays [49–53], nanoantenna arrays [54–58], metal-insulator-metal (MIM) structures [10, 22–27], and combined nanodisk and nanohole arrays [65–67]. By tuning the geometries and dimensions of the plasmonic nanostructures, optical resonances in the visible frequency range can be achieved based on the mechanisms of propagating surface plasmons (SP) [12–16], localized surface plasmon resonances (LSPR) [18, 28–33], as well as Fabry-Pérot cavity modes [71]. Plasmonic color generation has been widely studied in realizing highly saturated color with narrow bandwidth [23, 25-27], color filtering with extraordinary optical transmission [35–37], high-resolution color pixels for imaging [10, 28, 34], polarization dependent [16, 17] or independent [18, 20, 21] color filtering and imaging, and angle-insensitive structural color printing [21, 34]. Noble metals like gold and silver have been traditionally employed in the color filtering and imaging platforms due to their lower ohmic losses within the visible spectrum [10, 18, 24, 25, 28, 34, 38]. However, the interband transition of gold limits the color range obtainable to below the wavelength of 550 nm [24,39], while silver is susceptible to oxidation and sulfidation which leads to the degradation of colors under ambient usage [55]. Consequently, a suitable substitute for noble metals, aluminum, has been highly attractive for structural color printing application due to its excellent optical response in the visible spectrum, chemical and thermal stability thanks to its natively formed oxidation layer, low cost, and complementary metal oxide semiconductor (CMOS) compatibility [15, 16, 20, 26, 27, 40]. Recently, aluminum based metamaterials with complex nanostructures such as MIM structures [10, 22–27] and combined nanodisk and nanohole arrays [65–67] have been designed to exhibit excellent color performance, however, the fabrication processes are still sophisticated, which will not only increase the production cost but degrade the color performance due to fabrication imperfections.

In this work, we introduce and demonstrate an all-metal structural color printing platform based on aluminum plasmonic metasurfaces with high color performance using a simple, one-step focused ion beam milling process on aluminum surface. By adjusting the geometrical parameters of the designed aluminum square-shaped disk arrays, including the disk etching depth, disk width and unit cell period, a wide visible color range can be realized. The mechanism of structural color generation in aluminum square-shaped disk arrays is analyzed according to the excitation of electric dipole and magnetic dipole resonances. Furthermore, the polarization and incident angle dependent optical properties of the color printing platform have also been studied. The demonstrated all-metal structural color printing on aluminum surface offers great potential for many relevant applications such as microscale imaging, information storage, and security marking.

2. DEVICE DESIGN AND FABRICATION

The square-shaped disk array on aluminum surface designed for plasmonic structural color printing is schematically illustrated in Figure 1(a). In order to vary the optical response of the designed disk arrays in the visible spectrum, the geometrical parameters of the disk etching depth (*d*), disk width (*w*) and the unit cell period (*P*) are tuned. First, a 250 nm thick aluminum layer is deposited on a silicon wafer using an electron-beam evaporator at a rate of 12 Å/sec. Then the designed disk arrays are directly milled into the aluminum layer using a focused ion beam (FIB) milling process (FEI Helios Nanolab 600 DualBeam) with a gallium ion current of 9.7 pA and an accelerating

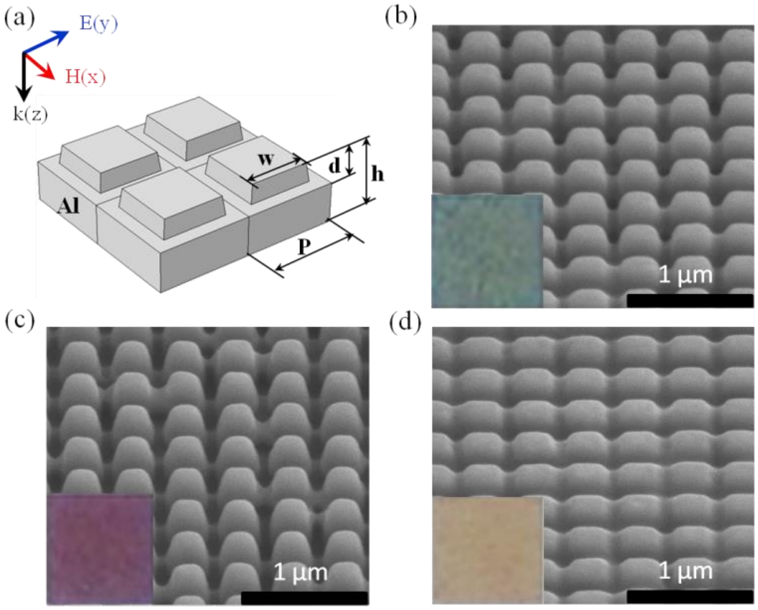

Figure 1. Design of the square-shaped disk array. (a) Schematic of the design. (b-d) SEM images of the design fabricated on h = 250 nm thick aluminum film with different geometric parameters of (b) P = 400 nm, d = 135 nm, w = 245 nm, (c) P = 400 nm, d = 227 nm, w = 200 nm, and (d) P = 400 nm, d = 82 nm, w = 245 nm. Insets: Optical reflection microscope images of 20 × 20 μm^2 disk arrays. Scale bars: 1 µm.

voltage of 30 KeV. In order to investigate the effects from geometrical parameters, three groups of disk arrays are fabricated with varying *d*, *w* and *P*, respectively. It is noted that the obtained unit cell period during the ion beam milling process is always consistent with the design, while the etching depth and disk width experience slight deviations from the designed values but still in a reasonable range with ±15 nm variation. After the ion beam milling process, as shown in Figures 1(b)-1(d), the top width of the square disk is smaller than the bottom width and thus there is a tapered angle of 83º for the disk sidewall. Optical transmission of the designed structure will be effectively blocked due to the limited penetration depth in the thick aluminum layer for incident light in the visible range.

3. RESULTS OF EXPERIMENTAL CHARACTERIZATION AND NUMERICAL SIMULATION

The optical reflection spectra from the fabricated square-shaped disk arrays are characterized within the visible range (400 ~ 800 nm) by utilizing an optical spectrometer (LR1, ASEQ instruments). Optical reflection spectrum and the corresponding optical reflection microscope image are collected in the bright field from each fabricated disk array with an area of 20 × 20 μm^2. Figures 1(b)-1(d) show SEM images of three representative disk arrays with different geometrical parameters. The insets display the measured bright-field optical microscope images of these disk arrays, showing three prime colors belonging to the Cyan-Magenta-Yellow (CMY) color model, a standard model to describe colors.

The effects of varying disk etching depth *d*, disk width *w* and unit cell period *P* for the square-shaped disk arrays on the optical reflection spectra and visible colors are further investigated. The measured optical reflection spectra and bright-field microscope

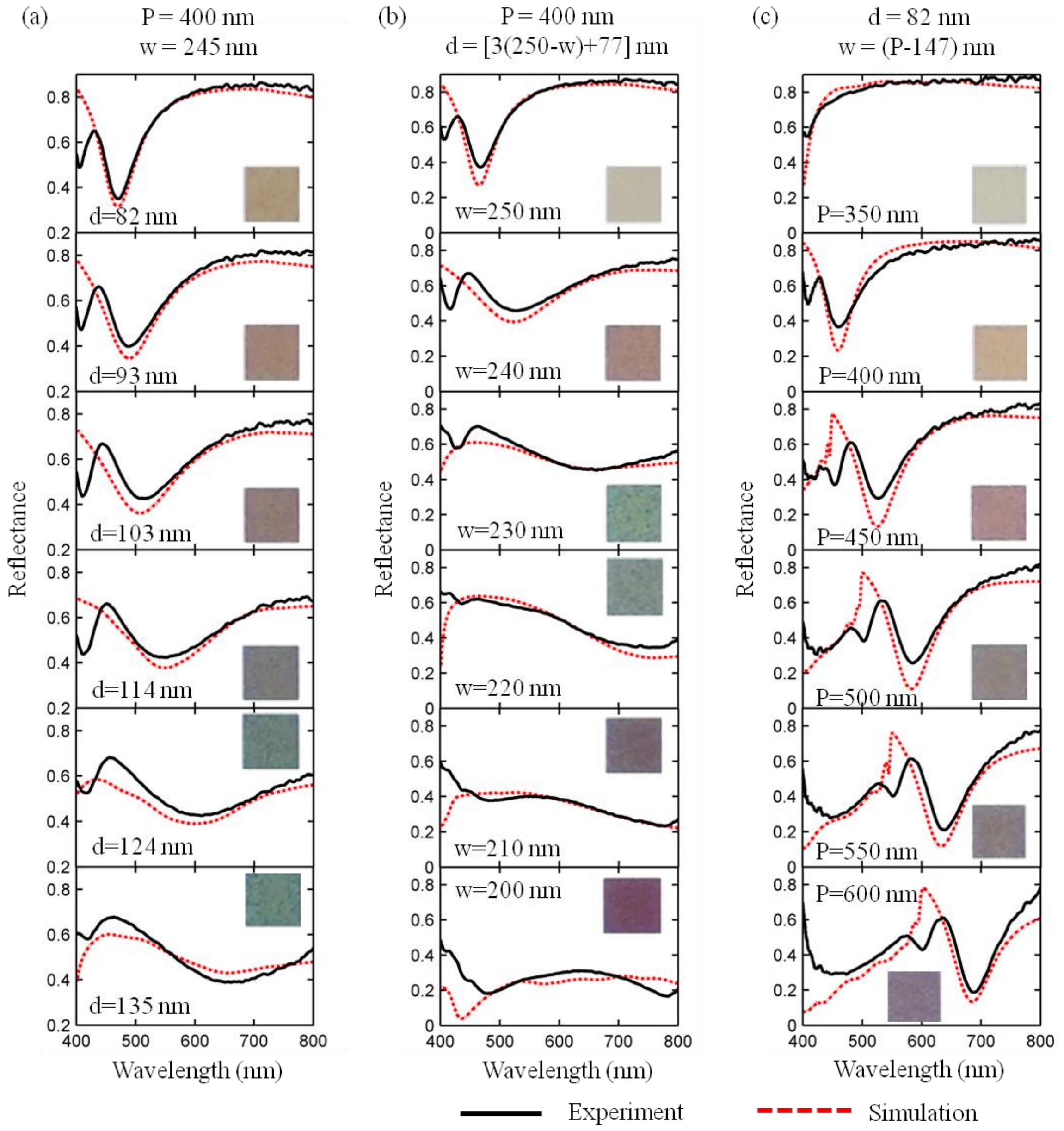

Figure 2. Measured and simulated reflection spectra. (a) Spectra of three groups of disk array samples by varying disk etching depth *d* from 82 nm to 135 nm with constant *P* = 400 nm and *w* = 245 nm, (b) by changing disk width *w* from 250 nm to 200 nm with constant *P* = 400 nm and *d* as a function of *w*, and (c) by changing period *P* from 350 nm to 600 nm with constant *d* = 82 nm and *P* - *w* = 147 nm. Insets show the optical reflection microscope images of 20 × 20 μm^2 disk arrays. Normal light incidence is employed.

images for three groups of disk arrays with varying *d*, *w* and *P* are shown in Figure 2. In Figure 2(a), the measured and simulated reflection spectra for disk arrays with varying *d* exhibit a red-shifted plasmonic resonance and a broader resonance dip as *d* is increased from 82 nm to 135 nm while w = 245 nm and P = 400 nm are constant. The colors of the microscope images also change accordingly. As shown in Figure 2(b), a similar optical response is observed for disk arrays with reduced *w* from 250 nm to 200 nm and constant P = 400 nm. It is noted that *d* will depend on *w* during the FIB process due to the variation of ion beam exposure area, giving a rough expression of $d = [3(250\text{-}w)+77]$ nm. Especially for the w = 200 nm case, a broad absorption band is obtained due to both the aluminum loss in the visible spectrum [17, 30, 40, 41] and the excitation of gap plasmon modes [42, 43]. It is indicated that the obtained visible color range is dependent on both disk etching depth *d* and disk width *w* with a constant unit cell period *P*. Moreover, a wider range of color can be realized with simultaneous variation of both *d* and *w*. In addition, Figure 2(c) displays the results for disk arrays with varying *P* from 350 nm to 600 nm and $w = (P\ \text{-}147)$ nm at a constant d = 82 nm. As both *P* and *w* are increased, the plasmonic resonance gets red-shifted. Numerical simulation results from the Finite Element Method (COMSOL Multiphysics) are also shown in Figure 2. The geometrical parameters of square-shaped disk arrays used in simulation are measured from the SEM images. A good match between the experimental and simulation results can be found in Figure 2. In order to understand the relationship between optical reflection spectra and color generation, all the experimental and simulated reflection spectra depicted in Figures 2(a)-2(c) have been converted as the discrete points in the CIE 1931 xy chromaticity coordinates based on color theory [44] in Figures 3(a)-3(c), respectively. As the geometrical parameters of *d*, *w* and *P* for disk arrays vary, the chromaticity coordinates evolve in a clockwise fashion close to the achromatic point, demonstrating the capability of aluminum metasurfaces to produce a relative large degree of visible color range tuning.

In order to understand the mechanism of the plasmonic resonance for the square-shaped disk array, optical field distributions at the resonance wavelength of 546 nm are analyzed for one selected sample with *P* = 400 nm, *w* = 245 nm and *d* = 114 nm. As shown in Figure 4(a), the time-averaged magnetic field (color map) and electric displacement (red arrows) distributions in the *y*-*z* cross section of the designed disk array indicate a strong magnetic dipole resonance [45–47] with enhanced magnetic field concentrated within the air trench surrounded by three aluminum-air interfaces due to the anti-symmetric current flow. At the same time, an electric dipole resonance is also

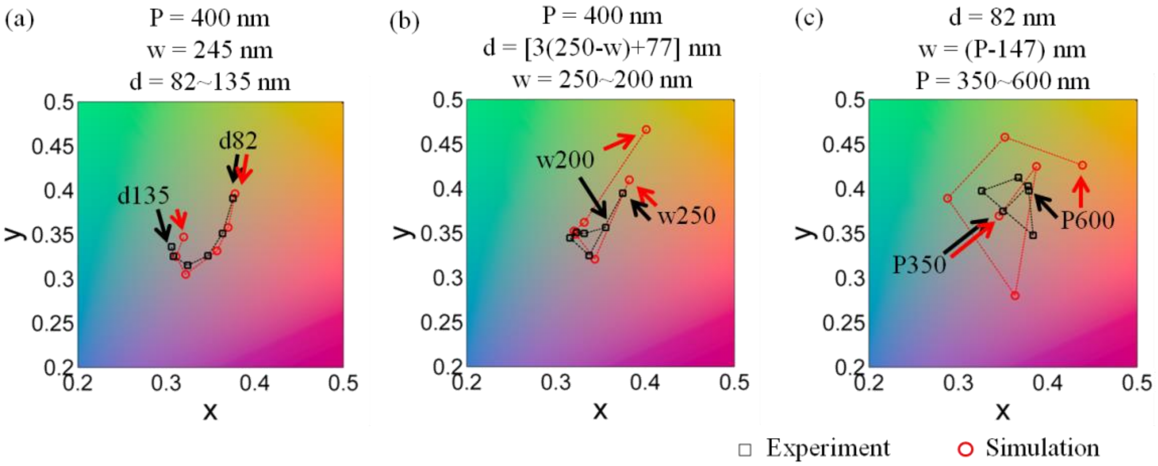

Figure 3. Measured (black square) and simulated (red circle) results in the CIE 1931 xy chromaticity coordinates. Results for three groups of disk array samples by changing (a) d, (b) w, and (c) P. The reflection spectrum data are obtained from Figures 2(a)-2(c). The beginning and ending points of parameter variations are labeled for each case.

formed on the top aluminum-air interface of the disk. The time-averaged optical power flow distribution in Figure 4(b) depicts the penetration of light into the aluminum surface layer. The excitation of resonant plasmonic modes will lead to the strong optical absorption for incident light at certain wavelength so that the subtractive color can be observed in the reflection from the disk array sample. A variety of colors are presented with the corresponding reflection spectra.

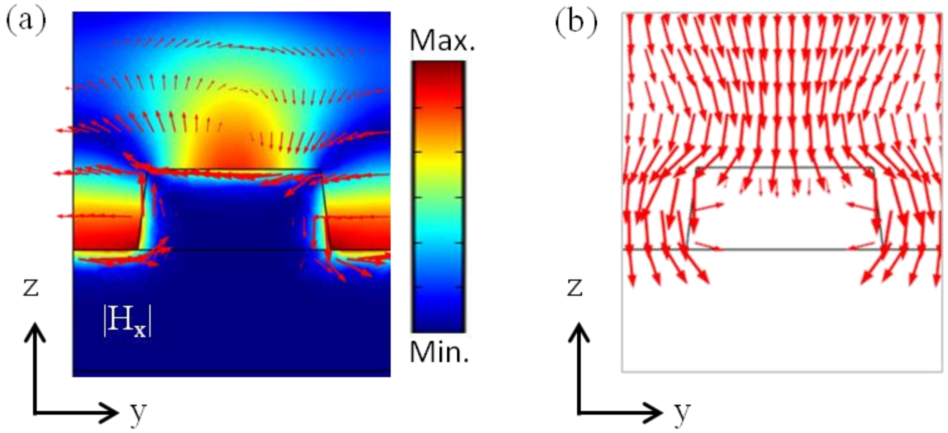

Figure 4. Mode analysis of the resonator. (a) Cross section of the time-averaged magnetic field (color map) and electric displacement (red arrows) distributions for a selected disk array (with *P* = 400 nm, *w* = 245 nm and *d* = 114 nm) at the resonance wavelength. (b) Cross section of the time-averaged optical power flow vector distribution.

The designed square-shaped disk arrays on aluminum surface can exhibit various visible colors. In Figure 5, the bright-field microscope images of two color palettes are displayed, where subtractive structural colors are generated from disk arrays with varying geometrical parameters in disk etching depth *d*, disk width *w* and unit cell period *P*. The color palette in Figure 5(a) includes the disk arrays with constant *P* = 400 nm but varying *w* and *d*, where the dimensions are measured from the SEM images. While the color palette in Figure 5 (b) has the disk arrays with a certain *P* in each row changing from 360 nm to 500 nm and varying *w* and *d*. An etching depth beyond the total thickness of the aluminum layer is also obtained experimentally, forming an aluminum-silicon two-layer post array on the silicon substrate. The absorption of incident light is further enhanced by the plasmonic resonance from the two-layer post as well as the optical loss in the silicon substrate. As a result, dark colors can be realized at the upper-right corner of the color palette in Figure 5(a) and the right columns of the color palette in Figure 5(b). The wide

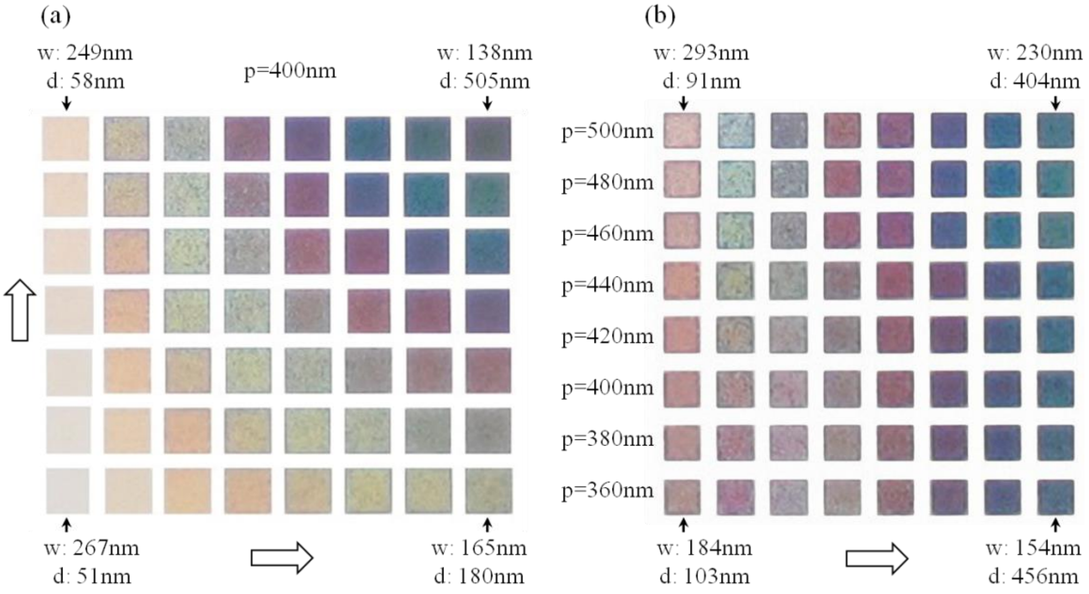

Figure 5. Color palettes generated from square-shaped disk arrays with varying disk etching depth *d*, disk width *w* and unit cell period *P*. (a) Color palette with constant *P* = 400 nm but varying *w* from 267 nm to 138 nm and *d* from 51 nm to 505 nm. Each fabricated disk array has an area of 15 × 15 μm^2. (b) Color palette with a certain *P* in each row changing from 360 nm to 500 nm and varying *w* from 293 nm to 154 nm and *d* from 91 nm to 456 nm. Each fabricated disk array has an area of 10 × 10 μm^2. The dimensions are measured from the SEM images. A variety of colors are obtained based on the designed square arrays, making it is possible to vividly realize the imaging properties with various colors.

range of colors achieved with the designed aluminum metasurfaces can be used forstructural color printing applications. A micrometer scale plasmonic printed copy [Figure 6(b)] of a landscape painting we drew [Figure 6(a)] is fabricated according to the color palettes in Figure 5(a), where the original image features and colors are successfully reproduced. The SEM images of the fabricated plasmonic painting are shown in Figure 6(c)-6(e).

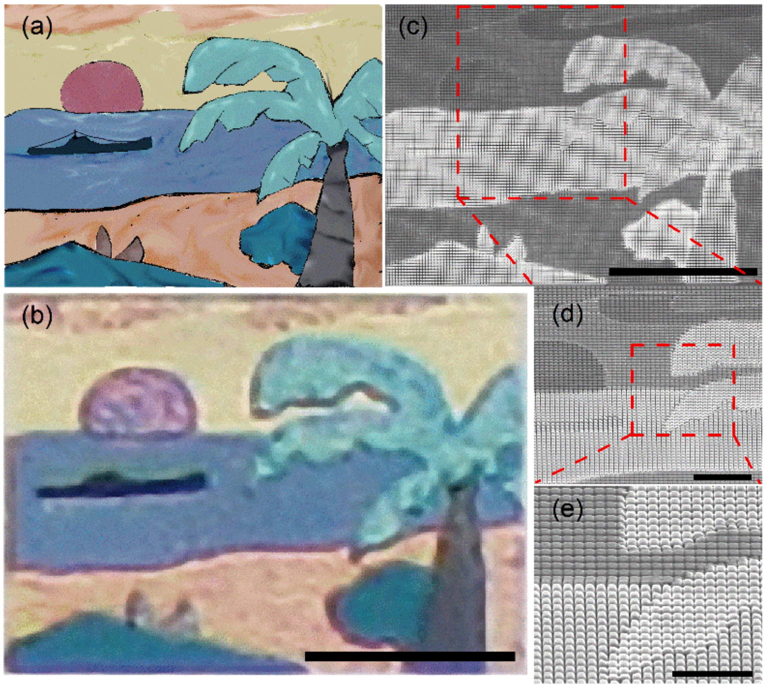

Figure 6. The high-resolution display technology based on the designed structure. (a) Original landscape painting with different colors. (b) The measured bright-field optical microscope image of the plasmonic painting with size of 50 μm by 35 μm. (c) SEM image of the fabricated plasmonic painting with various disk array patterns. (d) SEM image of the area outlined in panel (c). (e) SEM image of the area outlined in panel (d). Both SEM images in panels (d) and (e) are tilted with an angle of 52° to show clear three-dimensional disk array structures. Scale bars: 20 μm in (b) and (c), 5 μm in (d), and 3 μm in (e).

4. INCIDENT ANGLE DEPENDENCE OF OPTICAL RESPONSE

By considering the realistic situation for structural color printing applications, the incident angle dependence and polarization dependence of the optical spectral response are investigated in simulation for one designed square-shaped disk array with $P = 400$ nm, $w = 245$ nm and $d = 114$ nm. The calculated TE (electric field parallel to y axis) and TM (magnetic field parallel to y axis) polarized optical reflection spectra with varying incident angle from 0° to 80° are plotted in Figures 7(a) and 7(b), respectively. For TE polarization, the plasmonic resonance gets a broader linewidth towards the longer wavelength range as the incident angle is increased. While for TM polarization, the bandwidth of strong optical absorption almost linearly extends into the longer wavelength as the incident angle is increased. Such incident angle dependence indicates that the

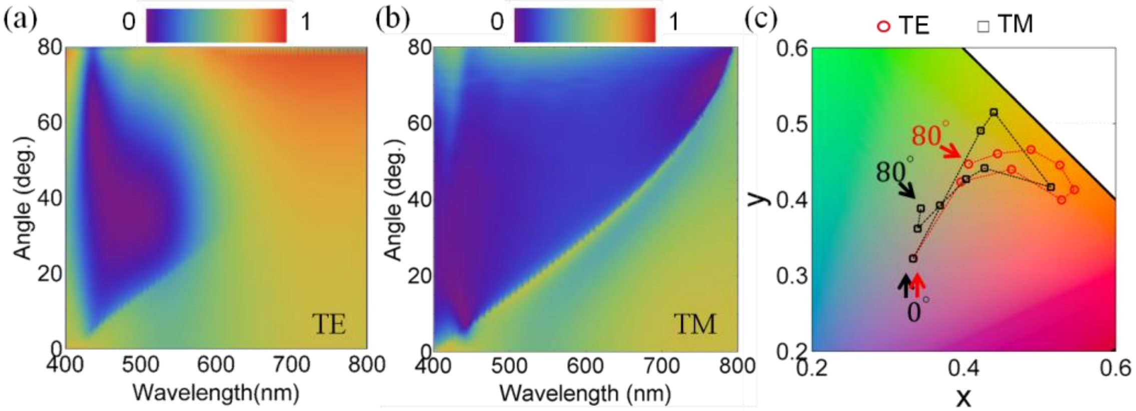

Figure 7. Polarization dependent reflection. Simulated incident angle dependent (a) TE and (b) TM polarized optical reflection spectra for a selected disk array (with $P = 400$ nm, $w = 245$ nm and $d = 114$ nm). (c) Incident angle resolved chromaticity coordinates calculated from the reflection spectra for TE (red circle) and TM (black square) polarizations, indicating the spatial color distribution of the resonators.

excitation of plasmonic modes are relevant to the grating coupling [22, 34, 48]. Based on color theory [81], the TE and TM polarized reflection spectra are converted into the chromaticity coordinates as a function of the incident angle as shown in Figure 7(c).

5. CONCLUSION

In summary, we have demonstrated an all-metal structural color printing platform based on aluminum plasmonic metasurfaces with high resolution and high color performance using a simple, one-step focused ion beam milling process on aluminum surface. A wide range of visible colors has been achieved with the plasmonic metasurfaces by varying the geometrical parameters of square-shaped disk arrays including the disk etching depth, the disk width and the unit cell period. The subtractive colors are obtained from the reflection spectra due to the excitation of plasmonic electric and magnetic dipole resonances. The reproduced microscale landscape painting shows the feasibility and flexibility of all-metal plasmonic metasurfaces used for color printing applications. The demonstrated aluminum plasmonic metasurfaces for structural color printing are well-suited for applications such as microscale imaging, information storage, anti-counterfeit tagging and security marking.

ACKNOWLEDGEMENTS

The authors acknowledge support from the Office of Naval Research (ONR) under Grant N00014-16-1-2408, the National Science Foundation (NSF) under Grant

DMR-1552871 and CBET-1402743. The authors also acknowledge the facility support from the Materials Research Center at Missouri S&T. This work was performed, in part, at the Center for Nanoscale Materials, a U.S. Department of Energy, Office of Science, Office of Basic Energy Sciences User Facility under Contract No. DE-AC02-06CH11357.

REFERENCES

[1] K. Nassau, "The Physics and Chemistry of Color: The 15 Mechanisms," in *The Science of Color: Second Edition* 2003 , pp. 247–280.

[2] L. Huang, X. Chen, H. Mühlenbernd, H. Zhang, S. Chen, B. Bai, Q. Tan, G. Jin, K. W. Cheah, C. W. Qiu, J. Li, T. Zentgraf, and S. Zhang, "Three-Dimensional Optical Holography Using a Plasmonic Metasurface," Nat. Commun. 4, pp. 2808, 2013.

[3] A. Poddubny, I. Iorsh, P. Belov, and Y. Kivshar, "Hyperbolic Metamaterials," Nat. Photonics 7, pp. 958–967, 2013.

[4] N. Meinzer, W. L. Barnes, and I. R. Hooper, "Plasmonic Meta-Atoms and Metasurfaces," Nat. Photonics 8, pp. 889–898, 2014.

[5] N. Yu and F. Capasso, "Flat Optics with Designer Metasurfaces," Nat. Mater. 13, pp. 139–150, 2014.

[6] J. A. Schuller, E. S. Barnard, W. Cai, Y. C. Jun, J. S. White, and M. L. Brongersma, "Plasmonics for Extreme Light Concentration and Manipulation," Nat. Mater. 9, pp. 193–204, 2010.

[7] H. J. Park, T. Xu, J. Y. Lee, A. Ledbetter, and L. J. Guo, "Photonic Color Filters Integrated with Organic Solar Cells for Energy Harvesting," ACS Nano 5, pp. 7055–7060, 2011.

[8] B. Zeng, Y. Gao, and F. J. Bartoli, "Ultrathin Nanostructured Metals for Highly Transmissive Plasmonic Subtractive Color Filters," Sci. Rep. 3, pp. 2840, 2013.

[9] M. J. Uddin, T. Khaleque, and R. Magnusson, "Guided-Mode Resonant Polarization-Controlled Tunable Color Filters," Opt. Express 22, pp. 12307, 2014.

[10] C. Genet and T. W. Ebbesen, "Light in Tiny Holes," Nature 445, pp. 39–46, 2007.

[11] Q. Chen and D. R. S. Cumming, "High Transmission and Low Color Cross-Talk Plasmonic Color Filters Using Triangular-Lattice Hole Arrays in Aluminum Films," Opt. Express 18, pp. 14056, 2010.

[12] D. Inoue, A. Miura, T. Nomura, H. Fujikawa, K. Sato, N. Ikeda, D. Tsuya, Y. Sugimoto, and Y. Koide, "Polarization Independent Visible Color Filter Comprising an Aluminum Film with Surface-Plasmon Enhanced Transmission through a Subwavelength Array of Holes," Appl. Phys. Lett. 98, 2011.

[13] S. Yokogawa, S. P. Burgos, and H. A. Atwater, "Plasmonic Color Filters for CMOS Image Sensor Applications," Nano Lett. 12, pp. 4349–4354, 2012.

[14] Z. Li, A. W. Clark, and J. M. Cooper, "Dual Color Plasmonic Pixels Create a Polarization Controlled Nano Color Palette," ACS Nano 10, pp. 492–498, 2016.

[15] T. Ellenbogen, K. Seo, and K. B. Crozier, "Chromatic Plasmonic Polarizers for Active Visible Color Filtering and Polarimetry," Nano Lett. 12, pp. 1026–1031, 2012.

[16] G. Si, Y. Zhao, J. Lv, M. Lu, F. Wang, H. Liu, N. Xiang, T. J. Huang, A. J. Danner, J. Teng, and Y. J. Liu, "Reflective Plasmonic Color Filters Based on Lithographically Patterned Silver Nanorod Arrays," Nanoscale 5, pp. 6243–6248, 2013.

[17] J. Do, M. Fedoruk, F. Jäckel, and J. Feldmann, "Two-Color Laser Printing of Individual Gold Nanorods," Nano Lett. 13, pp. 4164–4168, 2013.

[18] J. S. Clausen, E. Højlund-Nielsen, A. B. Christiansen, S. Yazdi, M. Grajower, H. Taha, U. Levy, A. Kristensen, and N. A. Mortensen, "Plasmonic Metasurfaces for Coloration of Plastic Consumer Products," Nano Lett. 14, pp. 4499–4504, 2014.

[19] C. Saeidi and D. van der Weide, "Bandwidth-Tunable Optical Spatial Filters with Nanoparticle Arrays," Opt. Express 22, pp. 12499, 2014.

[20] T. Xu, Y.-K. Wu, X. Luo, and L. J. Guo, "Plasmonic Nanoresonators for High-Resolution Colour Filtering and Spectral Imaging," Nat. Commun. 1, pp. 1–5, 2010.

[21] A. F. Kaplan, T. Xu, and L. Jay Guo, "High Efficiency Resonance-Based Spectrum Filters with Tunable Transmission Bandwidth Fabricated Using Nanoimprint Lithography," Appl. Phys. Lett. 99, 2011.

[22] A. S. Roberts, A. Pors, O. Albrektsen, and S. I. Bozhevolnyi, "Subwavelength Plasmonic Color Printing Protected for Ambient Use," Nano Lett. 14, pp. 783–787, 2014.

[23] F. Cheng, J. Gao, S. T. Luk, and X. Yang, "Structural Color Printing Based on Plasmonic Metasurfaces of Perfect Light Absorption," Sci. Rep. 5, pp. 11045, 2015.

[24] F. Cheng, J. Gao, L. Stan, D. Rosenmann, D. Czaplewski, and X. Yang, "Aluminum Plasmonic Metamaterials for Structural Color Printing," Opt. Express 23, pp. 14552, 2015.

[25] F. Cheng, X. Yang, D. Rosenmann, L. Stan, D. Czaplewski, and J. Gao, "Enhanced Structural Color Generation in Aluminum Metamaterials Coated with a Thin Polymer Layer," Opt. Express 23, pp. 25329, 2015.

[26] K. Kumar, H. Duan, R. S. Hegde, S. C. W. Koh, J. N. Wei, and J. K. W. Yang, "Printing Colour at the Optical Diffraction Limit," Nat. Nanotechnol. 7, pp. 557–561, 2012.

[27] X. M. Goh, Y. Zheng, S. J. Tan, L. Zhang, K. Kumar, C. W. Qiu, and J. K. W. Yang, "Three-Dimensional Plasmonic Stereoscopic Prints in Full Colour," Nat. Commun. 5, pp. 5361, 2015.

[28] S. J. Tan, L. Zhang, D. Zhu, X. M. Goh, Y. M. Wang, K. Kumar, C. W. Qiu, and J. K. W. Yang, "Plasmonic Color Palettes for Photorealistic Printing with Aluminum Nanostructures," Nano Lett. 14, pp. 4023–4029, 2014.

[29] C. L. Haynes, A. D. McFarland, L. Zhao, R. P. Van Duyne, G. C. Schatz, L. Gunnarsson, J. Prikulis, B. Kasemo, and M. Käll, "Nanoparticle Optics: The Importance of Radiative Dipole Coupling in Two-Dimensional Nanoparticle Arrays †," J. Phys. Chem. B 107, pp. 7337–7342, 2003.

[30] S. Zou and G. C. Schatz, "Theoretical Studies of Plasmon Resonances in One-Dimensional Nanoparticle Chains: Narrow Lineshapes with Tunable Widths," Nanotechnology 17, pp. 2813–2820, 2006.

[31] V. A. Markel and A. K. Sarychev, "Surface Plasmons in Ordered and Disordered Chains of Metal Nanospheres," Conf. Quantum Electron. Laser Sci. - Tech. Dig. Ser. 75, pp. 85426, 2007.

[32] Y. K. R. Wu, A. E. Hollowell, C. Zhang, and L. Jay Guo, "Angle-Insensitive Structural Colours Based on Metallic Nanocavities and Coloured Pixels beyond the Diffraction Limit," Sci. Rep. 3, pp. 1194, 2013.

[33] T. W. Ebbesen, H. J. Lezec, H. F. Ghaemi, T. Thio, and P. A. Wolff, "Extraordinary Optical Transmission through Sub-Wavelenght Hole Arrays," Nature 391, pp. 667–669, 1998.

[34] L. Martín-Moreno, F. J. García-Vidal, H. J. Lezec, K. M. Pellerin, T. Thio, J. B. Pendry, and T. W. Ebbesen, "Theory of Extraordinary Optical Transmission through Subwavelength Hole Arrays," Phys. Rev. Lett. 86, pp. 1114–1117, 2001.

[35] H. Liu and P. Lalanne, "Microscopic Theory of the Extraordinary Optical Transmission," Nature 452, pp. 728–731, 2008.

[36] R. J. H. Ng, X. M. Goh, and J. K. W. Yang, "All-Metal Nanostructured Substrates as Subtractive Color Reflectors with near-Perfect Absorptance," Opt. Express 23, pp. 32597, 2015.

[37] J. Zhang, J.-Y. Ou, N. Papasimakis, Y. Chen, K. F. MacDonald, and N. I. Zheludev, "Continuous Metal Plasmonic Frequency Selective Surfaces," Opt. Express 19, pp. 23279, 2011.

[38] V. R. Shrestha, S. S. Lee, E. S. Kim, and D. Y. Choi, "Aluminum Plasmonics Based Highly Transmissive Polarization-Independent Subtractive Color Filters Exploiting a Nanopatch Array," Nano Lett. 14, pp. 6672–6678, 2014.

[39] L. Wang, R. J. H. Ng, S. Safari Dinachali, M. Jalali, Y. Yu, and J. K. W. Yang, "Large Area Plasmonic Color Palettes with Expanded Gamut Using Colloidal Self-Assembly," ACS Photonics 3, pp. 627–633, 2016.

[40] T. Søndergaard, S. M. Novikov, T. Holmgaard, R. L. Eriksen, J. Beermann, Z. Han, K. Pedersen, and S. I. Bozhevolnyi, "Plasmonic Black Gold by Adiabatic Nanofocusing and Absorption of Light in Ultra-Sharp Convex Grooves," Nat. Commun. 3, pp. 969, 2012.

[41] T. Søndergaard and S. I. Bozhevolnyi, "Theoretical Analysis of Plasmonic Black Gold: Periodic Arrays of Ultra-Sharp Grooves," New J. Phys. 15, pp. 013034, 2013.

[42] S. Westland and C. Ripamonti, "Computing CIE Tristimulus Values," in *Computational Colour Science Using MATLAB* John Wiley & Sons, Ltd, 2004 , pp. 27–48.

[43] V. A. Fedotov, P. L. Mladyonov, S. L. Prosvirnin, and N. I. Zheludev, "Planar Electromagnetic Metamaterial with a Fish Scale Structure," Phys. Rev. E - Stat. Nonlinear, Soft Matter Phys. 72, 2005.

[44] W. Cai, U. K. Chettiar, H.-K. Yuan, V. C. de Silva, A. V. Kildishev, V. P. Drachev, and V. M. Shalaev, "Metamagnetics with Rainbow Colors," Opt. Express 15, pp. 3333, 2007.

[45] Z. Fang, Y. R. Zhen, L. Fan, X. Zhu, and P. Nordlander, "Tunable Wide-Angle Plasmonic Perfect Absorber at Visible Frequencies," Phys. Rev. B - Condens. Matter Mater. Phys. 85, pp. 1–7, 2012.

[46] T. Xu, H. Shi, Y. K. Wu, A. F. Kaplan, J. G. Ok, and L. J. Guo, "Structural Colors: From Plasmonic to Carbon Nanostructures," Small 7, pp. 3128–3136, 2011.

II. WAVELENGTH-SELECTIVE MID-INFRARED METAMATERIAL ABSORBERS WITH MULTIPLE TUNGSTEN CROSS RESONATORS

Zhigang Li,[1] Liliana Stan,[2] David A. Czaplewski,[2] Xiaodong Yang,[1] and Jie Gao [1,*]

[1]Department of Mechanical and Aerospace Engineering, Missouri University of Science and Technology, Rolla, MO 65409, USA

[2]Center for Nanoscale Materials, Argonne National Laboratory, Argonne, IL 60439, USA

ABSTRACT

Wavelength-selective metamaterial absorbers in the mid-infrared range are demonstrated by using multiple tungsten cross resonators. By adjusting the geometrical parameters of cross resonators in single-sized unit cells, near-perfect absorption with single absorption peak tunable from 3.5 μm to 5.5 μm is realized. The combination of two, three, or four cross resonators of different sizes in one unit cell enables broadband near-perfect absorption at mid-infrared range. The obtained absorption spectra exhibit omnidirectionality and weak dependence on incident polarization. The underlying mechanism of near-perfect absorption with cross resonators is further explained by the optical mode analysis, dispersion relation and equivalent RLC circuit model. Moreover, thermal analysis is performed to study the heat generation and temperature increase in the cross resonator absorbers, while the energy conversion efficiency is calculated for the thermophotovoltaic system made of the cross resonator thermal emitters and low-bandgap semiconductors. The designed metamaterial absorbers (emitters) are expected to be promising in energy harvesting applications.

1. INTRODUCTION

Metamaterials exhibit intriguing electromagnetic properties with flexibly tailored permittivity and permeability through engineering the geometrical shape and material composition of artificial meta-atoms [1]. One important application of metamaterials is perfect light absorbers and thermal emitters used for promising applications of energy harvesting, imaging, sensor, and optical communication [2–4]. Metamaterial perfect absorbers in the mid-infrared range are appealing to various applications such as thermal imaging system with spatial light manipulation [5], molecular or gas sensing with low cost [6,7], and thermophotovoltaics (TPV) with conversion efficiency exceeding the Shockley-Queisser (SQ) limit [8–11]. Thermal emitters play key roles in TPV systems with heat energy directly converted into electric power. Since the emissivity of a material equals to the absorptivity at equilibrium according to the Kirchhoff's law [12], the thermal emission spectrum of a metamaterial at a certain temperature can be equivalently predicted by its light absorption spectrum. For TPV system with relatively high-bandgap semiconductor such as GaSb (0.71 eV), it requires a narrowband metamaterial thermal emitter with resonant wavelength shorter than 1.75 µm and radiation suppression at other wavelengths for getting optimal conversion efficiency [13]. By considering the thermal stability, high temperature-enduring refractive metals (e.g. Ti [14], W [8], Pt [15,16]) and dielectrics (e.g. Al_2O_3 [7], TiN [17]) are preferred materials for constructing the metamaterial thermal emitters.

In terms of the materials used, metamaterial absorbers can be mainly categorized into three types: all-metallic, metal-dielectric and all-dielectric metamaterial absorbers [18,19]. All-metallic micro-/nano-cavities or photonic crystal structures in 1D [20], 2D [21] and 3D [22] have been widely investigated for efficient light absorption, owing to the advantages of intrinsic thermal stability and enhanced photonic density of states. In contrast, all-dielectric structures are able to realize a narrow absorption window via surface phonon polaritons or inter-subband transitions [23,24]. Metal-dielectric metamaterials are known as perfect absorbers or emitters with the excitation of plasmonic magnetic resonance at certain wavelength [2,25–28]. The metal-insulator-metal (MIM) structures are usually designed as a combination of a metallic ground plane, a dielectric spacer and a top patterned metallic layer with resonators. Various geometries have been designed to obtain wavelength-selective metamaterial absorbers with omnidirectional and polarization-independent properties, including simple multilayer [29], ring resonator [2], fishnet [30], patch resonator [25], cross resonator [26] and other complex structures [1]. Since the resonance wavelength of a single resonator highly depends on its geometrical design, methods have been developed by combining dual or multiple resonators with different sizes in one unit cell in order to obtain the multi-band or broadband absorption, including multi-width strips [27], multiple patches [28], cross resonators [26], disks [31] and mixture of cross and disk resonators [32], as well as stacked double ring resonators [33]. The metal-dielectric multilayers are also used to realize ultra-broadband absorption with either 1D gratings [34] or 2D trapezoid cavities [35] based on the stop-light waveguide theory and structured metamaterial absorber through multiple overlapping resonances [36,37].

In this work, wavelength-selective metamaterial absorbers in the mid-infrared range are demonstrated by using single-sized and double-sized unit cells of tungsten cross resonators to obtain single peak, dual-band and broadband near-perfect absorption (or emission) at mid-infrared range. The design and optimization of metamaterial absorbers are discussed, followed by the experimental characterization of the absorption spectra. The underlying mechanism of near-perfect absorption in cross resonators is explained with the excitation of optical magnetic resonances for both TM and TE polarized incidence, and is further modelled by equivalent RLC circuit for intuitive understanding. Finally, potential applications at mid-infrared range for metamaterial absorbers and emitters are analyzed through the thermal analysis for heat generation and temperature increase, as well as the energy conversion efficiency calculation for low-temperature TPV system based on low-bandgap semiconductors.

2. DESIGN AND CHARACTERIZATION OF MID-INFRARED ABSORBERS

The designed metamaterial absorbers are composed of a top 50 nm-thick tungsten (W) layer patterned with cross resonators, a 200 nm-thick alumina (Al_2O_3) spacer layer and a 200 nm-thick tungsten ground plane on a silicon substrate, denoted as t_h, t_d and t_m, respectively. The thicknesses of top tungsten layer and spacer layer are selected to optimize the absorption performance and fabrication quality for the following absorber designs. The thick tungsten ground plane will effectively block the transmission so that the absorption is equal to unity minus the reflection. Figure 1(a) presents the schematics of single-sized unit cells of cross resonators A, B, C and D with the same geometrical parameters of period (P = 1500 nm) and arm width (w = 450 nm) but different arm lengths L of 0.87P, 0.77P, 0.67P and 0.57P, respectively. As shown in Figures 1(b)–1(d), by combining two, three or four cross resonators of different sizes in one double-sized unit cell, metamaterial absorber patterns of ADAD, ABCC, and ABCD are obtained for realizing flexibly tunable absorption band.

Geometrical parameters of metamaterial absorbers are optimized with numerical simulation (COMSOL Multiphysics), by starting from a single-sized unit cell of cross resonator with P = 900 nm, L = 800 nm and w = 300 nm at normal incidence under averaged TE and TM polarizations. Figures 2(a)–2(c) give the simulated polarization-averaged absorption spectra of single-sized unit cells as functions of period, arm length and arm width, where two main absorption peaks are observed. The absorption peak at around 1.5 μm is due to the grating effect of coupled cross resonators, showing less

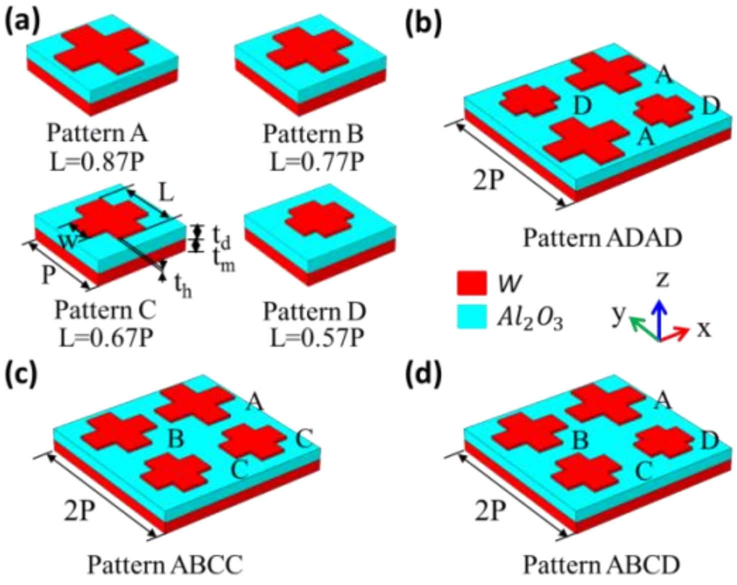

Figure 1. Schematics of the unit cells of wavelength-selective metamaterial absorbers with tungsten cross resonators. (a) Single-sized unit cells of cross resonators A, B, C and D with the same period P and arm width w but different arm length L. (b - d) The combination of two, three or four cross resonators of different sizes in one double-sized unit cell, forming the patterns of ADAD, ABCC, and ABCD, respectively.

dependence on the geometrical parameters of cross resonators. Another absorption peak at longer wavelength arises from the magnetic resonance of cross resonator, exhibiting a strong dependence on the period and arm length but not arm width. Moreover, Figures. 2(d)–2(f) show the absorption spectra of length but not arm width. Moreover, Figures. 2(d)–2(f) show the absorption spectra of three different types of double-sized unit cells with patterns of ADAD, ABCC and ABCD by changing the unit cell period, where dual-band and broadband near-perfect absorption at mid-infrared range are achieved. In experiment, the unit cell period of P = 1500 nm is used by considering a balance between high absorption and relatively wide bandwidth for double-sized unit cells.

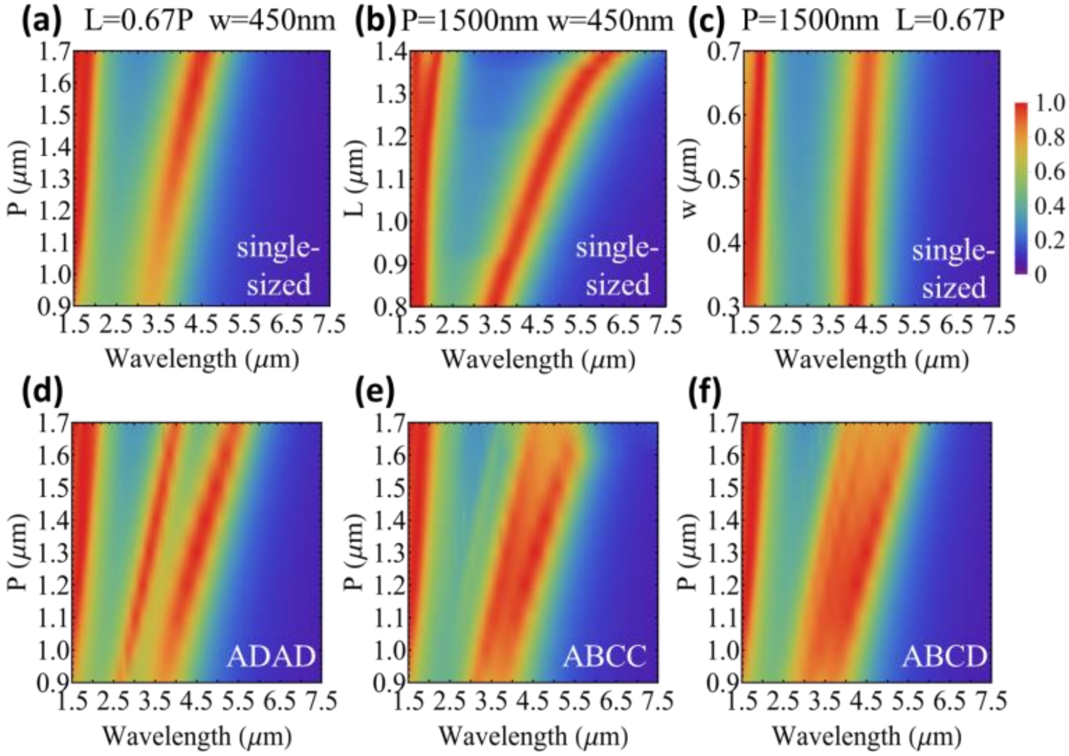

Figure 2. Simulated polarization-averaged absorption spectra of metamaterial absorbers as functions of geometrical parameters at normal incidence, for single-sized unit cells with varying (a) period P, (b) arm length L and (c) arm width w, and for double-sized unit cells of (d) ADAD, (e) ABCC and (f) ABCD with varying period P.

The W-Al_2O_3-W three-layer stack is grown by RF sputtering on a silicon substrate. The W is grown in Ar atmosphere at 6 mTorr pressure at a deposition rate of 0.75 Å / sec and the Al_2O_3 is grown in Ar atmosphere at 5 mTorr pressure at a rate of 0.08 Å / sec. The designed cross resonator patterns are fabricated with focused ion beam (FIB) milling on the top tungsten layer. Figures 3(a)–3(d) show scanning electron microscopy (SEM) images of the fabricated metamaterial absorbers with cross resonator array patterns of C, ADAD, ABCC and ABCD, with the geometrical parameters of cross resonators A, B, C and D described in Figure 1(a). Due to the strong atomic bonding force and high hardness of W, the FIB milled W cross resonators have relatively rough side walls, compared with other metals such as Au [38], Ag [39] and Al [40,41]. Such imperfections in the fabrication process gives an averaged variation of ± 15 nm in the geometrical parameters of cross resonators different from the design. The absorption spectra of the metamaterial absorbers are obtained from the measured reflection spectra at normal incidence using Fourier transform infrared spectroscopy (FTIR). The measured reflection spectra are normalized with the reflection from a high-quality gold mirror. Numerical simulation is further conducted with the geometrical parameters of cross resonators obtained from the SEM images, where the permittivity of W and Al2O3 is from Rakic [42] and Kischkat [43], respectively.

Figure 4 shows the experimental unpolarized absorption spectra (solid lines) at normal incidence for different unit cell patterns, where the simulated polarization-averaged absorption spectra (dashed lines) are also plotted for comparison. In Figure 4(a), it shows the absorption spectra of single-sized unit cell patterns of A, B, C and D with P = 1500 nm and w = 450 nm but L = 0.87P, 0.77P, 0.67P and 0.57P, respectively. A near perfect absorption peak induced by the magnetic resonance of the cross resonator shows red shift with the increased arm length, allowing the widely tunable absorption band ranging from 3.5 µm to 5.5 µm, which differs from the almost fixed absorption peak at 1.73 µm due to the grating effect of coupled cross resonators. The deviation between the experimental and simulation results can be explained by the imperfect geometries in the fabricated cross resonators and the variation of permittivity. The influence of period is shown in Figure 4(b) for the double-sized unit cell pattern ADAD. Two individual absorption peaks at longer wavelength arising from resonator A and D in the double-sized unit cell pattern ADAD exhibit red shift with the increased period and the fixed arm width, however, a mitigation of the absorption appears due to the reduced effective light-

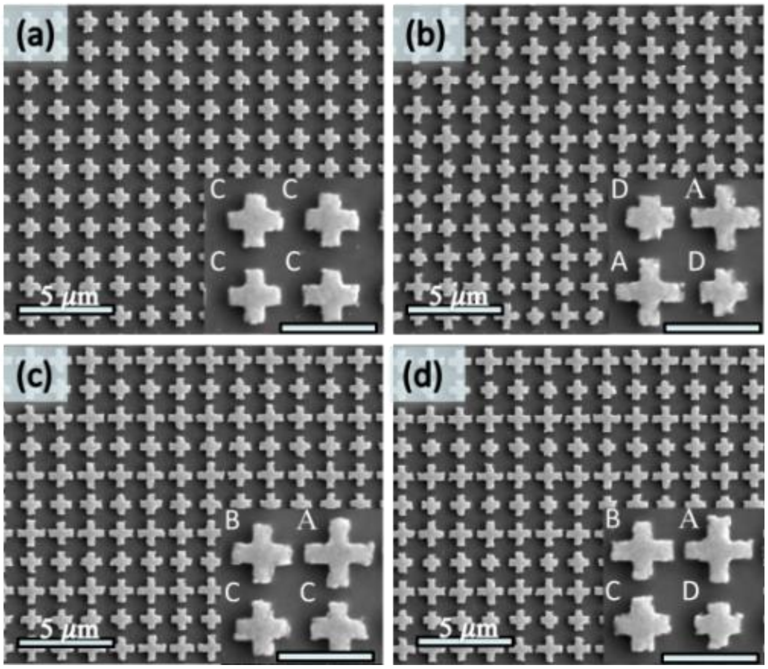

Figure 3. SEM images of the fabricated metamaterial absorbers. The cross resonator arrays for unit cell patterns of (a) C, (b) ADAD, (c) ABCC and (d) ABCD. The scale bar inside the insert image is 1 µm.

cross resonator interaction volume. Additionally, the improved absorption has been observed by increasing the arm width w from 450 nm to 600 nm. The structure with larger arm width has higher fabrication tolerance, and the effect of roughness on absorption is less compared to the structure with smaller arm width.

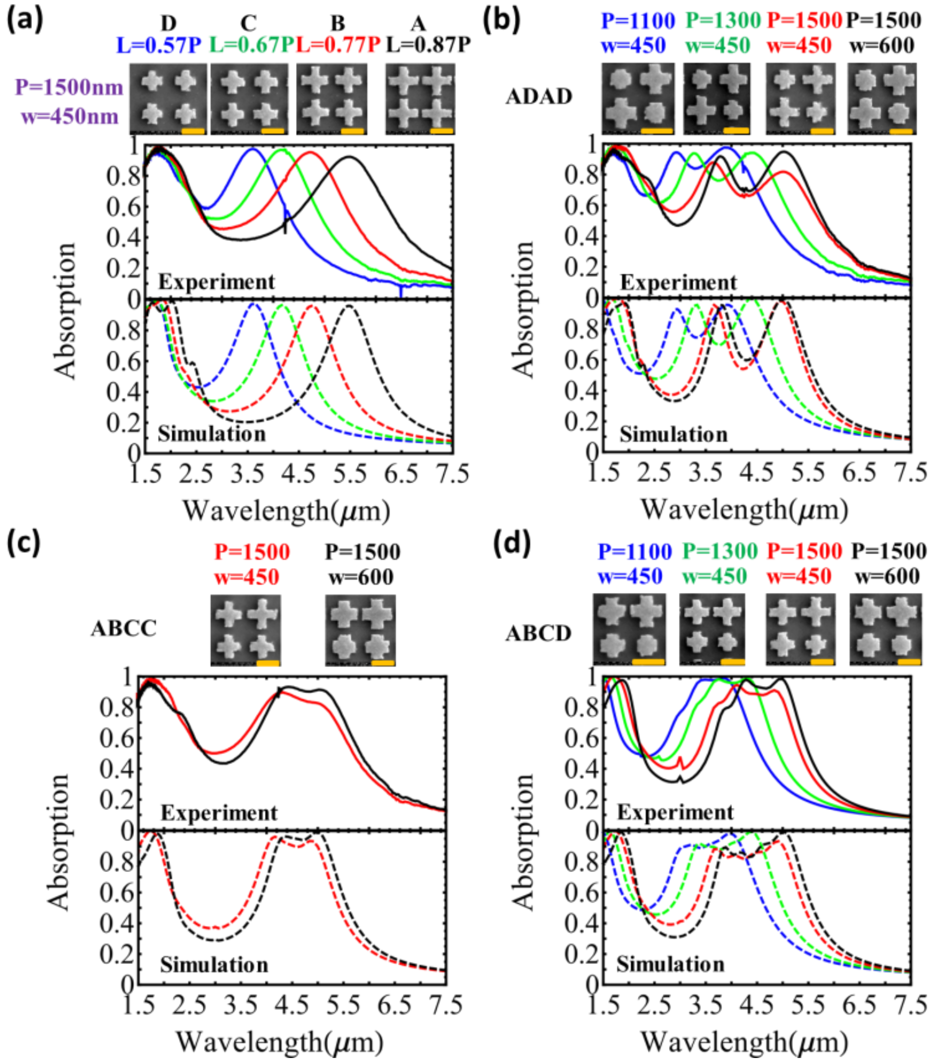

Figure 4. Experimental (unpolarized) and simulated (polarization-averaged) absorption spectra at normal incidence for cross resonator arrays with different unit cell patterns. (a) A, B, C and D with P = 1500 nm and w = 450 nm but L = 0.87P, 0.77P, 0.67P and 0.57P, respectively. (b) ADAD with P = 1100 nm, 1300 nm and 1500 nm. (c) ABCC with different w but same P and L. (d) ABCD with different P The scale bar of the SEM image is 1 µm.

More continuous absorption bands are realized with the double-sized unit cell patterns of ABCC and ABCD, as shown in Figures 4(c) and 4(d), respectively. With P = 1500 nm and w = 600 nm, pattern ABCC shows an absorption band of around 900 nm with the absorption intensity over 0.9 (the maximum of 0.93). And the absorption band is about 1 μm (1.2 μm) for the absorption intensity over 0.88 (0.85) for pattern ABCD. Compared with the absorption spectra of pattern ABCC, the single-sized unit cell D slightly broadens the absorption band to the shorter wavelength range in pattern ABCD, but it also affects the absorption intensity due to the weak coupling with neighboring resonators. Furthermore, a near perfect absorption band is observed in experiment for pattern ABCD with P = 1100 nm and w = 450 nm, having the absorption intensity over 0.94 (the maximum of 0.96) from 3.22 μm to 4 μm.

3. OPTICAL MODE ANALYSIS AND EQUIVALENT CIRCUIT MODEL

In Figure 5, cross sections of magnetic field Hy distributions along the x-z plane across the unit cells are plotted under TM polarization (electric field is along x direction) at normal incidence, where the location of each cross section view is illustrated in Figures 5(e1)-5(e4). Figures 5(a1)-5(a3) show the magnetic field distributions in unit cell pattern C at the wavelength of 4.17 μm and 1.73 μm, representing the first-order and high-order magnetic resonance modes along the horizontal cross arm along the x direction, respectively. The black arrows represent the direction and magnitude of the induced electric current density. The magnetic resonance arises from the antiparallel currents of electric charges in the W layers excited by the incident light [2]. There is one induced current loop between the top W resonator and the ground plane for the first-order magnetic resonance at 4.17 µm in Figure 5(a1). For the high-order magnetic resonance at 1.73 µm in Figure 5(a2), there are multiple induced current loops observed with the coupling between neighboring cross resonators. This type of resonance at short wavelength is related to the grating effect of coupled cross resonators, and the cross-talk effect between the neighboring cross resonators manifests itself by the connected induced

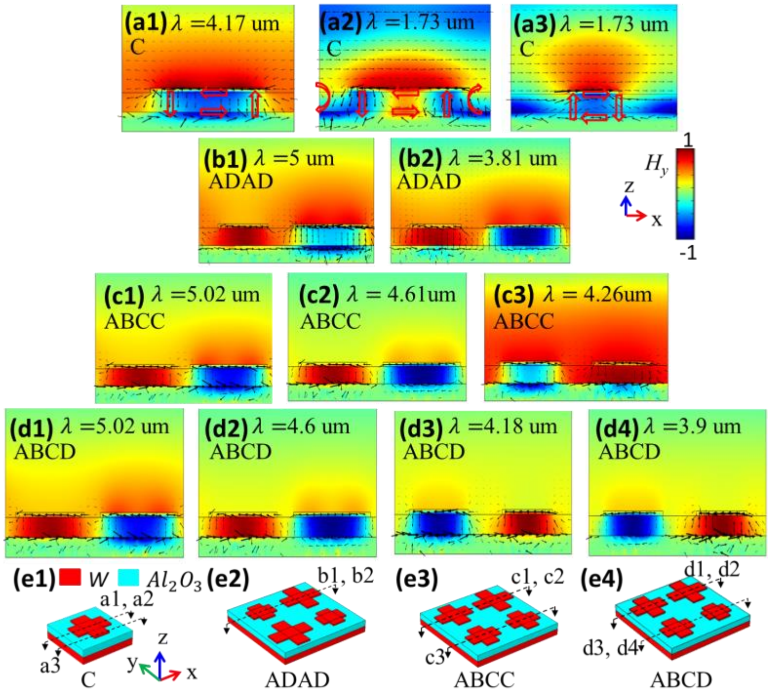

Figure 5. Cross section view of the normalized magnetic field Hy distribution at different resonance wavelengths under TM polarization at normal incidence. Results for the designed unit cell patterns of (a1 - a3) C, (b1 - b2) ADAD, (c1 - c3) ABCC and (c1 - c4) ABCD. The black arrows represent the induced current density. (e1 - e4) Schematics of the locations of cross sections in the designed unit cells.

current loops. Furthermore, as shown in Figures 5(b)-5(d), the first-order magnetic resonance and induced current loop are also found in the magnetic field distributions at longer wavelengths for double-sized unit cell patterns. The combination of the multiple first-order magnetic resonances in cross resonators with different sizes are responsible for the generation of absorption bands with different bandwidth and absorption intensity [25–27].

In order to develop further understanding of absorption performance, the dispersion relations of designed metamaterial absorbers are plotted through the simulated absorption spectra as a function of wave number λ^{-1} and in-plane wave vector kx normalized with half of the reciprocal lattice vector kd = π/P. The results are shown in Figure 6 for unit cell patterns of A, D, and ABCD under TM and TE polarization, respectively. It shows that there is almost no dependence of the absorption peak and band on the incident angle for the first-order magnetic resonances at long wavelengths larger than 2.5 μm (below 4000 cm-1), which is a significant advantage for absorber or emitter applications with omnidirectional requirements. However, for the high-order magnetic resonance at high wave number larger than 4000 cm-1, the absorption branch is strongly modified by the grating effect of coupled cross resonators, with the excitation of spoof surface plasmons [16,25,44,45]. The dispersion relation of surface plasmons is described as |kspp| = (ω/c)$\sqrt{\varepsilon_1\varepsilon_2/(\varepsilon_1+\varepsilon_2)}$, where ε_1 and ε_2 denotes the permittivity of metal and dielectric, respectively. It is noted that spoof surface plasmons are usually considered for 1D or 2D periodic metamaterials under TM polarization [44,46], however, spoof surface plasmons also exist under TE polarization for 2D case [45]. For a 2D periodic metamaterial absorber, to excite spoof surface plasmons, momentum matching condition (i.e. kspp = k||, inc + kg) must be achieved at a specific wavelength. k||, inc = kx,inc $\hat{\boldsymbol{x}} +$ ky,inc $\hat{\boldsymbol{y}}$, representing the wave vector of the tangential component of the incident light in the x-y plane. kg is the reciprocal lattice vector of the Bloch wave for the grating with kg $=2\pi m/P\,\hat{\boldsymbol{x}} + 2\pi n/P\,\hat{\boldsymbol{y}}$, where m and n are the grating diffraction order along the x and y direction, respectively. The wave vector of spoof surface plasmons is then a function of unit cell period and incident angle, which is observed in Figure 6. The excitation of different diffraction orders of spoof surface plasmons depends on the incident polarization. For TM polarized incidence with only kx,inc, |kspp| = |kx,inc + $2\pi m/P$| with kx,inc = (ω/c)sinθ and the assumption of n = 0. The branches with diffraction orders of m = ± 1 are plotted with white dashed lines in Figures 6(a1)–(c1)

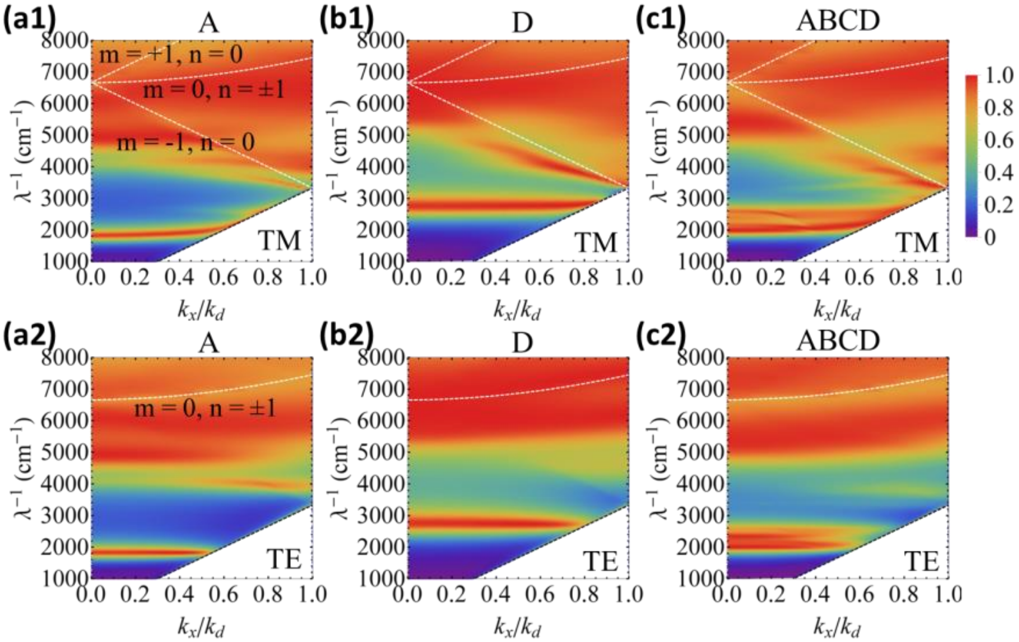

Figure 6. Polarized dispersion. Dispersion relation of unit cell patterns of A, D, and ABCD under (a1 - c1) TM and (a2 - c2) TE polarization, respectively. The white dashed lines are obtained from the grating dispersion relations at different diffraction orders.

from the theoretical dispersion relation. In addition, the diffraction orders with m = 0 and n = ± 1 are shown under TM polarization following the relation of |kspp| =

$\sqrt{(\omega\sin\theta/c)^2+(2\pi n/P)^2}$, which are attributed to the electric field component along the y direction of the diffracted wave. Furthermore, in Figures 6(a2)–6(c2), the diffraction orders with m = 0 and n = ± 1 are plotted under TE polarization where the above dispersion relation is still followed, where the incident electric field is dominant along y direction with kx,inc = 0. The dispersion curve shows blue shift with the increased incidence angle for the TE case. The above dispersion analysis explains the strong interactions between the high-order magnetic resonances of neighboring cross resonators and the excitation of spoof surface plasmons at short wavelength range [45,47].

In order to obtain an intuitive description of the underlying mechanism for magnetic resonance characteristics, the designed cross resonators are analyzed with the equivalent RLC circuit model [48,49] to model not only the first-order magnetic resonance and its coupling but also the impedance of the effective multilayer stack. Figure 7(a) shows the equivalent RLC circuit model of the single-sized unit cell pattern C. The total impedance ZC is composed of the impedance from unit cell pattern ZC0 and the impedance of the effective multilayer stack Zms. For ZC0, two types of capacitance are considered, the parallel capacitance between the top W resonator and ground plane Cd = $\phi_1\varepsilon_0\varepsilon_d$(2Lw-w2)/td and an approximated gap capacitance between neighboring resonators Cg = $\phi_2\varepsilon_0\varepsilon_d$wth/(P-L), where ε_0 is the permittivity in the free space, ϕ_1 and ϕ_2 are numerical factors to approximate the non-uniform distribution of charges due to the induced electric currents [48,49]. Furthermore, Lm is employed to represent the mutual magnetic inductance from stored magnetic energy between the top W resonator and the ground plane, while Lk accounts for the kinetic inductance induced from the kinetic movement of free charge carriers inside the W layers. Lm = $\phi_3\mu_0$Ltd/w with the permeability of free space, μ_0, and the numerical factor, ϕ_3, to rectify the geometrical approximation. Lk can be derived from the complex kinetic impedance Zk = Rk - $i\omega$Lk with Zk = L/(Aeff $\tilde{\sigma}$) and Aeff = ϕ_4wλ/(2$\pi\kappa$). Aeff denotes the effective area across. The induced current path obtained from the multiplication of arm width and skin depth of W, with the extinction coefficient κ [50] and the numerical factor ϕ_4. The complex conductivity of W reads $\tilde{\sigma} = \sigma' + i\sigma''$, where $\sigma' = \omega\varepsilon_0\varepsilon_m''$ and $\sigma'' = -\omega\varepsilon_0\varepsilon_m'$ are derived from Maxwell's equation by considering the conduction current density and displacement current density [50]. Therefore, Rk and Lk can be solved from the real part and imaginary part of Zk, respectively. Additionally, the impedance of the effective

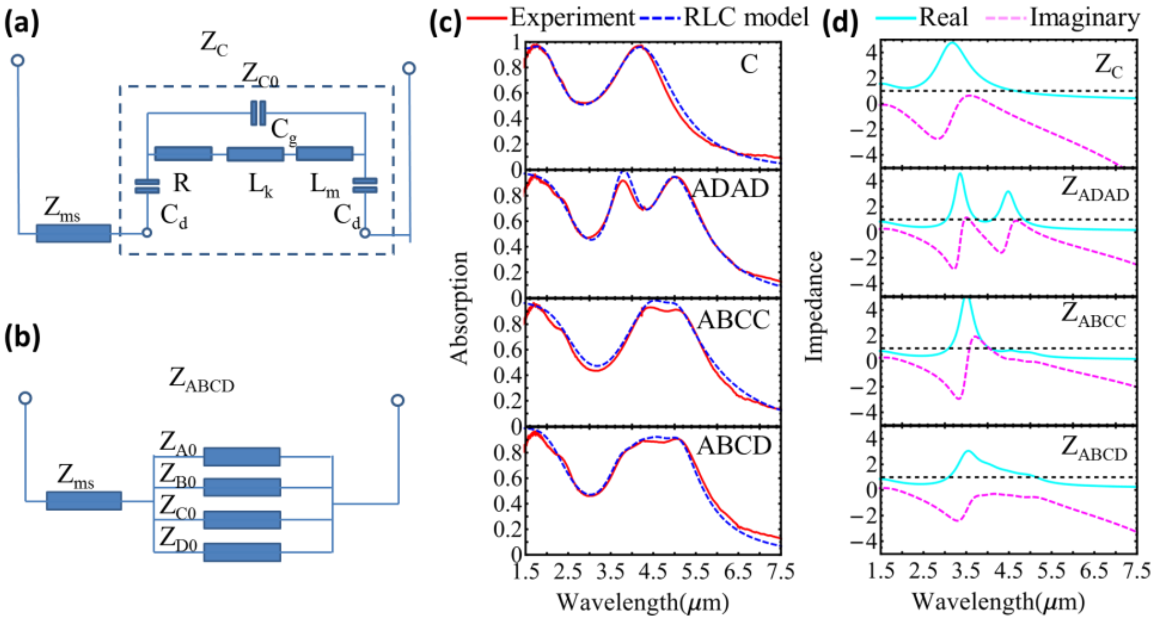

Figure 7. Equivalent RLC circuit model of the designed unit cells of cross resonators. (a) Single-sized unit cell of C. (b) Double-sized unit cell pattern of ABCD. (c) Unpolarized absorption spectra obtained from experiment and equivalent RLC model at normal incidence for unit cell patterns of C, ADAD, ABCD and ABCD. (d) The real and imaginary parts of normalized impedance calculated from equivalent RLC model. The dashed line is at the impedance of 1.

multilayer stack Zms can be calculated from the impedance transformation method [51]. This method is based on the recursion relation of Zj = η_j(Zj+1 + i$\eta_j$tankjdj) / (η_j + iZj+1tankjdj), j = 2, 1, with the initialization of Z3 = η_3, where η_j= $\sqrt{\mu_0/(\varepsilon_0\varepsilon_j)}$ expresses the intrinsic impedance of the jth layer with thickness dj and refractive index nj. The impedance of vacuum is Z_0 =$\sqrt{\mu_0/\varepsilon_0}$. kj is the wave vector at the jth layer with kj = njk0, where k0 denotes the wave vector in free space. The impedance of the effective multilayer stack is then obtained by the relation Zms = ϕ_5Z1, where ϕ_5 is numerical factor to account for the influence from the cross resonator pattern in the effective multilayer stack assumption. Finally, the total impedance of single-sized unit cell pattern C is obtained by Zc = Zms + (Zk + $i\omega$Lm) / [1 + $i\omega$Cg(Zk + $i\omega$Lm)]+2 / ($i\omega$Cd). As shown in Figure 7(b), regarding the impedance of multiple cross resonators, a parallel circuit connecting each single-sized unit cell is employed to evaluate the coupling effect of multiple resonances for the double-sized unit cell patterns of ABCD, with the impedance of each cross resonator denoted as ZA0, ZB0, ZC0 and ZD0, respectively. To simplify the problem, a homogenization assumption is used by setting the same value for each type of numerical factor (ϕ_1, ϕ_2, ϕ_3, ϕ_4), and the same value for gap capacitance between neighboring resonators with Cg = $\phi_2\varepsilon_0\varepsilon_d$wth/deff, where the effective distance deff = [(2P – LA – LB)+ (2P – LB – LC)+ (2P – LC – LD)+ (2P – LA – LD)]/4. The total impedance of the whole unit cell pattern of ABCD reads ZABCD = Zms + (1/ZA0+1/ZB0+1/ZC0+1/ZD0). The absorption spectrum is consequently calculated by A = 1 – [(ZABCD – Z0) / (ZABCD + Z0)]2. Figure 7(c) plots the equivalent RLC model calculated unpolarized absorption spectra for metamaterial absorbers with unit cell patterns of C, ADAD, ABCC and ABCD, respectively, showing a good agreement with the measured results. Accordingly, Figure 7(d) shows the real and imaginary parts of the total effective impedance Ztotal of the designed metamaterial absorbers, normalized by the Z0 of free space. The absorption performance can be alternatively explained through the impedance match theory [4]. When Ztotal/Z0 approaches 1, there is no reflected wave and a strong absorption band will appear in the absorption spectrum.

4. THERMAL ANALYSIS FOR ABSORBERS AND ENERGY CONVERSION EFFICIENCY FOR EMITTERS

As the incident light wave is coupled into the metamaterial absorber, heat is generated due to the optical loss of the W layers and the time-averaged dissipative energy density per unit volume is written as $Q_{\mathrm{h}} = \varepsilon_0 \omega \varepsilon_m''(\omega)|\boldsymbol{E}|^2/2$, where $\boldsymbol{E}$ is the electric field and ε_m'' is the imaginary part of the metal [52,53]. Figure 8 shows the distributions of the time-averaged dissipative energy density at the cross section of the top W layer for the designed metamaterial absorbers at different resonance wavelengths, with green arrows describing the direction and magnitude of the Poynting vector. The power dissipation density distributions in Figure 8 are obtained with TM polarized normally incident light with the power of 22.2 μW/μm^2 for each type of metamaterial absorber. From the top view of the unit cell pattern of C at two resonance wavelengths in Figures 8(a1) and 8(a3), the optical energy flow inside the W cross resonators at certain resonant wavelengths generate heat. The cross sections in Figures 8(a2) and 8(a4) show the optical energy penetration inside the absorbers and both the W resonator and ground plane contribute to the heat generation through dissipative loss. Similar dissipation process happens for metamaterial absorbers with double-sized unit cell patterns of ADAD, ABCC and ABCD, as seen in Figures 8(b1)-8(b2), 8(c1)-8(c3) and 8(d1)-8(d4), where the specific energy dissipation distribution inside each type of unit cell at certain resonance wavelength is observed.

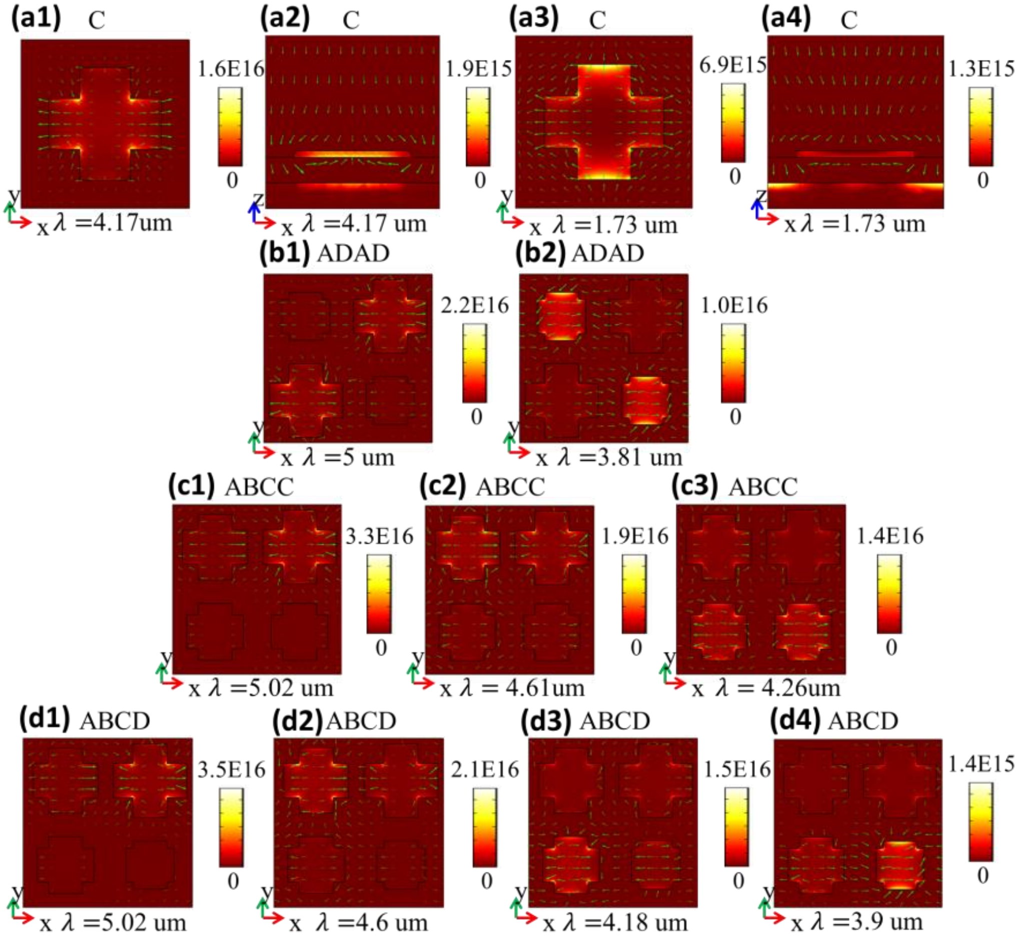

Figure 8. Time-averaged optical power dissipation density Q_h (W/m^3) distributions at the cross section (x-y plane) of top W layer. Results for unit cell patterns of (a1, a3) C, (b1, b2) ADAD, (c1 - c3) ABCC and (d1 - d4) ABCD at different resonance wavelengths under normal incidence. Cross section (x-z plane) of single-sized unit cell pattern of C is shown in (a2) and (a4). Green arrows show direction and magnitude of Poynting vector.

The generated heat Q_d serves as the heat source in the transient heat transfer equation $C_p\rho\partial T/\partial t + \nabla\cdot(-k_c\nabla T) = Q_d$, where C_p, ρ, k_c, are the material dependent specific heat capacity, density and thermal conductivity, respectively. To simplify the heat transfer analysis, the steady-state heat transfer is considered by setting the time derivative component as zero. This equation has been proved valid for a nanoscale material system, however, the parameter of thermal conductivity needs to be modified accordingly for thin films [53–56]. It has been theoretically and experimentally pointed out that the thermal conductivity of a thin film at the nanoscale dramatically decreases since the interfacial scattering effects between similar or dissimilar materials inside the structure significantly impede the vibrational energy transfer across the interfaces [55]. To simplify the problem, specific heat capacity and density can still be the same as bulk material. Thermal parameters used in this work are listed in Table 1 [53–56]. To solve the heat transfer problem, proper boundary conditions are imposed on the designed metamaterial absorber. At the bottom of the 100 µm-thick silicon substrate, a Dirichlet boundary condition is used by setting a constant temperature $T = T_0$, where T_0 is the room temperature of 300 K. Following the boundary conditions used in [53], the heat generation and temperature distribution is solved for metamaterial absorbers using COMSOL Multiphysics.

Figure 9 shows the calculated steady-state temperature distributions in cross resonators generated by heat source from the dissipative energy for metamaterial absorbers with unit cell patterns of C, ADAD, ABCC and ABCD at different resonance wavelengths. It is noted that the 100 µm-thick silicon substrate is not shown in the plot. For a single-sized unit cell pattern of C shown in Figures 9(a1)-9(a2), a temperature variation range from 315 K to 320 K is found at $\lambda = 4.17$ µm and the highest temperature appears in the horizontal arm of the W cross resonator. A similar temperance range is found at λ =1.73 µm but with the highest temperature in the vertical arm of the W cross resonator. The magnitude of temperature distribution is consistent with the time-averaged

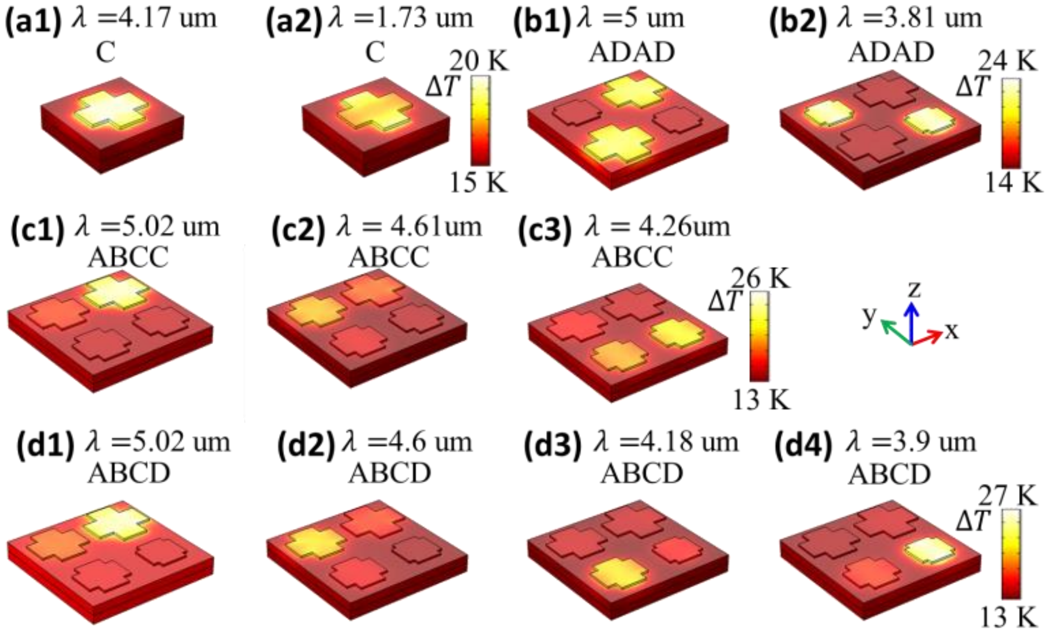

Figure 9. Temperature distributions at resonance. Temperature distributions for unit cell patterns of (a1, a2) C, (b1, b2) ADAD, (c1 - c3) ABCC and (d1 - d4) ABCD at different resonance wavelengths under TM polarized normal incidence. It is noted that the incident optical power density is 22.2 µW/µm^2 and the 100 µm-thick silicon substrate is not shown. The enhanced temperature is observed at the resonant cross resonator.

dissipative energy density Q_h serving as the heat source. For the double-sized unit cell patterns of ADAD, ABCC and ABCD, high temperature regions are distributed in the specific W cross resonators at certain resonance wavelengths. When comparing the temperature distribution of single-sized unit cell patterns of C at λ = 4.17 µm (with maximum T of 313 K and minimum T of 308 K) with double-sized unit cell pattern of ABCD at λ =4.18 µm (with maximum T of 314 K and minimum T of 306 K), one can find a relatively higher maximum temperature but a lower minimum temperature for the double-sized unit cell pattern, which is due to the coupling effects between neighboring cross resonators and hence a different heat dissipation environment for each type of unit cell pattern.

The designed W-based metamaterial absorbers and emitters can advance promising applications in thermal energy harvesting such as thermal photovoltaic (TPV) cells at the mid-infrared wavelength range. Different from conventional solar cells, many types of heat sources are available for TPV cells such as high-temperature combustion processes (typically above 2000 K) and low-temperature waste heat sources (typically in 600 K ~ 1300 K) from industries of glass, steel and paper [57,58]. High-temperature TPV cells are still difficult to implement in practice mainly due to the requirement of high-temperature enduring materials and thermal management [57]. Low-temperature TPV cells are important for energy recovery from waste heat sources and have been experimentally explored with low-bandgap semiconductor of InAs (0.32 eV) [58]. Alternative selections of low-bandgap semiconductors (0.18 eV – 0.35 eV), for instance,

Table 1. Physical properties of materials for heat transfer analysis.

	ρ(kg m^{-3})	C_p (J kg^{-1} K^{-1})	k_c(W m^{-1} K^{-1})
Tungsten	19300	132	52.2 (thickness, 200 nm) 17.4 (thickness, 50 nm)
Alumina	3970	765	1.6
Silicon	2330	712	148
Air	1	353 [K] / T	0.03

InSb (0.18 eV) [59], SnTe (0.18 eV) [60], PbTe (0.19 eV) [61], PbSe (0.26 eV ~ 0.29 eV) [62,63], InAsSb (0.29 eV) [64] and GaInAsSbP (0.35 eV) [65], have also been reported for designing practical low-temperature TPV cells.

The common configuration of the TPV cell has been schematically shown in the literature [8,13]. The energy conversion efficiency of TPV cells is mainly determined by both the thermal emission spectrum of the emitter and the semiconductor selection as pointed out from the detailed balance efficiency [8,10,66]. To simplify the problem, the photon recycling process of sub-bandgap photons or re-emitted photons can be ignored, which is considered as an improvement of the overall conversion efficiency [8]. It assumes that the quantum efficiency of the semiconductor exactly cuts off at the bandgap energy (E_g). Each photon with energy (ζ) greater than the bandgap energy can excite an electron-hole carrier pair with energy of E_g. The overall conversion efficiency of TPV cell η is evaluated as the fraction of converted electrical power to input power from thermal emitter, described by $\eta = U(T, E_g)\nu(T, E_g)M(V_{op})$ [8], where U is the ultimate conversion efficiency which imposes a cutoff on the irradiance power allowing to be converted from thermal emitter, ν takes account into the recombination process, and Mpresents the consideration on maximizing the overall conversion efficiency of the TPV cell by optimizing the selection of open-circuit voltage (V_{op}). As defined in [8],

$$U(T, E_g) = \frac{\int_0^{\pi/2} d\theta \sin(2\theta) \int_{E_g}^{\infty} d\zeta E_m(\zeta,\theta) I_{BB}(\zeta,T_e) E_g/\zeta}{\int_0^{\pi/2} d\theta \sin(2\theta) \int_0^{\infty} d\zeta E_m(\zeta,\theta) I_{BB}(\zeta,T_e)} \tag{1}$$

where $E_m(\zeta, \theta) = (< A_{TE}(\zeta, \theta) > +< A_{TE}(\zeta, \theta) >)/2$ is the emissivity obtained from polarization and incident angle averaged absorption spectra according to the Kirchhoff's law, $I_{BB} = 2\zeta^3/[h^3c^2(Exp(\frac{\zeta}{k_B T}) - 1))]$ is the spectral radiance of an ideal blackbody. It finds that the ultimate efficiency is highly dependent on the operating temperature and bandgap energy, which is essentially related with the power that can be used for electric generation. Optimum useful power is obtained when emissivity of designed selective emitter is matched to that of a blackbody. However, taking account into the recombination process and actual difference between open-circuit voltage V_{op} and bandgap voltage V_g, ultimate efficiency is reduced by the second term, expressed as [8]

$$v(T, E_g) = V_{op} \,/\, V_g = V_c \,/\, V_g \ln\left[f Q_e(T, E_g)/Q_c(T_c, E_g)\right] \tag{2}$$

Bandgap voltage is written as $V_g = E_g/e$, where e is an electron's charge; initial cell voltage at cell temperature T$_c$ is written as$V_c = k_B T_c/e$. The non-ideality factor f is usually set as 0.5 to consider the influence from non-radiative recombination and non-unity absorption in the TPV cell [8]. For the TPV cell, the fraction of incident photon number flux resulting from the designed emitter and an ideal blackbody at temperature of T$_c$ reads [8]

$$\frac{Q_e}{Q_c} = \left[\int_0^{\pi/2} d\theta \sin(2\theta) \int_{E_g}^{\infty} d\zeta \pi E_m(\zeta, \theta) I_{BB}\,(\zeta, T_e)/\zeta\right] \Big/ \left[\int_{E_g}^{\infty} d\zeta \pi I_{BB}\,(\zeta, T_c)/\zeta\right] \tag{3}$$

The last consideration is on impedance matching term M, aiming at maximizing the conversion efficiency by optimizing the selection of open-circuit voltage. The expression is given by [8]

$$M = z_m^2/[(1 + z_m - e^{-z_m})(z_m + \ln(1 + z_m))] \tag{4}$$

where z_m is solved from the relation $z_m + \ln(1 + z_m) = V_{op} \,/\, V_c$.

Figure 10 plots the distributions of ultimate efficiency U and overall conversion efficiency η as functions of the thermal emitter temperature and semiconductor bandgap energy. Compared to the unit cell pattern of D in Figure 10(b1), the high U region (over

0.5) for the unit cell pattern A in Figure 10(a1) is shifted to the area with lower bandgap energy and lower operating temperature. This is mainly because the energy matching condition between the wavelength-selective emissivity spectrum of the thermal emitter and the temperature dependent blackbody radiation spectrum [8]. The center emission wavelength for the emitter with unit cell pattern of A is around 5.5 μm (0.225 eV), which corresponds to the blackbody temperature of 530 K, giving the maximum *U* over 0.5 at temperature below 1000 K (even as low as 500 K) and semiconductor bandgap energy below 0.21 eV. While the emitter with unit cell pattern of D has the center emission wavelength around 3.5 μm (0.354 eV) corresponding to the blackbody temperature of

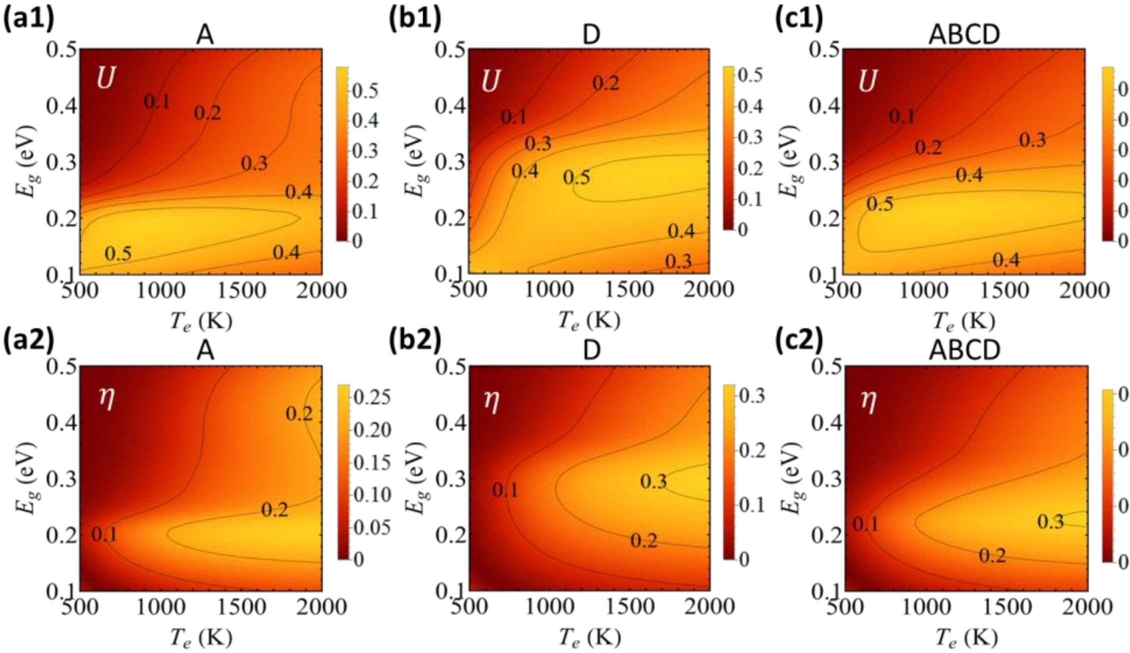

Figure 10. Ultimate conversion efficiency (*U*) as the function of thermal emitter temperature and the semiconductor band gap energy. Results for unit cell patterns of (a1) A, (b1) D and (c1) ABCD. Overall conversion efficiency (η) of the TPV system for unit cell patterns of (a2) A, (b2) D and (c2) ABCD.

830 K, the maximum U over 0.5 is located at temperature above 1150 K and semiconductor bandgap energy above 0.24 eV. Due to the fact that resonance wavelength of the emitter is located in the mid-infrared range, U is lower than the reported design in the near-infrared range [8], but the current thermal emitter design exhibits the advantage of operating at low temperature. For instance, an overall conversion efficiency η of 0.1 at temperature 685 K or η of 0.2 at temperature 1080 K can be enabled by using InSb (0.18 eV) with the unit cell pattern of A in Figure 10(a2). Also, the similar η value can be achieved by using InAsSb (0.29 eV) with the unit cell pattern of D in Figure 10(b2) at a relatively higher temperature. For the unit cell pattern of D, at the working temperature of 1800 K, η of 0.31 is obtained which is the same as the Shockley-Queisser limit of traditional solar cells. In Figure 10(c1), the emitter with double-sized unit cell pattern of ABCD shows a region with U over 0.5 at lower bandgap energy because of the dominant contribution from the unit cell pattern of A with the resonance wavelength around 5.5 µm. Also, one can find in Figure 10(c2) that the double-sized unit cell enables the TPV cells to operate at low emitter temperature with low semiconductor bandgap energy at the same time for achieving the same overall conversion efficiency. Therefore, the current mid-infrared metamaterial emitters based on multiple W cross resonators are promising in low-temperature waste heat recycling for low power electronic products.

5. CONCLUSION

In summary, single-sized and double-sized unit cells patterns with tungsten cross resonators have been demonstrated to realize wavelength-selective metamaterial absorbers and emitters in the mid-infrared range, with near-perfect single absorption peaks tunable from 3.5 µm to 5.5 µm and broadband absorption with bandwidth of about 1 µm within the wavelength range from 3 µm to 5.2 µm. The obtained absorption peak is mainly explained by the magnetic resonance supported in the cross resonator unit cells and the dispersion relation of unit cell array under both TM and TE polarizations. An equivalent RLC circuit model is developed to study the characteristics of absorption and impedance spectra for different unit cell patterns based on the magnetic resonance. Furthermore, heat generation and dissipation is analyzed for absorber applications. Thermal energy conversion efficiency is also calculated for realizing feasible TPV systems based on mid-infrared thermal emitter operating at low temperature with low-bandgap semiconductors for applications of low power electronics.

ACKNOWLEDGEMENTS

The authors acknowledge the facility support from the Materials Research Center at Missouri S&T. This work was performed, in part, at the Center for Nanoscale Materials, a U.S. Department of Energy Office of Science User Facility, and supported by the U.S. Department of Energy, Office of Science, under Contract No. DE-AC02-06CH11357.

REFERENCES

[1] S. B. Glybovski, S. A. Tretyakov, P. A. Belov, Y. S. Kivshar, and C. R. Simovski, "Metasurfaces: From Microwaves to Visible," Phys. Rep. 634, pp. 1–72, 2016.

[2] N. I. Landy, S. Sajuyigbe, J. J. Mock, D. R. Smith, and W. J. Padilla, "Perfect Metamaterial Absorber," Phys. Rev. Lett. 100, pp. 1–4, 2008.

[3] Y. Cui, Y. He, Y. Jin, F. Ding, L. Yang, Y. Ye, S. Zhong, Y. Lin, and S. He, "Plasmonic and Metamaterial Structures as Electromagnetic Absorbers," Laser Photonics Rev. 8, pp. 495–520, 2014.

[4] H. Deng, Z. Li, L. Stan, D. Rosenmann, and D. Czaplewski, "Broadband Perfect Absorber Based on One Ultrathin Layer of Refractory Metal," Opt. Lett. 40, pp. 2592–2595, 2015.

[5] C. M. Watts, D. Shrekenhamer, J. Montoya, G. Lipworth, J. Hunt, T. Sleasman, S. Krishna, D. R. Smith, and W. J. Padilla, "Terahertz Compressive Imaging with Metamaterial Spatial Light Modulators," Nat. Photonics 8, pp. 605–609, 2014.

[6] H. T. Miyazaki, T. Kasaya, M. Iwanaga, B. Choi, Y. Sugimoto, and K. Sakoda, "Dual-Band Infrared Metasurface Thermal Emitter for CO2sensing," Appl. Phys. Lett. 105, 2014.

[7] A. Lochbaum, Y. Fedoryshyn, A. Dorodnyy, U. Koch, C. Hafner, and J. Leuthold, "On-Chip Narrowband Thermal Emitter for Mid-IR Optical Gas Sensing," ACS Photonics 4, pp. 1371–1380, 2017.

[8] E. Rephaeli and S. Fan, "Absorber and Emitter for Solar Thermo-Photovoltaic Systems to Achieve Efficiency Exceeding the Shockley-Queisser Limit," Opt. Express 17, pp. 15145, 2009.

[9] H. A. Atwater and A. Polman, "Plasmonics for Improved Photovoltaic Devices," Nat. Mater. 9, pp. 205–213, 2010.

[10] C. Wu, B. Neuner, J. John, A. Milder, B. Zollars, S. Savoy, and G. Shvets, "Metamaterial-Based Integrated Plasmonic Absorber/Emitter for Solar Thermo-Photovoltaic Systems," J. Opt. 14, pp. 024005, 2012.

[11] S. Molesky, C. J. Dewalt, and Z. Jacob, "High Temperature Epsilon-near-Zero and Epsilon-near-Pole Metamaterial Emitters for Thermophotovoltaics.," Opt. Express 21 Suppl 1, pp. A96-110, 2013.

[12] J.-J. Greffet and M. Nieto-Vesperinas, "Field Theory for Generalized Bidirectional Reflectivity: Derivation of Helmholtz's Reciprocity Principle and Kirchhoff's Law," J. Opt. Soc. Am. A 15, pp. 2735, 1998.

[13] H. Deng, T. Wang, J. Gao, and X. Yang, "Metamaterial Thermal Emitters Based on Nanowire Cavities for High-Efficiency Thermophotovoltaics," J. Opt. (United Kingdom) 16, pp. 35102, 2014.

[14] H. Wang, V. Prasad Sivan, A. Mitchell, G. Rosengarten, P. Phelan, and L. Wang, "Highly Efficient Selective Metamaterial Absorber for High-Temperature Solar Thermal Energy Harvesting," Sol. Energy Mater. Sol. Cells 137, pp. 235–242, 2015.

[15] D. Woolf, J. Hensley, J. G. Cederberg, D. T. Bethke, A. D. Grine, and E. A. Shaner, "Heterogeneous Metasurface for High Temperature Selective Emission," Appl. Phys. Lett. 105, 2014.

[16] D. Costantini, A. Lefebvre, A. L. Coutrot, I. Moldovan-Doyen, J. P. Hugonin, S. Boutami, F. Marquier, H. Benisty, and J. J. Greffet, "Plasmonic Metasurface for Directional and Frequency-Selective Thermal Emission," Phys. Rev. Appl. 4, pp. 14023, 2015.

[17] H. Wang, Q. Chen, L. Wen, S. Song, X. Hu, and G. Xu, "Titanium-Nitride-Based Integrated Plasmonic Absorber/Emitter for Solar Thermophotovoltaic Application," Photonics Res. 3, pp. 329, 2015.

[18] C. M. Watts, X. Liu, and W. J. Padilla, "Metamaterial Electromagnetic Wave Absorbers," Adv. Mater. 24, pp. OP98-120, OP181, 2012.

[19] T. Inoue, M. De Zoysa, T. Asano, and S. Noda, "Realization of Narrowband Thermal Emission with Optical Nanostructures," Optica 2, pp. 27, 2015.

[20] K. Ikeda, H. T. Miyazaki, T. Kasaya, K. Yamamoto, Y. Inoue, K. Fujimura, T. Kanakugi, M. Okada, K. Hatade, and S. Kitagawa, "Controlled Thermal Emission of Polarized Infrared Waves from Arrayed Plasmon Nanocavities," Appl. Phys. Lett. 92, pp. 2006–2009, 2008.

[21] Y. X. Yeng, M. Ghebrebrhan, P. Bermel, W. R. Chan, J. D. Joannopoulos, M. Soljacic, and I. Celanovic, "Enabling High-Temperature Nanophotonics for Energy Applications," Proc. Natl. Acad. Sci. 109, pp. 2280–2285, 2012.

[22] J. G. Fleming, S. Y. Lin, I. El-Kady, R. Biswas, and K. M. Ho, "All-Metallic Three-Dimensional Photonic Crytal with a Large Infrared Bandgap," Nature 417, pp. 52–55, 2002.

[23] L. P. Wang and Z. M. Zhang, "Phonon Mediated Magnetic Polaritons in the Infrared Region," Opt. Express 19 Suppl 2, pp. A126-135, 2011.

[24] T. Inoue, M. De Zoysa, T. Asano, and S. Noda, "Single-Peak Narrow-Bandwidth Mid-Infrared Thermal Emitters Based on Quantum Wells and Photonic Crystals," Appl. Phys. Lett. 102, pp. 10–14, 2013.

[25] H. Wang and L. Wang, "Perfect Selective Metamaterial Solar Absorbers," Opt. Express 21, pp. A1078–A1093, 2013.

[26] X. Liu, T. Tyler, T. Starr, A. F. Starr, N. M. Jokerst, and W. J. Padilla, "Taming the Blackbody with Infrared Metamaterials as Selective Thermal Emitters," Phys. Rev. Lett. 107, 2011.

[27] Y. Cui, J. Xu, K. Hung Fung, Y. Jin, A. Kumar, S. He, and N. X. Fang, "A Thin Film Broadband Absorber Based on Multi-Sized Nanoantennas," Appl. Phys. Lett. 99, pp. 253101, 2011.

[28] A. Lefebvre, D. Costantini, I. Doyen, Q. Lévesque, E. Lorent, D. Jacolin, J.-J. Greffet, S. Boutami, and H. Benisty, "CMOS Compatible Metal-Insulator-Metal Plasmonic Perfect Absorbers," Opt. Mater. Express 6, pp. 2389, 2016.

[29] Y. Guo and Z. Jacob, "Thermal Hyperbolic Metamaterials," Opt. Express 21, pp. 15014, 2013.

[30] N. H. Shen, T. Koschny, M. Kafesaki, and C. M. Soukoulis, "Optical Metamaterials with Different Metals," Phys. Rev. B - Condens. Matter Mater. Phys. 85, 2012.

[31] C.-W. Cheng, M. N. Abbas, C.-W. Chiu, K.-T. Lai, M.-H. Shih, and Y.-C. Chang, "Wide-Angle Polarization Independent Infrared Broadband Absorbers Based on Metallic Multi-Sized Disk Arrays," Opt. Express 20, pp. 10376, 2012.

[32] A. K. Azad, W. J. M. Kort-Kamp, M. Sykora, N. R. Weisse-Bernstein, T. S. Luk, A. J. Taylor, D. A. R. Dalvit, and H. T. Chen, "Metasurface Broadband Solar Absorber," Sci. Rep. 6, pp. 20347, 2016.

[33] H. Deng, L. Stan, D. A. Czaplewski, J. Gao, and X. Yang, "Broadband Infrared Absorbers with Stacked Double Chromium Ring Resonators," Opt. Express 25, pp. 28295, 2017.

[34] S. He, F. Ding, L. Mo, and F. Bao, "Light Absorber with an Ultra-Broad Flat Band Based on Multi-Sized Slow-Wave Hyperbolic Metamaterial Thin-Films," Prog. Electromagn. Res. 147, pp. 69–79, 2014.

[35] D. Ji, H. Song, X. Zeng, H. Hu, K. Liu, N. Zhang, and Q. Gan, "Broadband Absorption Engineering of Hyperbolic Metafilm Patterns," Sci. Rep. 4, pp. 4498, 2014.

[36] J. Zeng, L. Li, X. Yang, and J. Gao, "Generating and Separating Twisted Light by Gradient-Rotation Split-Ring Antenna Metasurfaces," Nano Lett. 16, pp. 3101–3108, 2016.

[37] L. Sun, Z. Li, T. S. Luk, X. Yang, and J. Gao, "Nonlocal Effective Medium Analysis in Symmetric Metal-Dielectric Multilayer Metamaterials," Phys. Rev. B - Condens. Matter Mater. Phys. 91, 2015.

[38] Z. Li, W. Wang, D. Rosenmann, D. A. Czaplewski, X. Yang, and J. Gao, "All-Metal Structural Color Printing Based on Aluminum Plasmonic Metasurfaces," Opt. Express 24, pp. 20472, 2016.

[39] W. Wang, D. Rosenmann, D. A. Czaplewski, X. Yang, and J. Gao, "Realizing Structural Color Generation with Aluminum Plasmonic V-Groove Metasurfaces," Opt. Express 25, pp. 20454–20465, 2017.

[40] A. D. Rakić, A. B. Djurišić, J. M. Elazar, and M. L. Majewski, "Optical Properties of Metallic Films for Vertical-Cavity Optoelectronic Devices," Appl. Opt. 37, pp. 5271, 1998.

[41] J. Kischkat, S. Peters, B. Gruska, M. Semtsiv, M. Chashnikova, M. Klinkmüller, O. Fedosenko, S. Machulik, A. Aleksandrova, G. Monastyrskyi, Y. Flores, and W. Ted Masselink, "Mid-Infrared Optical Properties of Thin Films of Aluminum Oxide, Titanium Dioxide, Silicon Dioxide, Aluminum Nitride, and Silicon Nitride," Appl. Opt. 51, pp. 6789, 2012.

[42] J. B. Pendry, L. Martín-Moreno, and F. J. Garcia-Vidal, "Mimicking Surface Plasmons with Structured Surfaces," Science. 305, pp. 847–848, 2004.

[43] B. Zhao, L. Wang, Y. Shuai, and Z. M. Zhang, "Thermophotovoltaic Emitters Based on a Two-Dimensional Grating/Thin-Film Nanostructure," Int. J. Heat Mass Transf. 67, pp. 637–645, 2013.

[44] A. Barbara, S. Collin, C. Sauvan, J. Le Perchec, C. Maxime, J.-L. Pelouard, and P. Quémerais, "Plasmon Dispersion Diagram and Localization Effects in a Three-Cavity Commensurate Grating.," Opt. Express 18, pp. 14913–25, 2010.

[45] Y.-B. Chen and C.-J. Chen, "Interaction between the Magnetic Polariton and Surface Plasmon Polariton," Opt. Commun. 297, pp. 169–175, 2013.

[46] F. Costa, S. Genovesi, A. Monorchio, and G. Manara, "A Circuit-Based Model for the Interpretation of Perfect Metamaterial Absorbers," IEEE Trans. Antennas Propag. 61, pp. 1201–1209, 2013.

[47] A. Sakurai, B. Zhao, and Z. M. Zhang, "Resonant Frequency and Bandwidth of Metamaterial Emitters and Absorbers Predicted by an RLC Circuit Model," J. Quant. Spectrosc. Radiat. Transf. 149, pp. 33–40, 2014.

[48] Z. M. Zhang, *Nano/Microscale Heat Transfer* McGraw-Hill, 2007 .

[49] C. Batchelor and J. Hastings, *Waves and Fields in Bio-Ontologies* Prentice-Hall, 2012 , Vol. 897.

[50] G. Baffou, R. Quidant, and F. J. García De Abajo, "Nanoscale control of optical heating in complex plasmonic systems," in *ACS Nano* 2010 , Vol. 4, pp. 709–716.

[51] X. Chen, Y. Chen, M. Yan, and M. Qiu, "Nanosecond Photothermal Effects in Plasmonic Nanostructures," ACS Nano 6, pp. 2550–2557, 2012.

[52] I. Stark, M. Stordeur, and F. Syrowatka, "Thermal Conductivity of Thin Amorphous Alumina Films," Thin Solid Films 226, pp. 185–190, 1993.

[53] R. M. Costescu, D. G. Cahill, F. H. Fabreguette, Z. A. Sechrist, and S. M. George, "Ultra-Low Thermal Conductivity in W/Al2O3 Nanolaminates," Science. 303, pp. 989–990, 2004.

[54] J. Martan, N. Semmar, C. Boulmer-Leborgne, P. Plantin, and E. Le Menn, "Thermal Characterization of Tungsten Thin Films by Pulsed Photothermal Radiometry," Nanoscale Microscale Thermophys. Eng. 10, pp. 333–344, 2006.

[55] C. Ferrari, F. Melino, M. Pinelli, P. R. Spina, and M. Venturini, "Overview and status of thermophotovoltaic systems," in *Energy Procedia* 2014 , Vol. 45, pp. 160–169.

[56] A. Krier, M. Yin, A. R. J. Marshall, and S. E. Krier, "Low Bandgap InAs-Based Thermophotovoltaic Cells for Heat-Electricity Conversion," J. Electron. Mater. 45, pp. 2826–2830, 2016.

[57] C. Liu, Y. Li, and Y. Zeng, "Progress in Antimonide Based III-V Compound Semiconductors and Devices," Engineering 02, pp. 617–624, 2010.

[58] M. V. Kovalenko, W. Heiss, E. V. Shevchenko, J. S. Lee, H. Schwinghammer, A. P. Alivisatos, and D. V. Talapin, "SnTe Nanocrystals: A New Example of Narrow-Gap Semiconductor Quantum Dots," J. Am. Chem. Soc. 129, pp. 11354–11355, 2007.

[59] S. H. Wei and A. Zunger, "Electronic and Structural Anomalies in Lead Chalcogenides," Phys. Rev. B - Condens. Matter Mater. Phys. 55, pp. 13605–13610, 1997.

[60] W. H. Strehlow and E. L. Cook, "Compilation of Energy Band Gaps in Elemental and Binary Compound Semiconductors and Insulators," J. Phys. Chem. Ref. Data 2, pp. 163–200, 1973.

[61] J. Tang and E. H. Sargent, "Infrared Colloidal Quantum Dots for Photovoltaics: Fundamentals and Recent Progress," Adv. Mater. 23, pp. 12–29, 2011.

[62] M. G. Mauk and V. M. Andreev, "GaSb-Related Materials for TPV Cells," Semicond. Sci. Technol. 18, pp. S191, 2003.

[63] K. J. Cheetham, P. J. Carrington, N. B. Cook, and A. Krier, "Low Bandgap GaInAsSbP Pentanary Thermophotovoltaic Diodes," Sol. Energy Mater. Sol. Cells 95, pp. 534–537, 2011.

[64] W. Shockley and H. J. Queisser, "Detailed Balance Limit of Efficiency of P-n Junction Solar Cells," J. Appl. Phys. 32, pp. 510–519, 1961.

III. ENGINEERING THE THERMAL EMISSION VIA QUASI-PERIODIC METAL-DIELECTRIC MULTILAYER STACKS

Zhigang Li,[1] Liliana Stan,[2] David A. Czaplewski,[2] Xiaodong Yang,[1] and Jie Gao [1,*]

[1]Department of Mechanical and Aerospace Engineering, Missouri University of Science and Technology, Rolla, MO 65409, USA

[2]Center for Nanoscale Materials, Argonne National Laboratory, Argonne, IL 60439, USA

ABSTRACT

We theoretically and experimentally investigate thermal emission properties for three types of quasi-periodic metal-dielectric multilayer stacks: Periodic, Thue-Morse and Fibonacci multilayer stacks. Compared with local effective permittivity theory (EMT), nonlocal EMT shows efficient description of the effective permittivity parameters dispersion, providing a better way to characterize the optical topological transitions on the designed metamaterials. Epsilon-near-zero and Epsilon-near-pole behaviors are closely associated with the high absorptivity (emissivity). The enhancements of absorptivity or emissivity arise from surface plasmon polariton (SPP) modes and bulk plasmon polariton (BPP) modes formed by the coupling of SPP modes. Differences in the dispersion relations of SPP and BPP modes in the designed metamaterials are attributed to the existence of specific arrangement sequences of layers in the multilayer stacks, which are essential to control the thermal energy density distribution and thermal emission properties for selective thermal emitter design, attractive for wavelength selective sensing and energy harvesting.

1. INTRODUCTION

Going beyond the ability of traditional natural materials, artificially designed metamaterials are famous for their unique properties, which dramatically boost the development in a wide range of fields, covering perfect absorber based energy harvesting [1–3], selective thermal emission engineering [4–7], color printing and imaging at extremely nanoscale [8,9], and extreme sensitivity for bio-sensing [10]. In terms of thermal applications, metamaterials based thermophotovoltaic (TPV) method is receiving extensive attention as it is one excellent way to improve the high temperature energy conversion process, not only overcoming the upper limit on energy conversion for semiconductor cells, but also simplifying the design by efficient integration or modulation in real applications [11–14]. To maximize the efficiency of TPV approach, it is crucial to use an emitter with tunable thermal radiation spectrum lying within the operational wavelength compatible with the bandgaps of specific photovoltaic cells (typically 0.3 - 0.7 eV for low bandgap semiconductors [15,16]). To tailor the thermal emission spectrum for a narrow spectral range, four types of methods are mainly applied in terms of the materials, namely all-metallic [17–19], all-dielectric [20], metal-dielectric [4,5,25,26] and rare earth oxides [21] configurations. However, metal-dielectric multilayer metamaterials manifest the significant role in selective thermal emission engineering compared with other routes such as rare earth oxides limited by materials availability and complex composites [21], two dimensional or three dimensional photonic crystals limited by less sharp bands or low emissivity [17,18,22,23], gratings and meta-surfaces limited by complex fabrication techniques and large scale applications [4,5,20].

Periodic multilayer stacks are most prevailing multilayer metamaterials utilized to construct metamaterials composed of alternative arrangement of the layer A and layer B (for example, layer A is metal and layer B is dielectric or reversed allocation) [6,24,25]. Different from the periodic sequence, there exists two representative sequences of the quasiperiodic arrangements: Thue-Morse sequence and Fibonacci sequence. Thue-Morse sequence can be arranged in strings by the rule of Boolean complementary operation, such as $\mathrm{S}_n = \{S_{n-1}\mathrm{S}_{n-1}^{*}\}$ with $\mathrm{S}_0 = A$, $\mathrm{S}_0^{*} = B$, and 3rd generation term as $\mathrm{S}_3 = ABBABAAB$. Similarly, Fibonacci sequence is generated with the recursive formula given as $\mathrm{S}_n = \{S_{n-1}S_{n-2}\}$ with $\mathrm{S}_0 = B$ and $\mathrm{S}_1 = A$, yielding the 5th generation term as $ABAABABA$. Specific sequence of layers in the multilayer stack also produces significant differences on the optical properties, including modification of thermal radiation behaviors [26,27], localization properties of light [28,29], bandgap effects on the light transportation [30–32], second or high harmonic generation [33–36], and strong optical nonlocality [37]. Additionally, previous work on quasiperiodic multilayers are mainly basing on noble metals with low temperature stability [26,38], dielectric/semiconductor with low wavelength selectivity [28,30,32,33], which are not suitable for high temperature selective thermal emission engineering with high emittance and narrow band at near and middle infrared region. Furthermore, unique properties of metamaterials are supported by the hyperbolic iso-frequency surface, a spatial dispersion relation relating the momentum and energy of optical modes inside materials [39].

In this work, we focus on designing the high temperature selective thermal emitter based on quasiperiodic metal-dielectric multilayer stacks and investigating the thermal emission properties through modifying the arraignment sequence in multilayer stacks.

First, three types of multilayer stacks, Periodic multilayer (PM), Thue-Morse multilayer (ThM) and Fibonacci multilayer (FM), are designed and fabricated with the same metal filling ratio of refractory tungsten (W), respectively. The effective permittivity theory (EMT) is then employed for local and nonlocal analysis, revealing the Epsilon-near-zero behaviors associated with the optical topological transition in the iso-frequency surfaces of multilayer stacks. ENZ and Epsilon-near-pole (ENP) behaviors are also utilized to explain the high absorptivity (emissivity).The differences of the emissivity measured from the designed metamaterials are analyzed in terms of the effective group indexes, surface and bulk modes with respect to the transverse magnetic (TM) polarization.

2. METHODS AND EXPERIMENTAL PRODUCERS

Figures 1(a)–1(c) schematically illustrate periodic, Thue-Morse and Fibonacci multilayer stack, respectively. To explore the thermal emission properties of quasi-periodic metal-dielectric multilayer and influence from different arrangement sequences, the considered three types of multilayer stacks with gold substrate are fabricated on the silicon wafer, respectively. The multilayer stacks composed of refractory metal W and dielectric Si layers are deposited with specific sequence as periodic, Thue-Morse and Fibonacci, respectively. The gold substrate with thickness of 200 nm is added to block the light transmission in the spectrum region of mid-infrared and infrared studied in this work. In Figures 1(d)–1(f), it shows the scanning electron microscope (SEM) images of the cross section of PM, ThM and FM stacks, respectively, with gold substrate on the top of silicon wafer. All cross sections are obtained through cutting the multilayer stacks with focused ion beam (FIB) system (Helios Nanolab 600). The same filling ratio of metallic medium is initially designed for three types of multilayer stacks, which turns out to be 0.040 ± 0.005 in fabrication results; the thicknesses of W layer and Si layer varies over different layers and stacks. For theoretical calculation in this work, the optical constants of W, Si and Au are obtained from references [40,41]. Combining the results from SEM image measurement and numerical calculations, the thicknesses of W layer and Si layer are determined to be 8.9 ± 0.6 and 209.7 ± 3.5 nm for PM stack, 8.6 ± 1.4 and 180.1 ± 29.2 nm for ThM stack and 6.3 ± 2.3 and 183.9 ± 33.2 nm for FM stack, respectively. The existed variation in layer thicknesses causes slight modifications for three types of multilayer stacks in terms of the optical response; however, the specific features of three types of multilayer are captured in the experiment.

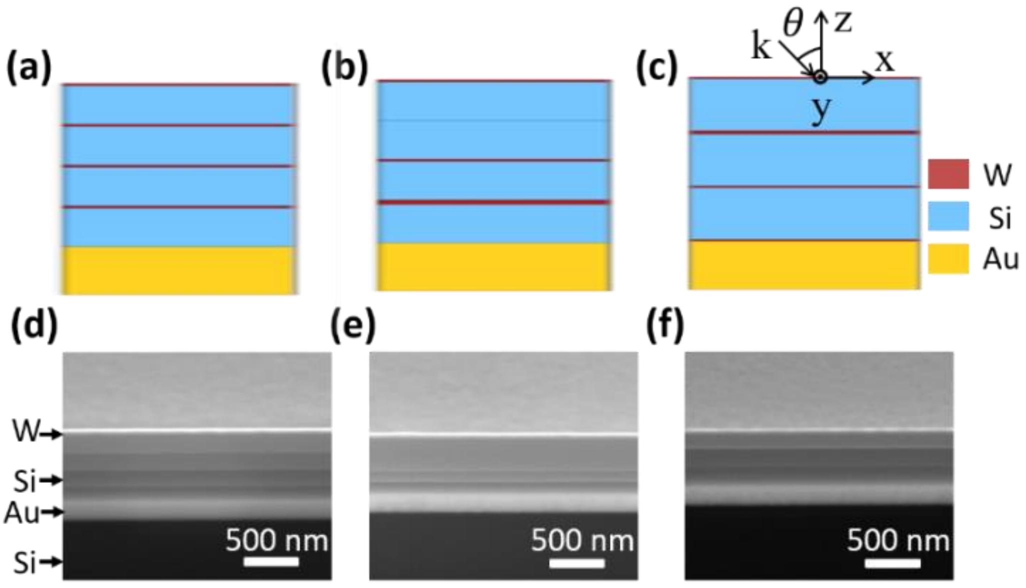

Figure 1. W-Si multilayer stacks in simulation and experiment. Schematic of W-Si multilayer stack with (a) periodic, (b) Thue-Morse and (c) Fibonacci sequence, respectively. SEM image of the cross section of (d) periodic, (e) Thue-Morse and (f) Fibonacci multilayer stack, respectively.

The absorptivity (unity minus the reflectivity) is indirectly obtained from the reflectivity measurement in the spectrum region of near-infrared and mid-infrared at room temperature by the Fourier transform infrared (FTIR) spectrometer (Nicolet 6700) with a nitrogen-purged mercury cadmium telluride (MCT) detector. The normalization is conducted using high-quality gold mirror as reference. Before the thermal emission measurement, all the prepared multilayer stacks are annealed at 400 K for 20 minutes in air to remove the pollutions and stabilize deposition layers in the samples. A thermal plate (DATAPLATE 730 Series Digital Hot Plates) with temperature controller is used for the annealing process and heating process for thermal emission measurement later. The emittance signals are collected by the FTIR spectrometer. To stabilize the emittance signal, the collection does not start until holding for 20 minutes at the desired measurement temperature. A black soot sample is used as reference sample which is prepared by direct deposition no to a clean silica glass slide using a candle with a deposition time larger than 20 minutes and then annealed at 500 K for 1 hour to purify and stabilize the black soot sample. The prepared black soot sample is able to achieve a high emissivity close to the ideal black body as reported in the reference [42,43].

3. COMPARISON OF ABSORPTIVITY AND EMISSIVITY IN THE DESIGNED METAMATERIALS

Consider the designed three types of multilayer stacks, which possess almost identical filling ratio of metallic medium. The almost same effective permittivity parameters are therefore expected for different multilayer stacks according to the local EMT theory [44]. The effective permittivity parameters ε_x^{loc} in the parallel direction and

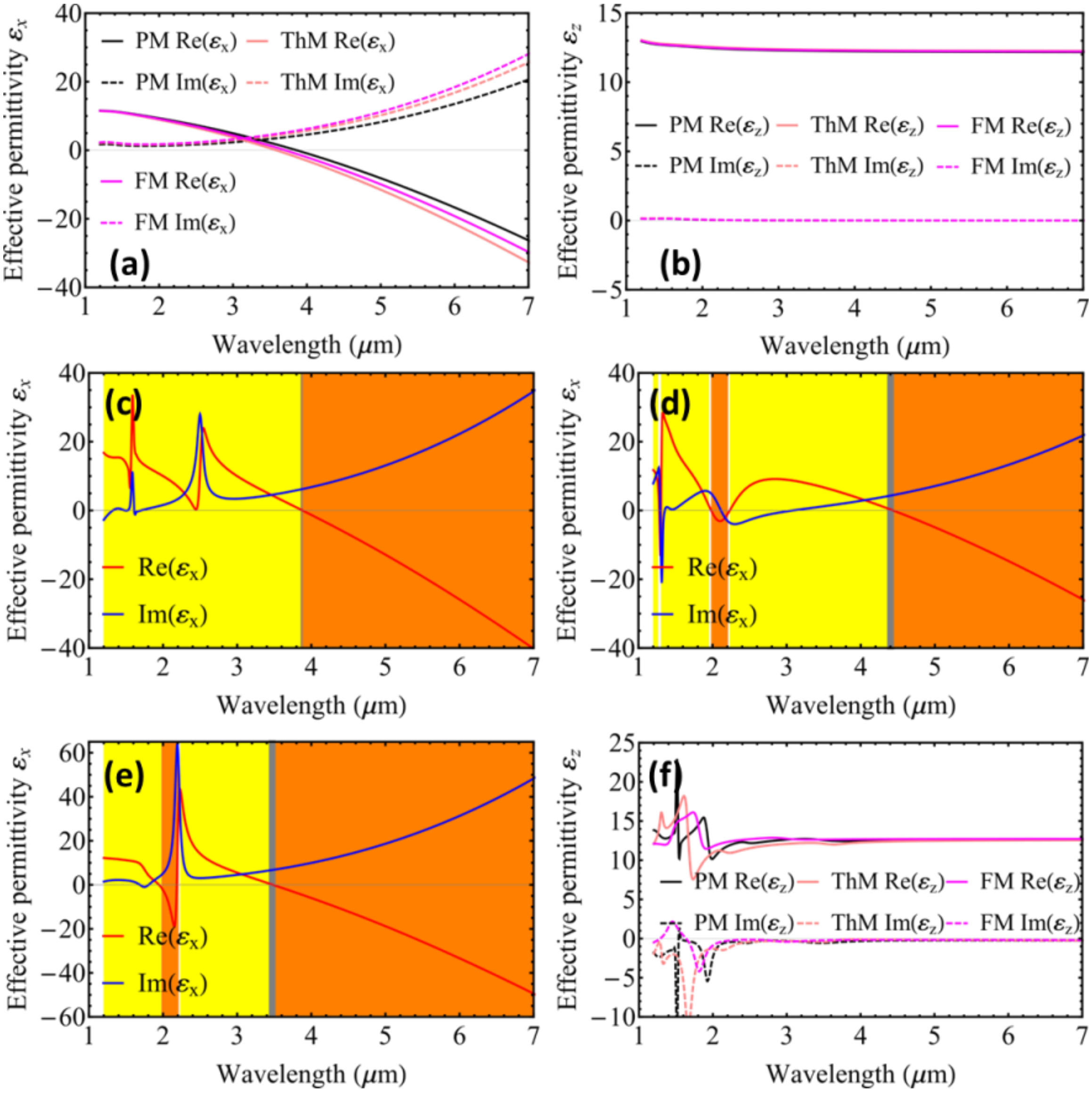

Figure 2. Effective medium analysis. Effective permittivity (a) ε_x and (b) ε_z of the PM, ThM and FM stacks based on the local effective medium theory. Effective permittivity (c)-(e) ε_x and (f) ε_z of the PM, ThM and FM stack, respectively, based on the nonlocal effective medium theory. For each type of stack, one specific topological transition region for is colored in gray with conventional anisotropic medium region shaded in yellow and hyperbolic medium region shaded in orange.

ε_z^{loc} in the normal direction of designed multilayer stacks are extracted as $\varepsilon_x^{loc} = \varepsilon_m f + \varepsilon_d(1-f)$ and $\varepsilon_z^{loc} = \varepsilon_m \varepsilon_d / [\varepsilon_d f + \varepsilon_m(1-f)]$, where $\mathrm{f} = a_m/(a_m + a_d)$ is the metal filling ratio. The calculation results are shown in Figures 2(a)–2(b), respectively. An overlap of effective permittivity dispersion is found for both ε_x^{loc} and ε_z^{loc} , though slight violations exist because of small variations among different stacks due to slight difference in filling ratios. Due to the limitations of local EMT in predicting the optical properties as discussed in literature [44], another analysis for the effective permittivity dispersion are performed based on the nonlocal EMT [45,46]. One representative method of nonlocal EMT is developed based on the original definition of effective permittivity as $\varepsilon_x^{nonloc} = \int_s D_x\, ds \Big/ \int_s E_x\, ds$ and $\varepsilon_z^{nonloc} = \int_s D_z\, ds \Big/ \int_s E_z\, ds$, integrated on the cross section of metamaterial [46], which is proved to be capable of efficiently calculating the optical characteristics of multilayer stacks. The nonlocal EMT is then employed to extract the effective permittivity parameters $\varepsilon_x^{\mathrm{non}loc}$ and ε_z^{nonloc} as shown in Figures 2(c)–2(f). Contributions from different arrangement sequences are significantly differed in the effective permittivity dispersion relationships for three types of multilayer stacks.

Furthermore, compared with the results of local EMT, nonlocal EMT provides better understanding on the effective permittivity dispersion relationship and optical topology transformation for the designed metamaterials. ENZ point serves as the separation position for conventional elliptical dispersion relation region (colored in yellow) and hyperbolic dispersion relation region (colored in orange*)*. A range of transformation region is obtained by varying the incident angle from normal to parallel, yielding the transformation region (colored in gray) from 3.860 to 3.882 μm for PM stack, 4.366 to 4.436 μm for ThM stack and 3.461 to 3.483 μm for FM stack. Additionally, ENP behaviors are also observed in the dispersion relation of effective permittivity parameters for three cases, which are associated with the low polarization sensitivity and omnidirectional high absorptivity or emissivity effect [24].

In Figure 3, it shows the experimental (blue) and calculated (red) absorptivity spectra of the PM, ThM and FM stacks at normal incidence under room temperature. Transfer matrix method [37] is applied to theoretically predict the absorptivity of designed metamaterials, whose permittivity parameters are considered to be temperature independent. For three types of multilayer stacks, differences in the absorptivity spectra reflect the optical response of specific arrangement sequence of layers. Specific arrangement sequences construct various Fabry-Perot (FP) resonators [47] within multilayer stacks. Consequently, the position and intensity of the resonance peaks on the absorptivity spectra are quite different among the designed metamaterials.

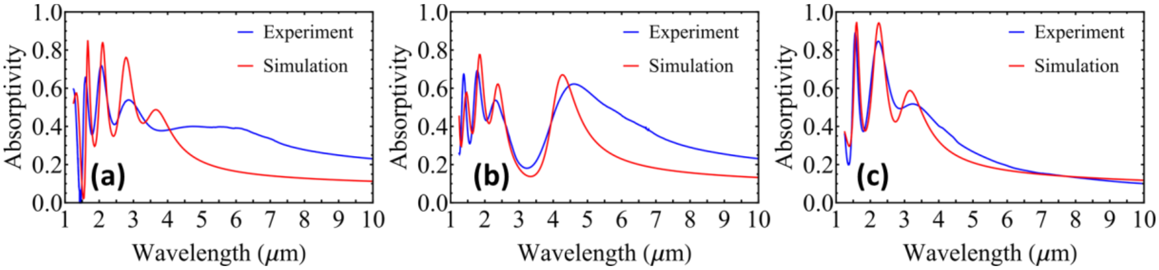

Figure 3. Absorptivity spectra of designed multilayer stacks. Experimental and calculated absorptivity spectra of the (a) PM, (b) ThM and (c) FM stacks at normal incidence.

ENZ and ENP region also play an important role on the formation of high absorptivity. For the calculated spectrum in Figure 3(b), large absorptivity is found at the wavelength of 4.27 µm lying at the proximity the ENZ wavelength. This resonance is derived from the impedance matching effect. Similar resonances are found at 3.676 µm for PM stack and 3.156 µm for FM stack, but with relatively lower absorptivity because of imperfect impedance match. Comparing with the relatively broad resonance from ENZ behavior, absorption resonance generated by ENP shows narrow band, such as the resonance at 2.791 μm for PM stack and 2.248 μm for FM stack. The ENP resonance arises from the regularized singularity with high loss, which reduces the impedance mismatch and enhances the absorptivity. The absorptivity is further enhanced by interactions from surface plasmon polaritons and bulk plasmon polaritons [48], which will be discussed in detail in the discussion section. Also, it is also immediately revealed by the Kirchhoff's law that high emissivity will be obtained at the wavelength of high absorptivity [49].

Based on the equivalence principle at thermal equilibrium state from the Kirchhoff's law, the expected emittance can be theoretically calculated by setting the formulation as $\mathrm{E}(\lambda, \theta, \varphi) = \mathrm{A}(\lambda, \theta, \varphi)$, where E denotes the emissivity and $\mathrm{A}(\lambda, \theta, \varphi)$ represents the optical absorptivity in terms of wavelength, azimuthal angle and polar angle. To validate thermal emission properties of designed metamaterials, the emittance of three types of multilayer stacks were directly measured at elevated temperatures. Also, aiming at exploring the stability and adaptability in the ambient atmospheres, thermal emission measurements are conducted in air at desired elevated temperatures. Thermal oxidation at high temperature will degrade the prepared samples and result in the distorted results in the experiment [6,19]; however, the serious degradation could be effectively prevented using an appropriate low temperature according to the Arrhenius law [50]. Consequently, 400 K is applied as highest temperature in current experiment considering the influence of thermal oxidation problem in the samples. More details about the temperature selection and validation will be addressed in the discussion section.

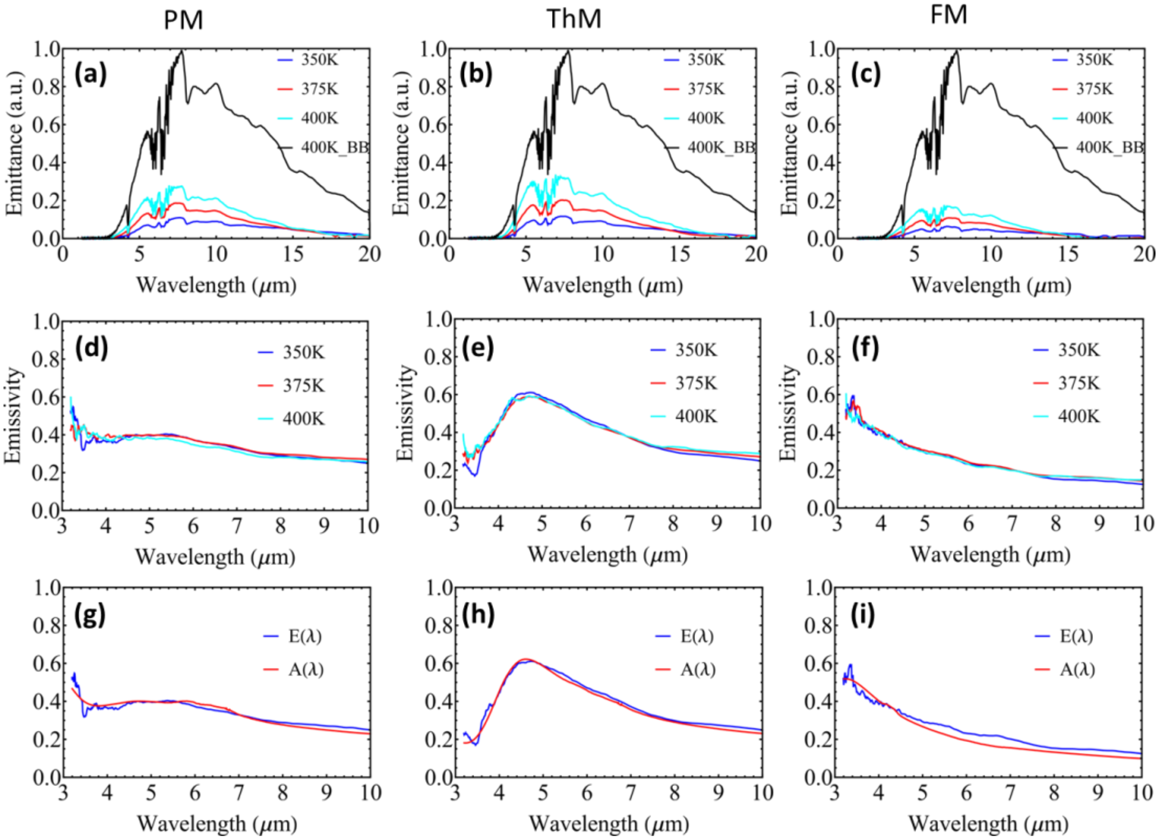

Figure 4. Comparison of emissivity and absorptivity. Experimental emittance of (a) PM, (b) ThM and (c) FM stacks at different temperatures, 350 K, 375 K and 400 K. The emittance of blackbody (BB) reference is given at 400 K. Normalized emissivity of (d) PM, (e) ThM and (f) FM stacks. Comparison of the emissivity measured at 350 K and absorptivity measured at room temperature of (g) PM, (h) ThM and (i) FM stacks.

Figures 4(a)–4(c) show the direct emittance measurement results at 350 K, 375 K and 400 K for PM, ThM and FM stack, respectively. The temperature dependent emittance shows increasing intensity for increasing temperature from 350 K to 400 K. Emissivity is then used to characterize the thermal emission spectra by normalization with black soot reference at corresponding temperatures, showing the results in Figures 4(d)–4(f). Here only show the emissivity spectra in the wavelength range from 3 µm to 10 µm because of the low single to noise ratio in the wavelength shorter than 3 µm, which is limited by the sensitivity of detector and FTIR spectrometer. In Figure 4(e), an emissivity peak is observed to be about 0.6 at the wavelength of 4.27 µm for the ThM stack, while most of the character emissivity peaks for PM and FM stacks are located before 3 µm outside of the measured spectra range. Some violations on the spectrum are attributed to deviations in the normalization process, thermal expansion of the dielectric layers [51] and thermal oxidation [6].

Comparisons are shown in Figures 4(g)–4(i) for the emissivity $\mathrm{E}(\lambda)$ measured at 350 K and absorptivity $\mathrm{A}(\lambda)$ measured at room temperature for three types of multilayer stacks. The measured emissivity and absorptivity curves show a good agreement both in the intensity and spectrum pattern, which is a direct validation of the Kirchhoff's law. Also, this work extends the ability to control the thermal emission with multilayer stacks by simply applying different arrangement sequence of layers, showing character thermal radiative properties for specific multilayer stacks.

4. DISPERSION RELATIONSHIP AND MODE ANALYSIS

The influence from different arrangement sequence of layers in the multilayer stacks can be explained through the dispersion relations in wave vector resolved space. To derive the dispersion relation of the designed metal-dielectric multilayer stacks, the transfer matrix method was applied for a propagating Block waves. Taking the TM polarization as an example [37], the tangential components of the electromagnetic filed at the two interfaces of the jth layer with the permittivity ε_j can be formulated as $\begin{pmatrix} E_z^j \\ H_y^j \end{pmatrix} =$

$\mathrm{M}^J \begin{pmatrix} E_z^{j+1} \\ H_y^{j+1} \end{pmatrix}$ with the transfer-matrix $\mathrm{M}^J = \begin{pmatrix} \cos[\phi] & -\mathrm{i}\sin[\phi]/\eta \\ -\mathrm{i}\sin[\phi]\eta & \cos[\phi] \end{pmatrix}$, where $\phi = 2\pi a_j \sqrt{\varepsilon_j {k_0}^2 - {k_x}^2}$, $\eta = \sqrt{\frac{\mu_0}{\varepsilon_0}} \sqrt{\varepsilon_j {k_0}^2 - {k_x}^2} / \varepsilon_j k_0$. ε_0 and μ_0 denote the permittivity and permeability of the vacuum. While the total transfer-matrix of the stack with N layers reads $\mathrm{M} = \prod_{j=1}^{N} \mathrm{M}^j$, and the Bloch type phase shift has a relation with the trace of the total transfer-matrix M written as $\cos\left[k_z \sum_{j=1}^{N} a_j\right] = \frac{1}{2} Tr(\mathrm{M})$. For simplification, normalization is applied by the W plasma frequency $\omega_\mathrm{p} = 2.005 \times 10^{16}\ \mathrm{rad/s}$ and the corresponding electromagnetic wave vector $\mathrm{k_p} = 6.69 \times 10^{7} \mathrm{m}^{-1}$.

For a fully understanding of the dispersion relation of designed multilayer stacks, we plot the wave vector resolved space in another two views, $\omega_0 - k_z$ and $\omega_0 - k_x$, to explore the on-axis and off-axis dispersion and band structures, respectively. First, let's see the dispersion relations in the $\omega_0 - k_z$ space. Figure 5(a) presents the calculated reflection spectra of designed metamaterials, in which the resonance peaks show a corresponding relation with bandgap edges in the band structure curves plotted both in the real and imaginary part. It is notable that the interested region is shaded in gray from 1.5 µm to 7 µm. In Figures 8(b)–8(c), band structure relationship is obviously altered both in real and imaginary part by the arrangement sequences in the multilayer stacks. The group velocity distribution shown in Figures 8(d) 8(e) is obtained by $v_g = d\omega_0/dk_z$ from band structure relationships. Negative group velocity is generated in the first Brillouin zone, accompanying with the sharp variation of group velocity in the vicinity of band edge. Large group velocity exceeding the light speed is considered as another feature of metamaterials. The effective group index $N_{effz} = c_0\, dk_z/d\omega_0$ is associated

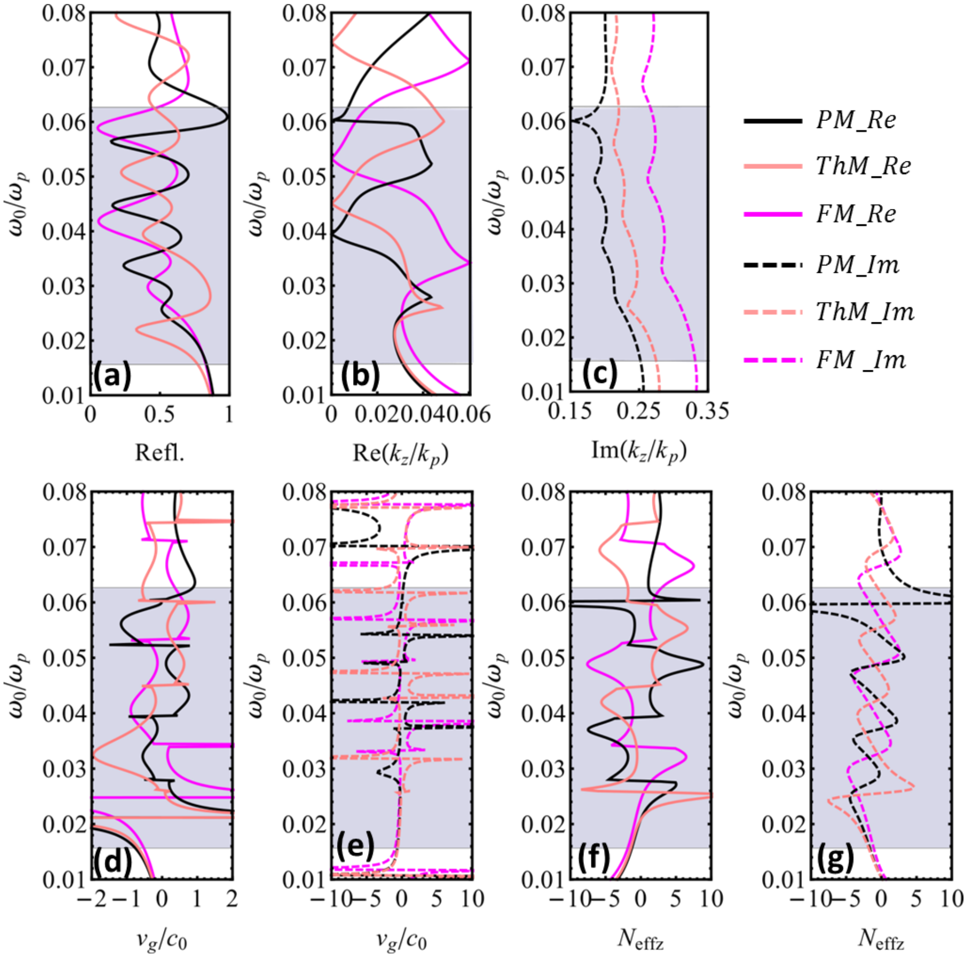

Figure 5. Band structure and group velocity. (a) Reflection and (b) real and (c) imaginary part of band structure at normal incidence for designed multilayer stacks. (d) Real and (e) imaginary part of group velocity distribution obtained from (b) and (c), respectively. (f) and (g) show real and imaginary part of effective group index distribution, respectively. An interested region is shaded in gray from 1.5 μm to 7 μm.

with the group velocity governing the optical pulse propagation in the medium. As seen in Figures 8(f)–8(g), when approaching the bandgap edges, the frequency dependent N_{effz} will be substantially increased, resulting in the high reflectivity; similarly, high absorptivity or low reflectivity in this work is observed with real part of N_{effz} approaches 1 while its imaginary part approaches the pole with negative value, enabling the impedance match with the refractive index of the air. Although the existence of a shift because of different length for the reciprocal lattice vectors, specific band structures are clearly observed in the wave vector resolved $\omega_0 - k_z$ space for three types of multilayer stacks, which are associated with the specific absorptivity properties and also the thermal radiative properties.

To further investigate the surface modes and bulk modes in the designed metamaterials, the dispersion curves bounded the bands are plotted in in Figures 6(a)–6(c) for PM, ThM and FM stack, respectively. SPPs are able to be thermally excited in the metal-dielectric multilayer metamaterials as the contribution of collective behavior the electrons oscillation in the multilayer stack [24,52]. The SSPs dispersion in the multilayer stack resides below the light line of dielectric. Light lines of air and Si are plotted according to the relation $\omega_0 = c_0/n\,k_x$, in which $n = n_{air}$ for air and $n = n_{Si}$ for Si. Above the light line of air, there are different branches (Group A) for each type of multilayer stack. If only consider the branches within the plot range, it finds four branches (A1 to A4) for PM stack, four branches (A1 to A4) for ThM stack and three branches (A1 to A3) for FM stack. The branches in group A are related with the dips on the absorption curves, while the branches in group B (B1 to B4) below the light line of dielectric are corresponding to the BPP modes associated with the metal layers. BPPs are induced from the coupling of SPPs between different multilayer interfaces in the multilayer stack [48]. Also, consider the classic expression for the propagation constant of SPP along the metal-dielectric interfaces: $k_x = \sqrt{\varepsilon_m \varepsilon_d/(\varepsilon_m + \varepsilon_d)}/k_0$, which is plotted as black dashed line in Figures 6(a)–6(c). SPP calculated from the classic expression is same for three types of multilayer stack since it only considers the interaction on one metal-dielectric interface; however BPP modes exhibit the discrepancy in the coupling of SPPs activated from different metal-dielectric interfaces. Variations in branches distribution and branch numbers of BPP modes show the influence of specific arrangement sequence of layers in different multilayer stacks. For example, the BPP dispersion curves (B2 branchs) is featured with different Ohmic damping effects from collective oscillation of electrons in the three types of multilayer stacks, which is associated with the influence of different SPPs couplings. The SPP coupling can be expressed as the generation of different modes split from the surface plasmon frequencies, symmetric or low–frequency mode with $\omega_{-} = \omega_{sp}\sqrt{1 - e^{-k_x a_m}/1 + \varepsilon_d}/\sqrt{1 + \varepsilon_d}$ and antisymmetric or high–frequency mode with $\omega_{+} = \omega_{sp}\sqrt{1 + e^{-k_x a_m}/1 + \varepsilon_d}/\sqrt{1 + \varepsilon_d}$, estimated for SSP with large wave vector [53]. Consequently, different SPP couplings are expected for the varying metal thicknesses of a_m because of the specific sequence of layers in the stack. Similarly, different characteristic propagation lengths of SPPs, described by $\delta_{SPP} = 1/[2Im(k_x)]$, can be found in different multilayer stacks, which are dominated by the imaginary part of the propagation constant [53].

Eigen modes analysis of the electromagnetic field is illustrated in Figure 6, corresponding to dispersion branches for each type of multilayer stack. Distribution of magnetic field intensity $|H_y|$ generated at eigenmode directly differs the electromagnetic wave interactions within multilayer stack composed of specific arrangement sequence of layers. Eigenmodes in Group A are the propagating modes through the multilayer stack, while the eigen modes in Group B are the localized electromagnetic fields caused from the coupling of SPP modes, distributed on the metal-dielectric interfaces in the stack. Again, the differences in the eigenmode analysis show the influence from specific arrangement sequence of layers in the multilayer stacks.

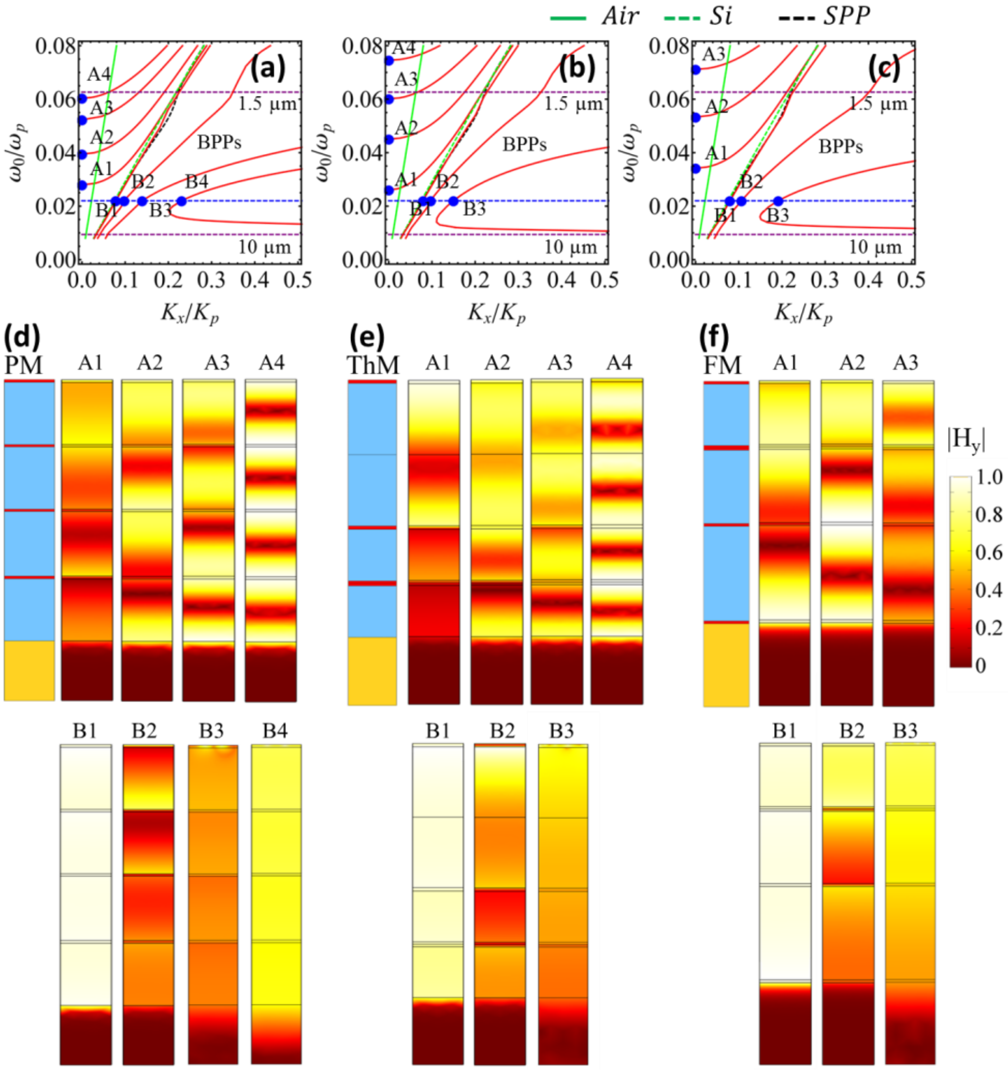

Figure 6. Dispersion and mode analysis. Dispersion diagram of (a) PM, (b) ThM and (c) FM stacks. (d). An interested region is bounded by the dashed purple curves at 1.5 μm and 10 μm, respectively and crossed by a dashed blue curve at 4.27 μm. Light lines are shown in solid green for air and in dashed green for Si. Eigen modes analysis is shown for the magnetic field intensity $|H_y|$of (d) PM, (e) ThM and (f) FM stacks regarding with the specific dispersion relation.

5. POLARIZATION AND ANGLE DEPENDENCE OF OPTICAL RESPONSE

Figures 7(a)–7(c) show the calculated polarization averaged absorptivity with the incident angle ranging from 0° to 80°for three types of multilayer stacks. According to

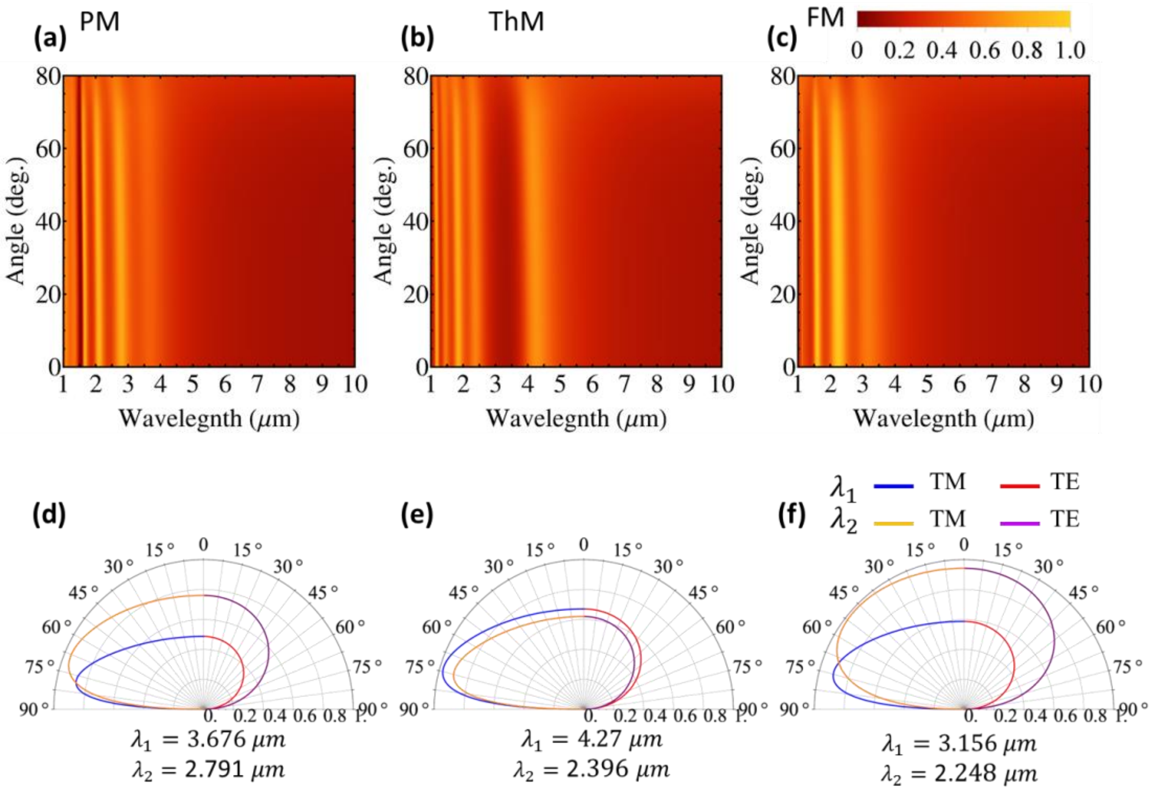

Figure 7. Absorption dependence on angle and polarization. Angle dependence of the polarization averaged absorptivity of (a) PM, (b) ThM and (c) FM stacks. Directional absorptivity for (d) PM, (e) ThM and (f) FM stacks at 3.676 µm, 4.27 µm and 3.156 µm, respectively. A second wavelength is selected at 2.791 µm, 2.396 µm and 2.248 µm for PM, ThM and FM, respectively. The TM polarization (blue and orange lines) shows stronger directional absorptivity ability compared with TE polarization (red and purple lines). Emissivity poses the identical angle dependence of absorptivity of multilayer stack according to the Kirchhoff's law.

the equivalence principle described by the Kirchhoff's law, unpolarized emissivity of the designed multilayer stacks exhibit incident angle dependence properties same as the polarization averaged absorptivity. Additionally, the polarized case is considered by plotting the polarized absorptivity spectra at two representative resonant wavelengths for each type of multilayer stack, as shown in Figures 7(d)–7(f). Different dependences of polarization and incident angle are observed for the absorptivity spectra for three types of multilayer stacks. The similarity is a directional absorptivity property appeared at large incident angle, about 75°, under the TM polarization at the wavelength of 3.676 µm for PM stack, 4.27 µm for ThM stack and 3.156 µm for FM stack. However, the absorptivity of FM stack shows independence of polarization and incident angle while maintaining high absorptivity for lower incident angles at wavelength of 2.248 µm due to the low polarization sensitivity and omnidirectional high emissivity effect of ENP resonance [24]. Influence of ENP resonance can also be observed for absorptivity of PM stack, but with less significance because of different permittivity dispersion at ENP resonance compared to the FM stack. Therefore, the specific sequence of layers in the multilayer stack greatly changes the polarization and angle dependence of optical response, from which polarized and directional properties can be achieved at a certain wavelength by constructing the multilayer stacks. Since the designed metamaterials are made of refractory metal W and high melting point dielectric Si, they are suitable to operate as thermal emitters at high temperature situations.

6. CONCLUSION

In this work, quasi-periodic metal-dielectric multilayer stacks are presented as an important role for the selective thermal emission engineering through the theoretically and experimentally investigation based on PM, ThM and FM stacks. Optical topological transitions are critical on these designed metamaterials, which are characterized by the nonlocal effective permittivity theory. ENZ and ENP behaviors showed association for the high absorptivity (emissivity). Dispersion relations of the designed metamaterials are analyzed in the wave vector resolved space. The space $\omega_0 - k_z$ shows high absorptivity or emissivity of metamaterials when effective group index N_{effz} with real part approaches one and imaginary part near negative pole. Meanwhile, in the space of $\omega_0 - k_x$, SPP modes and BPP modes enhance absorptivity or emissivity. The specific sequences in the arrangement of the multilayer stacks contribute to the variation of dispersion relationships and consequently the absorptivity or emissivity behaviors. These findings provide an alternative and flexible way to design the wavelength selective multilayer emitter and engineer the thermal emission spectrum at high temperature with metal-dielectric hyperbolic metamaterials.

ACKNOWLEDGEMENTS

The authors acknowledge the facility support from the Materials Research Center at Missouri S&T. This work was performed, in part, at the Center for Nanoscale Materials, a U.S. Department of Energy Office of Science User Facility, and supported by the U.S. Department of Energy, Office of Science, under Contract No. DE-AC02-06CH11357.

REFERENCES

[1] N. I. Landy, S. Sajuyigbe, J. J. Mock, D. R. Smith, and W. J. Padilla, "Perfect Metamaterial Absorber," Phys. Rev. Lett. 100, pp. 1–4, 2008.

[2] Y. Cui, Y. He, Y. Jin, F. Ding, L. Yang, Y. Ye, S. Zhong, Y. Lin, and S. He, "Plasmonic and Metamaterial Structures as Electromagnetic Absorbers," Laser Photonics Rev. 8, pp. 495–520, 2014.

[3] H. Deng, Z. Li, L. Stan, D. Rosenmann, and D. Czaplewski, "Broadband Perfect Absorber Based on One Ultrathin Layer of Refractory Metal," Opt. Lett. 40, pp. 2592–2595, 2015.

[4] X. Liu, T. Tyler, T. Starr, A. F. Starr, N. M. Jokerst, and W. J. Padilla, "Taming the Blackbody with Infrared Metamaterials as Selective Thermal Emitters," Phys. Rev. Lett. 107, pp. 4–7, 2011.

[5] D. Costantini, A. Lefebvre, A. L. Coutrot, I. Moldovan-Doyen, J. P. Hugonin, S. Boutami, F. Marquier, H. Benisty, and J. J. Greffet, "Plasmonic Metasurface for Directional and Frequency-Selective Thermal Emission," Phys. Rev. Appl. 4, pp. 14023, 2015.

[6] P. N. Dyachenko, S. Molesky, A. Y. Petrov, M. Störmer, T. Krekeler, S. Lang, M. Ritter, Z. Jacob, and M. Eich, "Controlling Thermal Emission with Refractory Epsilon-near-Zero Metamaterials via Topological Transitions," Nat. Commun. 7, pp. 11809, 2016.

[7] S. Campione, F. Marquier, J. P. Hugonin, A. R. Ellis, J. F. Klem, M. B. Sinclair, and T. S. Luk, "Directional and Monochromatic Thermal Emitter from Epsilon-near-Zero Conditions in Semiconductor Hyperbolic Metamaterials," Sci. Rep. 6, pp. 1–9, 2016.

[8] K. Kumar, H. Duan, R. S. Hegde, S. C. W. Koh, J. N. Wei, and J. K. W. Yang, "Printing Colour at the Optical Diffraction Limit," Nat. Nanotechnol. 7, pp. 557–561, 2012.

[9] Z. Li, W. Wang, D. Rosenmann, D. A. Czaplewski, X. Yang, and J. Gao, "All-Metal Structural Color Printing Based on Aluminum Plasmonic Metasurfaces," Opt. Express 24, pp. 20472, 2016.

[10] N. Liu, T. Weiss, M. Mesch, L. Langguth, U. Eigenthaler, M. Hirscher, C. Sönnichsen, and H. Giessen, "Planar Metamaterial Analogue of Electromagnetically Induced Transparency for Plasmonic Sensing," Nano Lett. 10, pp. 1103–1107, 2010.

[11] E. Rephaeli and S. Fan, "Absorber and Emitter for Solar Thermo-Photovoltaic Systems to Achieve Efficiency Exceeding the Shockley-Queisser Limit," Opt. Express 17, pp. 15145, 2009.

[12] P. Bermel, M. Ghebrebrhan, W. Chan, Y. X. Yeng, M. Araghchini, R. Hamam, C. H. Marton, K. F. Jensen, M. Soljačić, J. D. Joannopoulos, S. G. Johnson, and I. Celanovic, "Design and Global Optimization of High-Efficiency Thermophotovoltaic Systems," Opt. Express 18, pp. A314, 2010.

[13] V. Rinnerbauer, A. Lenert, D. M. Bierman, Y. X. Yeng, W. R. Chan, R. D. Geil, J. J. Senkevich, J. D. Joannopoulos, E. N. Wang, M. Soljačič, and I. Celanovic, "Metallic Photonic Crystal Absorber-Emitter for Efficient Spectral Control in High-Temperature Solar Thermophotovoltaics," Adv. Energy Mater. 4, 2014.

[14] H. Wang, V. Prasad Sivan, A. Mitchell, G. Rosengarten, P. Phelan, and L. Wang, "Highly Efficient Selective Metamaterial Absorber for High-Temperature Solar Thermal Energy Harvesting," Sol. Energy Mater. Sol. Cells 137, pp. 235–242, 2015.

[15] M. Bosi and C. Pelosi, "The Potential of III-V Semiconductors as Terrestrial Photovoltaic Devices," Prog. Photovoltaics Res. Appl. 15, pp. 51–68, 2007.

[16] V. Avrutin, N. Izyumskaya, and H. Morko, "Semiconductor Solar Cells: Recent Progress in Terrestrial Applications," Superlattices Microstruct. 49, pp. 337–364, 2011.

[17] V. Rinnerbauer, Y. X. Yeng, W. R. Chan, J. J. Senkevich, J. D. Joannopoulos, M. Soljačić, and I. Celanovic, "High-Temperature Stability and Selective Thermal Emission of Polycrystalline Tantalum Photonic Crystals," Opt. Express 21, pp. 11482, 2013.

[18] J. G. Fleming, S. Y. Lin, I. El-Kady, R. Biswas, and K. M. Ho, "All-Metallic Three-Dimensional Photonic Crytal with a Large Infrared Bandgap," Nature 417, pp. 52–55, 2002.

[19] H. Sai, Y. Kanamori, and H. Yugami, "High-Temperature Resistive Surface Grating for Spectral Control of Thermal Radiation," Appl. Phys. Lett. 82, pp. 1685–1687, 2003.

[20] J. J. Greffet, R. Carminati, K. Joulain, J. P. Mulet, S. Mainguy, and Y. Chen, "Coherent Emission of Light by Thermal Sources," Nature 416, pp. 61–64, 2002.

[21] G. Torsello, M. Lomascolo, A. Licciulu, D. Diso, S. Tundo, and M. Mazzer, "The Origin of Highly Efficient Selective Emission in Rare-Earth Oxides for Thermophotovoltaic Applications," Nat. Mater. 3, pp. 632–637, 2004.

[22] M. Laroche, R. Carminati, and J. J. Greffet, "Coherent Thermal Antenna Using a Photonic Crystal Slab," Phys. Rev. Lett. 96, 2006.

[23] T. Asano, K. Mochizuki, M. Yamaguchi, M. Chaminda, and S. Noda, "Spectrally Selective Thermal Radiation Based on Intersubband Transitions and Photonic Crystals.," Opt. Express 17, pp. 19190–19203, 2009.

[24] S. Molesky, C. J. Dewalt, and Z. Jacob, "High Temperature Epsilon-near-Zero and Epsilon-near-Pole Metamaterial Emitters for Thermophotovoltaics," Opt. Express 21, pp. A96, 2013.

[25] A. Narayanaswamy and G. Chen, "Thermal Emission Control with One-Dimensional Metallodielectric Photonic Crystals," Phys. Rev. B - Condens. Matter Mater. Phys. 70, pp. 1–4, 2004.

[26] F. F. De Medeiros, E. L. Albuquerque, M. S. Vasconcelos, and P. W. Mauriz, "Thermal Radiation in Quasiperiodic Photonic Crystals with Negative Refractive Index," J. Phys. Condens. Matter 19, pp. 496212, 2007.

[27] E. Maciá, "Thermal Emission Control via Bandgap Engineering in Aperiodically Designed Nanophotonic Devices," Nanomaterials 5, pp. 814–825, 2015.

[28] W. Gellermann, M. Kohmoto, B. Sutherland, and P. C. Taylor, "Localization of Light Waves in Fibonacci Dielectric Multilayers," Phys. Rev. Lett. 72, pp. 633–636, 1994.

[29] N. hua Liu, "Propagation of Light Waves in Thue-Morse Dielectric Multilayers," Phys. Rev. B - Condens. Matter Mater. Phys. 55, pp. 3543–3547, 1997.

[30] L. Dal Negro, C. J. Oton, Z. Gaburro, L. Pavesi, P. Johnson, A. Lagendijk, R. Righini, M. Colocci, and D. S. Wiersma, "Light Transport through the Band-Edge States of Fibonacci Quasicrystals," Phys. Rev. Lett. 90, pp. 4, 2003.

[31] L. Moretti, I. Rea, L. Rotiroti, I. Rendina, G. Abbate, A. Marino, and L. De Stefano, "Photonic Band Gaps Analysis of Thue-Morse Multilayers Made of Porous Silicon.," Opt. Express 14, pp. 6264–72, 2006.

[32] L. Dal Negro, M. Stolfi, Y. Yi, J. Michel, X. Duan, L. C. Kimerling, J. LeBlanc, and J. Haavisto, "Photon Band Gap Properties and Omnidirectional Reflectance in Si/SiO2Thue-Morse Quasicrystals," Appl. Phys. Lett. 84, pp. 5186–5188, 2004.

[33] X. B. Cai and X. F. Xuan, "Optical Harmonic Generation in a Fibonacci Dielectric Superlattice of LiNbO3," Opt. Commun. 240, pp. 227–233, 2004.

[34] A. Bahabad, O. Cohen, M. M. Murnane, and H. C. Kapteyn, "Quasi-Periodic and Random Quasi-Phase Matching of High Harmonic Generation," Opt. Lett. 33, pp. 1936, 2008.

[35] L. Wang, X. Yang, and T. Chen, "Second Harmonic Generation in Generalized Thue-Morse Ferroelectric Superlattices," Phys. B Condens. Matter 404, pp. 3425–3430, 2009.

[36] A. Arie and N. Voloch, "Periodic, Quasi-Periodic, and Random Quadratic Nonlinear Photonic Crystals," Laser Photonics Rev. 4, pp. 355–373, 2010.

[37] S. Savoia, G. Castaldi, and V. Galdi, "Optical Nonlocality in Multilayered Hyperbolic Metamaterials Based on Thue-Morse Superlattices," Phys. Rev. B - Condens. Matter Mater. Phys. 87, 2013.

[38] Y. Moritake, K. Nakayama, T. Suzuki, H. Kurosawa, T. Kodama, S. Tomita, H. Yanagi, and T. Ishihara, "Lifetime Reduction of a Quantum Emitter with Quasiperiodic Metamaterials," Phys. Rev. B - Condens. Matter Mater. Phys. 90, pp. 75146, 2014.

[39] H. N. S. Krishnamoorthy, Z. Jacob, E. Narimanov, I. Kretzschmar, and V. M. Menon, "Topological Transitions in Metamaterials," Science. 336, pp. 205–209, 2012.

[40] C. D. Salzberg and J. J. Villa, "Infrared Refractive Indexes of Silicon Germanium and Modified Selenium Glass*," J. Opt. Soc. Am. 47, pp. 244, 1957.

[41] A. D. Rakić, A. B. Djurišić, J. M. Elazar, and M. L. Majewski, "Optical Properties of Metallic Films for Vertical-Cavity Optoelectronic Devices," Appl. Opt. 37, pp. 5271, 1998.

[42] N. Gao, H. Sun, and D. Ewing, "Heat Transfer to Impinging Round Jets with Triangular Tabs," Int. J. Heat Mass Transf. 46, pp. 2557–2569, 2003.

[43] M. Paven, P. Papadopoulos, L. Mammen, X. Deng, H. Sachdev, D. Vollmer, and H. J. Butt, "Optimization of Superamphiphobic Layers Based on Candle Soot," Pure Appl. Chem. 86, pp. 87–96, 2014.

[44] O. Kidwai, S. V. Zhukovsky, and J. E. Sipe, "Effective-Medium Approach to Planar Multilayer Hyperbolic Metamaterials: Strengths and Limitations," Phys. Rev. A - At. Mol. Opt. Phys. 85, 2012.

[45] A. V. Chebykin, A. A. Orlov, A. V. Vozianova, S. I. Maslovski, Y. S. Kivshar, and P. A. Belov, "Nonlocal Effective Medium Model for Multilayered Metal-Dielectric Metamaterials," Phys. Rev. B 84, pp. 115438, 2011.

[46] L. Sun, Z. Li, T. S. Luk, X. Yang, and J. Gao, "Nonlocal Effective Medium Analysis in Symmetric Metal-Dielectric Multilayer Metamaterials," Phys. Rev. B - Condens. Matter Mater. Phys. 91, 2015.

[47] E. Nefzaoui, J. Drevillon, and K. Joulain, "Selective Emitters Design and Optimization for Thermophotovoltaic Applications," J. Appl. Phys. 111, 2012.

[48] I. Avrutsky, I. Salakhutdinov, J. Elser, and V. Podolskiy, "Highly Confined Optical Modes in Nanoscale Metal-Dielectric Multilayers," Phys. Rev. B - Condens. Matter Mater. Phys. 75, 2007.

[49] J.-J. Greffet and M. Nieto-Vesperinas, "Field Theory for Generalized Bidirectional Reflectivity: Derivation of Helmholtz's Reciprocity Principle and Kirchhoff's Law," J. Opt. Soc. Am. A 15, pp. 2735, 1998.

[50] K. J. Laidler, "The Development of the Arrhenius Equation," J. Chem. Educ. 61, pp. 494, 1984.

[51] H. Watanabe, N. Yamada, and M. Okaji, "Linear Thermal Expansion Coefficient of Silicon from 293 to 1000 K," Int. J. Thermophys. 25, pp. 221–236, 2004.

[52] Y. Guo, C. L. Cortes, S. Molesky, and Z. Jacob, "Broadband Super-Planckian Thermal Emission from Hyperbolic Metamaterials," Appl. Phys. Lett. 101, 2012.

[53] S. A. Maier, *Plasmonics: Fundamentals and Applications*, 1st ed. Springer US, 2007.

IV. BROADBAND INFRARED BINARY-PATTERN METASURFACE ABSORBERS WITH MICRO GENETIC ALGORITHM OPTIMIZATION

Zhigang Li,[1] Liliana Stan,[2] David A. Czaplewski,[2] Xiaodong Yang,[1] and Jie Gao [1,*]

[1]Department of Mechanical and Aerospace Engineering, Missouri University of Science and Technology, Rolla, MO 65409, USA

[2]Center for Nanoscale Materials, Argonne National Laboratory, Argonne, IL 60439, USA

ABSTRACT

Broadband binary-pattern metasurface absorbers are designed and demonstrated in the mid-infrared wavelength range through the micro genetic algorithm. The tungsten-based metasurface absorbers with the optimized binary-pattern nanostructures exhibit broadband near-perfect absorption due to the multiple plasmonic resonances supported within the unit cell. Furthermore, the influence of minor pixel modifications in the optimized binary-pattern nanostructures on the absorption performance is investigated in experiment. This work presents a promising approach to design and optimize complex optical nanostructures with the desired properties for metamaterial and metasurface applications.

1. INTRODUCTION

Electromagnetic metamaterial absorbers have been receiving great interest since the first demonstration of the perfect absorption properties [1]. Metamaterial absorbers have been designed to realize broadband or narrowband absorption at wavelengths from visible to infrared [2]. Various geometries have been used to design broadband metamaterial absorbers, mainly including multilayer films based on impedance match theory [3], metal-dielectric-metal structures with multiple resonators [4], structured multilayer gratings [5], and hybrid structures with multiple absorption mechanisms [6]. These metamaterial absorbers are constrained by the manual design process with limited geometry complexity and tedious parameters sweeping. Several optimization methods have been proposed to simplify the nanostructure design, including gradient-based methods [7], evolutionary models such as genetic algorithms [8–10], particle swarm optimization [11] and non-deterministic quasi-random method [12]. Genetic algorithms have been proved to be an efficient approach for the absorber design [8–10,13]. Starting from one random distribution of materials selection, the genetic algorithm searches the optimal distribution through the steps in the crossover of parents' information, evaluating the offspring's information, and repeating the loop over until reaching the stop criteria. Furthermore, micro genetic algorithm (micro-GA) is a modified genetic algorithm by adding the option of restarting the initialization of population, which requires a smaller initial population and converges faster than the traditional genetic algorithm, making this method appealing in real applications [8].

In this work, micro-GA is employed to design the broadband mid-infrared binary-pattern metasurface absorbers. The tungsten-based structure is selected for the optimization towards broadband near-perfect absorption. The optimized binary-pattern nanostructures within the unit cell support multiple plasmonic resonances to achieve broadband absorption. The effects of minor pixel modifications in the optimized nanostructures on the absorption performance are further investigated. This work provides an effective method to optimize the complex metamaterial and metasurface nanostructures with the desired properties.

2. FORMULATION OF STRUCTURAL DESIGN WITH MICRO GENETIC ALGORITHM

In the micro-GA method, the binary-pattern nanostructure is encoded into the chromosome with binary numbers defined as either material (“1”) or free space (“0”). To enable the evolutionary optimization toward the optimal result, the fitness function is defined as $F = \sum_{\theta} \sum_{\lambda} (1 - A_{TM})^2 + (1 - A_{TE})^2$ to evaluate the absorption property for each binary-pattern nanostructure, where A_{TM} and A_{TE} are the absorption under TM and TE polarization at a certain incident angle θ. Thus, the design problem of binary-pattern nanostructure is formulated as the minimization of the fitness function F subject to $\nabla \times \nabla \times \boldsymbol{E} - \mu\omega^2 \epsilon \boldsymbol{E} = 0$ and $\nabla \cdot \epsilon \boldsymbol{E} = 0$, where $\boldsymbol{E}$, ϵ, μ denote the electric field, permittivity and permeability in the unit cell. Periodic boundary conditions are applied around the unit cell in simulation using COMSOL software. The fitness value F is then extracted from the simulated absorption spectra for each obtained binary-pattern nanostructure and it is further evaluated to stop or start new calculation loops according to the criteria conditions.

The optimization target is to obtain the absorption above 0.9 at the selected 12 equally-spaced wavelengths from 2 μm to 4 μm at two incident angles of $0^{\circ}$and 45°. The binary-pattern nanostructure is encoded with an 11 by 11 array with “1”s and “0”s, where the 8-fold mirror symmetry is applied to enable polarization independence and to shorten the chromosome string. Due to the advantages of micro-GA in searching solutions, a population of 5 chromosomes is used with the tournament selection for crossover [8–10]. No mutation step is required since the repopulation step after reaching a value of the similarity among chromosomes will significantly accelerate the evolution progress. The two optimized patterns presented in this work both start from random structures initially and converge to the fitness values satisfying design target within 35 generations. It takes around 72 hours to get the result of Pattern A0 by using the computer with 2 processors of the Intel(R) Xeon(R) CPU E5645. No fillet operation is conducted to the pattern due to its negligible contribution to the absorption performance in this work.

3. DESIGNED METAMATERIALS TOWARD BROADBAND ABSORBER

Figure 1(a) shows the schematic of the optimized binary-pattern nanostructure pattern A0 in the unit cell through the micro-GA, with the top view shown in Figure 1(b) where the dashed blue lines mark the cross section locations for optical field analysis in Figure 2 The multilayer is composed of a top 45 nm-thick tungsten (W) layer, a 220 nm-thick alumina (Al_2O_3) spacer layer and a 200 nm-thick tungsten ground plane on a silicon substrate, denoted as t_h, t_d and t_m, respectively. Tungsten is used for its high intrinsic loss and the extended operating temperature due to high temperature enduring ability, making it potential for absorber design [4]. The pattern A0 in the unit cell is made of an 11 by 11 square pixel array filled with either W or air based on the optimization result with pixel width w of 100 nm. The tungsten ground plane is thick enough to effectively block the transmission so that the absorption is calculated as unity minus the reflection.

The W-Al_2O_3-W multilayer stack was deposited on a silicon substrate by RF sputtering. Both, W and Al_2O_3, were grown in Ar atmosphere at 6.5 mTorr and 5 mTorr, respectively. The deposition rates were 0.75 Å / sec for W and 0.08 Å / sec for Al_2O_3. The designed binary-pattern nanostructure was then fabricated with focused ion beam (FIB) milling on the top tungsten layer. Figure 1(c) shows a scanning electron microscopy (SEM) image of the fabricated pattern A0 array. Variations in the FIB milling process cause the 100 nm pixels to vary by ± 8 nm. The unpolarized reflection spectrum is measured at normal incidence with Fourier transform infrared spectroscopy (FTIR). The measured absorption spectrum for the fabricated pattern A0 array is plotted in Figure 1(d), showing that broadband near-perfect absorption is obtained with the

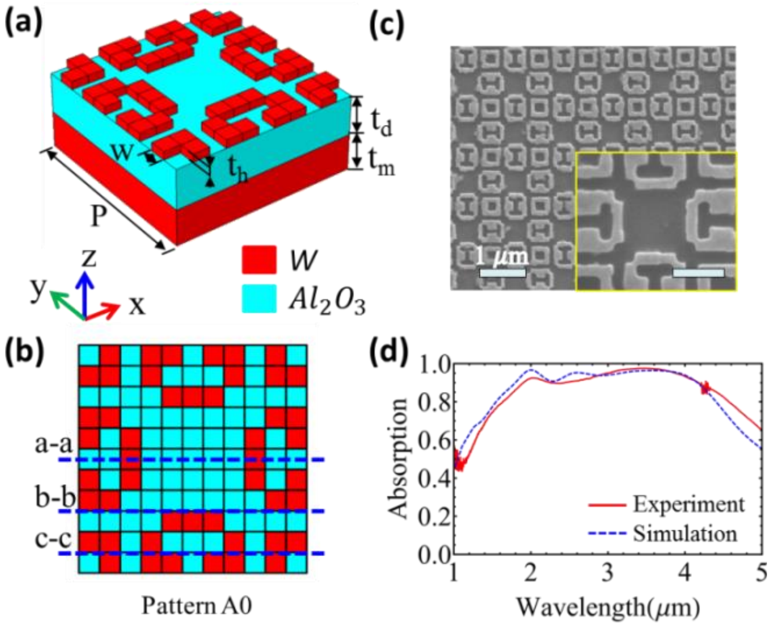

Figure 1. Designed binary-pattern absorber. Schematic of the optimized binary-pattern A0 in the unit cell and top view shown in (a-b). (c) SEM images of the pattern A0 array. Insert image scale bar: 400 nm. (d) Measured and simulated broadband absorption from the pattern A0 array under unpolarized normal incidence.

absorption over 0.9 from 1.9 μm to 4.2 μm and over 0.95 from 3 μm to 3.9 μm. The simulated absorption spectrum with the averaged polarization matches the experimental data well, where in simulation the permittivity parameters of W and Al_2O_3 are taken from Rakic [14] and Kischkat [15], respectively.

In order to understand the mechanism of broadband absorption for the optimized pattern A0, optical mode analysis is conducted at the three resonance wavelengths (λ = 2.02 μm, 2.58 μm and 3.65 μm) as shown in Figure 2. Figures 2(a1)–(a3) show the top

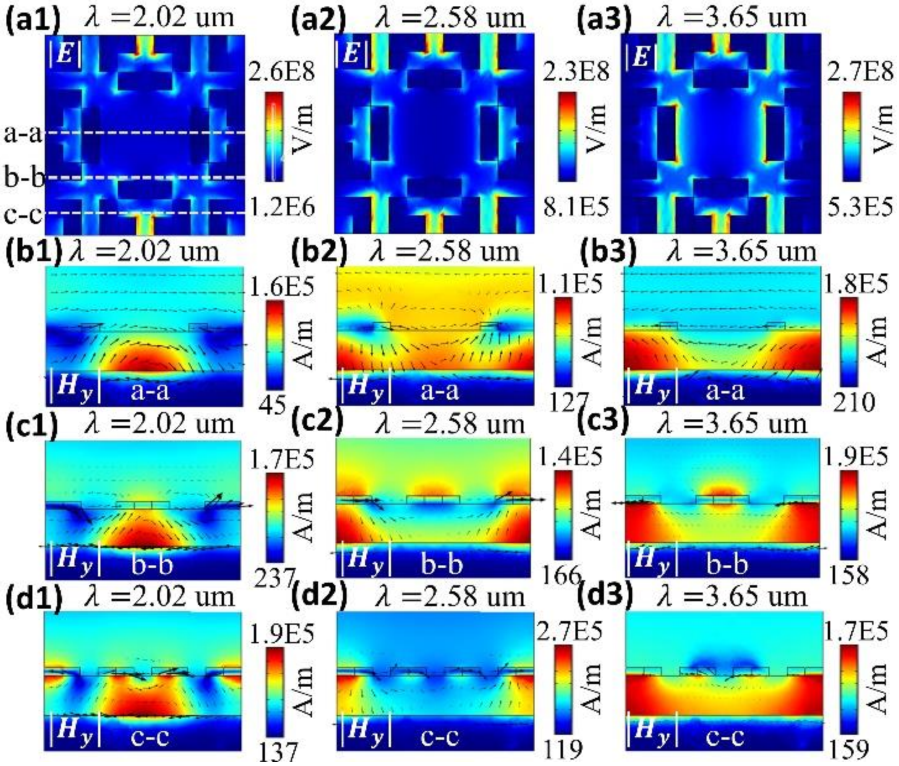

Figure 2. Mode analysis of designed absorber. Top view of the electric field |*E*| distributions at the top W surface of pattern A0 at λ = 2.02, 2.58 and 3.65 μm shown in (a1)-(a3). Cross section view of the magnetic field $|H_y|$ distributions at the locations of (b1)–(b3) a-a, (c1)–(c3) b-b and (d1)–(d3) c-c under TM polarization at normal incidence. Black arrows depict the direction and magnitude of the induced electric current density.

view of the electric field |E| distributions at the top W surface with normal incidence under TM polarization. It shows that the electric field distributions are enhanced at certain locations of the nanostructure at different resonance wavelengths. These multiple plasmonic resonances are also observed from the magnetic field |H_y| distributions in Figures 2(b1)–2(b3), Figures 2(c1)–2(c3) and Figure 2(d1)–2(d3) at the cross sections of a-a b-b and c-c, respectively. The black arrows plotted in the magnetic fields describe the direction and magnitude of the induced electric current density.

Figure 2(b1) presents a loop of the induced electric current between the top W layer and the W ground plane, which is a signature of magnetic resonance resulting from the antiparallel currents [1,4]. These current loops are also observed in other cross sections but with different distributions due to the certain pixel arrangement at each cross section. The multiple plasmonic resonances supported in the binary-pattern nanostructure are responsible for the achieved near-perfect broadband absorption. Additionally, as tungsten is treated as a non-magnetic dispersive medium in the designed metasurface absorber, the time-averaged dissipative power density reads [16], $Q_h = \epsilon_0 \omega \epsilon_m''(\omega)|\boldsymbol{E}|^2/2$, where ϵ_m'' denotes the imaginary part of the permittivity. It indicates that the absorbed electromagnetic energy is finally converted to heat dissipation due to the optical loss in tungsten.

4. PERFORMANCE PERTURBATION FROM MINOR STRUCTURAL MODIFICATION

In order to investigate the dependence of the absorption performance on the minor pixel modifications of the optimized binary-pattern nanostructure, three types of nanostructures, patterns A1, A2 and A3, are designed as shown in Figures 3(a)–3(c) in the 11 by 11 square pixel arrays with pixel width of 100 nm. The yellow pixels are the intentionally added tungsten pixels to introduce the perturbation to the originally optimized nanostructure pattern A0. In Figure 3(a) for pattern A1, 4 yellow pixels are placed at the corners of nanostructure in the clockwise direction which breaks the central mirror symmetry of pattern A0, and the SEM image is shown in Figure 3(d). The broken symmetry is expected to lead to significant influence on the absorption spectra. The measured and simulated absorption spectra of pattern A1 are plotted in Figure 3(g), showing that the three resonance wavelengths are red shifted to λ = 2.04 μm, 2.6 μm and 4 μm, respectively, and the absorption values are lower in the wavelength range from 2

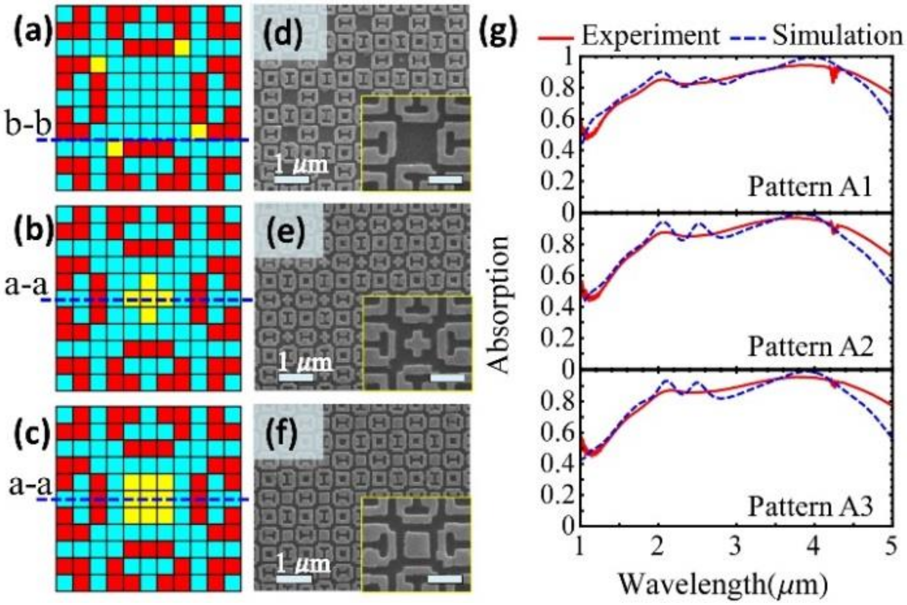

Figure 3. Designed absorber with modification. Schematic of three types of modified patterns A1, A2 and A3 with yellow pixels representing the perturbations to pattern A0 shown in (a)–(c). (d)–(f) SEM images of patterns A1, A2 and A3. Scale bar: 400 nm. (g) Measured and simulated absorption spectra under unpolarized normal incidence.

µm to 3.5 µm compared to pattern A0. Furthermore, Figures 3(b)–3(c) present the perturbed patterns A2 and A3 with the additional central cross and square structures, respectively. The corresponding absorption spectra of patterns A2 and A3 shown in Figure 3(g) exhibit similar behavior due to the same plasmonic resonance mechanism for cross and square structures with the same geometric length and thickness [17]. Compared to pattern A1, the resonances at ~ 2.5 µm for patterns A2 and A3 are observed to have blue-shifts and the absorption increases slightly at this wavelength due to the central cross/square structure. However, compared to pattern A0, the separations between the two resonances in the wavelength range of 2.5 – 4 µm become larger and lead to the absorption performance degradation from the optimized pattern A0.

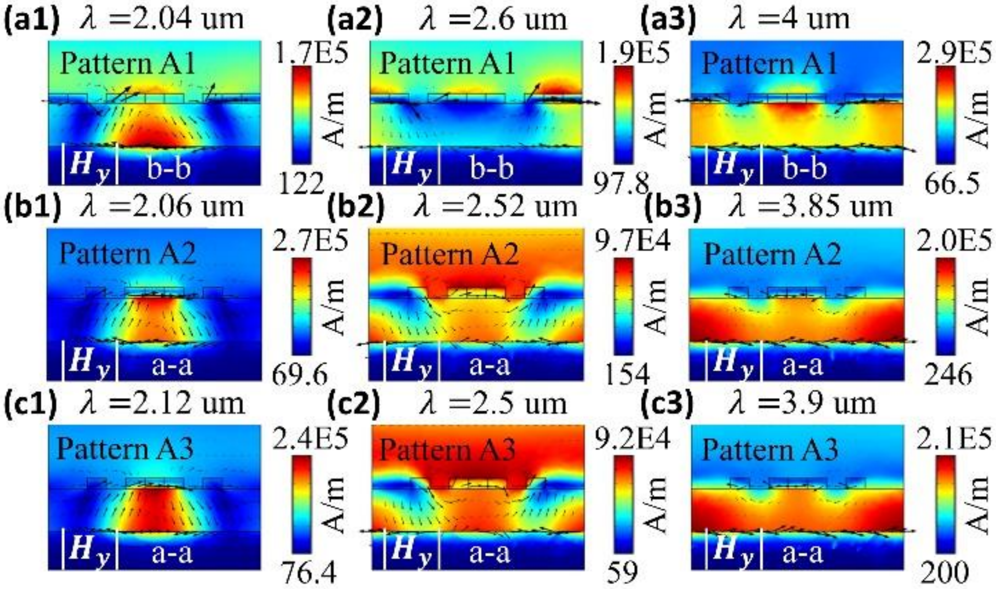

Figure 4. Mode analysis of designed absorber. Cross section view of the magnetic field $|H_y|$ distributions of (a1)–(a3) Pattern A1 at the location b-b, (b1)–(b3) Pattern A2 at the location a-a, and (c1)–(c3) Pattern A3 at the location a-a at three resonance wavelengths under TM polarization at normal incidence.

The perturbation of absorption performance can be understood with optical mode analysis for the modified nanostructures. Figure 4 shows the cross-section view of the magnetic field $|H_y|$ distributions of patterns A1, A2 and A3 at the locations marked by the dashed blue lines in Figures 3(a)–3(c). The yellow pixels in pattern A1 are expected to modify the magnetic field distributions, which are verified through simulation results in Figres 4(a1)–4(a3) at the b-b cross section. The asymmetric magnetic field distribution on the top metal layer is presented in Figure 4(a2) due to the existence of the added pixels in pattern A1, compared with the central symmetric magnetic field distribution of pattern A0 shown in Figure 2(c2). Pattern A2 and A3 keep the central mirror symmetry as pattern A0 after adding new pixels. In Figures 4(b1)-4(c3), the magnetic field $|H_y|$ distributions of patterns A2 and A3 at the a-a cross section are similar at three resonance wavelengths, so that it is almost equivalent to add either the central cross structure or the square structure into pattern A0. The observed variations of magnetic field distributions of patterns A2 and A3 compared with those of pattern A0 in Figures 2(b1)-2(b3) explain the perturbations due to the central structures, which result in the wavelength shifts for the resonances and the lower absorption in the spectra at wavelength range of 2.5 – 3.5 µm for patterns A2 and A3.

5. ALTERNATIVE DESIGN OF THE BROADBAND ABSORBER

In theory, there are multiple solutions available for the optimized binary-pattern nanostructures to achieve the broadband near-perfect absorption performance. However, it is difficult to find all the solutions due to the constraints from the optimization algorithm, practical fabrication limit and the limited computational resources [8–10,13]. Evolutionary optimization algorithm, for instance the micro-GA, will usually converge to a local minimum under predefined constraints for the target fitness value or just stop with the criteria of a maximum generation number. In this work, except pattern A0, another type of nanostructure pattern B0 is also found to satisfy the design target with constraint condition of 125 nm pixel width. Figure 5(a) shows the top view of pattern B0 in the 11 by 11 array with the pixel width of 125 nm and Figure 5(e) gives the SEM image. The measured and simulated absorption spectra are plotted in Figure 5(k), showing broadband absorption over 0.9 from 1.75 µm to 4.03 µm or over 0.95 from 2.8 µm to 3.8 µm. Three resonance peaks at the wavelength of 1.71 µm, 2.51 µm and 3.53 µm are found for pattern B0. Similar to pattern A0, broadband absorption performance of pattern B0 also results from multiple plasmonic resonances.

The perturbation of absorption performance due to the minor pixel modifications of pattern B0 is also investigated with the new nanostructures of patterns B1, B2 and B3 with single-pixel level modifications as shown in Figures 5(b)–5(d) for schematics and Figures 5(f)–5(h) for SEM images. The influence from the minor modifications is clearly seen in the absorption spectra in Figure 5(k). Compared with the absorption spectrum of pattern B0, patterns B1 and B2 exhibit red shifts for the resonance wavelengths and a slightly lower absorption in the wavelength range of 2 – 3.5 µm, while pattern B3 shows a more significant absorption degradation in the wavelength range of 1.3 – 2 µm. The observed spectra indicate that the intentionally added single-pixel defects have different levels of impact on the absorption performance according to the certain pixel locations. Furthermore, the scaling effect when designing the nanostructure is another factor to

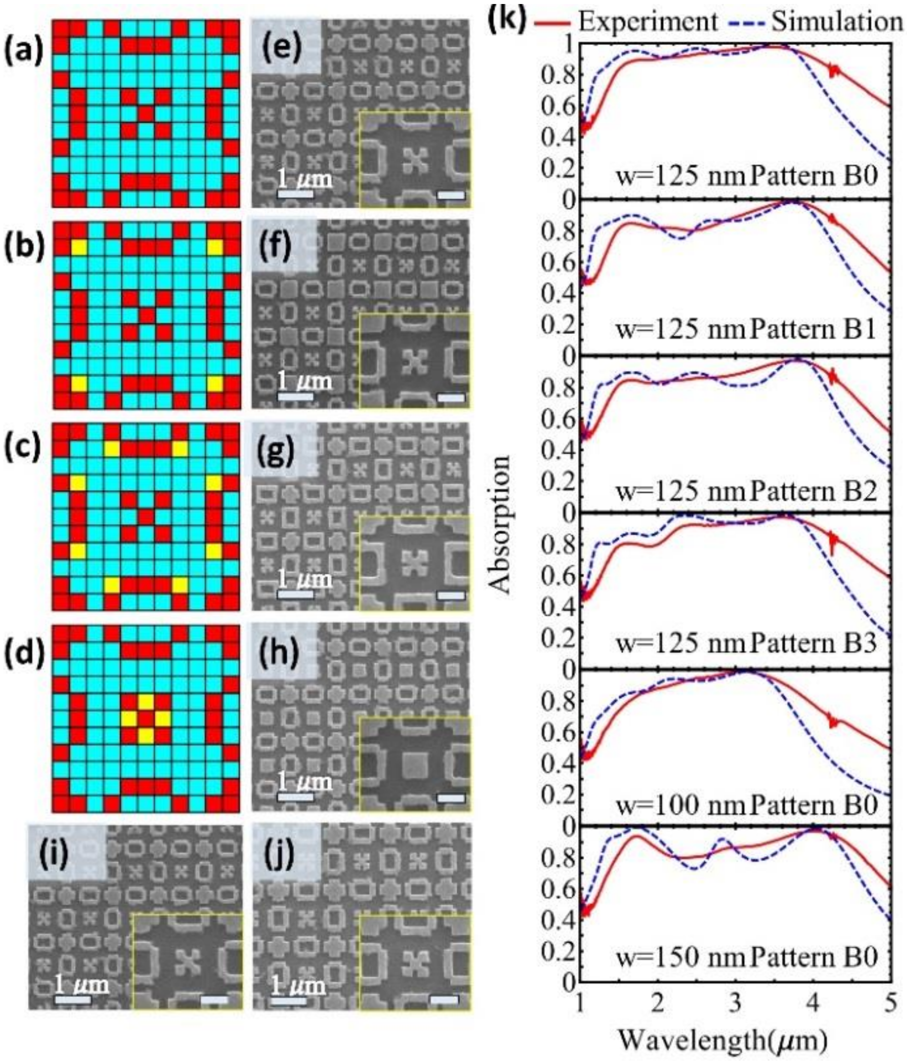

Figure 5. Designed binary-pattern absorber and modifications. Schematics of (a) Pattern B0 and three modified nanostructures (b) Pattern B1, (c) Pattern B2 and (d) Pattern B3 with the added yellow tungsten pixels. (e)–(h) SEM images of patterns B0, B1, B2 and B3. (i), (j) SEM images of the scaled nanostructures with pattern B0 but with pixel width *w* = 100 and 150 nm. Scale bar: 400 nm. (k) Measured and simulated absorption spectra under unpolarized normal incidence for the nanostructures in (e)–(j).

perturb the absorption performance. Here, the designed pattern B0 is scaled up and down through adjusting the pixel width *w* as 100 nm and 150 nm in the unit cell. The SEM images of the scaled nanostructures are shown in Figures 5(i) and 5(j) and the corresponding absorption spectra are plotted in the last two panels of Figure 5(k). With smaller pixel width of 100 nm, the absorption bandwidth shrinks and the resonance wavelengths are blue shifted (for example, a resonance shift from 3.55 μm to 3.17 μm is observed in the long wavelength region). In contrast, with the larger pixel width of 150 nm, the absorption bandwidth is broadened and the resonance wavelengths show red shifts. However the absorption from 2 – 3 μm is significantly lowered to below 0.86. In general, the absorption performance is degraded in both cases due to the modification of the optimized nanostructure with the pixel width of 125 nm.

6. CONCLUSION

In summary, we present the micro-GA enabled design method for the W-based broadband mid-infrared binary-pattern metasurface absorbers. Two kinds of optimized nanostructures are found with excellent absorption performance. The broadband absorption properties are contributed from the multiple plasmonic resonances supported in the unit cell. Furthermore, absorption perturbations due to the minor modifications of the optimized nanostructures by adding extra tungsten pixels are discussed. This work provides an efficient approach to design and optimize complex metamaterial and metasurface nanostructures for high-performance functional optical devices.

ACKNOWLEDGEMENTS

The authors thank the support from ISC and MRC centers at Missouri S&T. This work was performed, in part, at the Center for Nanoscale Materials, a U.S. Department of

Energy Office of Science User Facility, and supported by the U.S. Department of Energy, Office of Science, under Contract No. DE-AC02-06CH11357.

REFERENCES

[1] N. I. Landy, S. Sajuyigbe, J. J. Mock, D. R. Smith, and W. J. Padilla, "Perfect Metamaterial Absorber," Phys. Rev. Lett. 100, pp. 1–4, 2008 .

[2] C. M. Watts, X. Liu, and W. J. Padilla, "Metamaterial Electromagnetic Wave Absorbers," Adv. Mater. 24, pp. OP98-120, OP181, 2012 .

[3] H. Deng, Z. Li, L. Stan, D. Rosenmann, and D. Czaplewski, "Broadband Perfect Absorber Based on One Ultrathin Layer of Refractory Metal," Opt. Lett. 40, pp. 2592–2595, 2015 .

[4] H. Wang and L. Wang, "Perfect Selective Metamaterial Solar Absorbers," Opt. Express 21, pp. A1078–A1093, 2013 .

[5] Y. Cui, K. H. Fung, J. Xu, H. Ma, Y. Jin, S. He, and N. X. Fang, "Ultrabroadband Light Absorption by a Sawtooth Anisotropic Metamaterial Slab," Nano Lett. 12, pp. 1443–1447, 2012 .

[6] M. Desouky, A. M. Mahmoud, and M. A. Swillam, "Silicon Based Mid-IR Super Absorber Using Hyperbolic Metamaterial," Sci. Rep. 8, 2018 .

[7] B. Vial and Y. Hao, "Topology Optimized All-Dielectric Cloak: Design, Performances and Modal Picture of the Invisibility Effect," Opt. Express 23, pp. 23551, 2015 .

[8] S. Chakravarty, R. Mittra, and N. R. Williams, "Application of a Microgenetic Algorithm (MGA)to the Design of Broad-Band Microwave Absorbers Using Multiple Frequency Selective Surface Screens Buried in Dielectrics," IEEE Trans. Antennas Propag. 50, pp. 284–296, 2002 .

[9] J. a Bossard, S. Yun, D. H. Werner, and T. S. Mayer, "Synthesizing Low Loss Negative Index Metamaterial Stacks for the Mid-Infrared Using Genetic Algorithms.," Opt. Express 17, pp. 14771–9, 2009 .

[10] J. A. Bossard, L. Lin, S. Yun, L. Liu, D. H. Werner, and T. S. Mayer, "Near-Ideal Optical Metamaterial Absorbers with Super-Octave Bandwidth," ACS Nano 8, pp. 1517–1524, 2014 .

[11] S. Roy, S. D. Roy, J. Tewary, A. Mahanti, and G. K. Mahanti, "Particle Swarm Optimization for Optimal Design of Broadband Multilayer Microwave Absorber for Wide Angle of Incidence," Prog. Electromagn. Res. B 62, pp. 121–135, 2015 .

[12] S. Yu, C. Wang, Y. Zhang, B. Dong, Z. Jiang, X. Chen, W. Chen, and C. Sun, "Design of Non-Deterministic Quasi-Random Nanophotonic Structures Using Fourier Space Representations," Sci. Rep. 2017 .

[13] S. Jafar-Zanjani, S. Inampudi, and H. Mosallaei, "Adaptive Genetic Algorithm for Optical Metasurfaces Design," Sci. Rep. 8, pp. 11040, 2018 .

[14] A. D. Rakić, A. B. Djurišić, J. M. Elazar, and M. L. Majewski, "Optical Properties of Metallic Films for Vertical-Cavity Optoelectronic Devices," Appl. Opt. 37, pp. 5271, 1998 .

[15] J. Kischkat, S. Peters, B. Gruska, M. Semtsiv, M. Chashnikova, M. Klinkmüller, O. Fedosenko, S. Machulik, A. Aleksandrova, G. Monastyrskyi, Y. Flores, and W. Ted Masselink, "Mid-Infrared Optical Properties of Thin Films of Aluminum Oxide, Titanium Dioxide, Silicon Dioxide, Aluminum Nitride, and Silicon Nitride," Appl. Opt. 51, pp. 6789, 2012 .

[16] J. Hao, L. Zhou, and M. Qiu, "Nearly Total Absorption of Light and Heat Generation by Plasmonic Metamaterials," Phys. Rev. B 83, pp. 165107, 2011 .

[17] A. Sakurai, B. Zhao, and Z. M. Zhang, "Resonant Frequency and Bandwidth of Metamaterial Emitters and Absorbers Predicted by an RLC Circuit Model," J. Quant. Spectrosc. Radiat. Transf. 149, pp. 33–40, 2014 .

V. STRONG CIRCULAR DICHROISM IN PLASMONIC METASURFACES OPTIMIZED BY MICRO GENETIC ALGORITHM

Zhigang Li,[1] Liliana Stan,[2] David A. Czaplewski,[2] Xiaodong Yang,[1] and Jie Gao [1,*]

[1]Department of Mechanical and Aerospace Engineering, Missouri University of Science and Technology, Rolla, MO 65409, USA

[2]Center for Nanoscale Materials, Argonne National Laboratory, Argonne, IL 60439, USA

ABSTRACT

Strong circular dichroism in absorption in near-infrared range is realized by plasmonic metasurfaces via the micro genetic algorithm optimization method. Two types of binary chiral metasurfaces are designed and experimentally realized with excellent chirality performance. The investigations on the effect of geometric parameters influencing circular dichroism are also conducted for the binary-patterned chiral metasurfaces. The strong circular dichroism in absorption is attributed to simultaneous excitation and interference of modes arising from x- and y-polarized light with different phase shift. This work provides a universal design method toward the on-demand properties of the chiral metamaterials, which paves the way for future applications in chemical and biological chiral sensing, chiral imaging and nonlinear optics.

1. INTRODUCTION

Chiral structures are well known for lacking any mirror symmetry. Different from chiral molecules or materials with the weak chirality in nature, artificially designed chiral metamaterials, for instance, 2D anisotropic chiral metamaterials [1–4], dual-layer or multilayered twisted structures [5–7], 3D helical meta-atoms [8,9], and even achiral planar metasurfaces [10,11] can achieve giant chiral properties including optical rotation, circular dichroism and asymmetric transmission. Optical chirality has attracted intensive attentions in chemical and biological sensing [7], high contrast imaging for display technology [12] as well as electrooptical signal manipulation [3]. Generally, 2D planar metasurfaces with strong chirality are more appealing for applications with the need of compact configuration and simple fabrication requirement. However, there are two limits in the metamaterials design progress, complexity and efficiency. For the traditional design method mainly depending on the manual parameters sweeping, only few design variables and limited complexity can be involved in the geometry, possibly missing the optimal solution. As for efficiency, manually conducted metamaterial design method is usually limited to specific design applications, which is not efficient serving as the universal design method.

The two limits can be solved by the optimization methods, such as evolutionary method [13–15], gradient descent method [16,17], particle swarm optimization [18,19], and learning method based on neural networks [20,21]. Among various optimization methods, genetic algorithm, one popular branch of the evolutionary method for its simple frame and flexible compatibility, has successfully demonstrated the robustness and efficiency in the optimization of the electromagnetic design, such as the design with broadband absorber under linear polarization [14,15,22,23], selective transmission under circular polarization [24,25] or broadband circular polarizer [26]. However, the mechanism of generating the strong circular dichroism with complex binary-pattern has not been thoroughly studied yet. Moreover, compared with traditional genetic algorithm, micro genetic algorithm is more feasible in real applications since it accelerates the evolution progress by the repopulation step and consequently requires smaller initial population group but with faster convergence [27,28].

In this work, we employ the micro genetic algorithm to optimize the chiral metasurface for a strong circular dichroism in the absorption (CDA), which is the differential absorption of left-handed circularly polarized (LCP) and right-handed circularly polarized (RCP) light. Two types of nanostructure patterns are obtained with strong circular dichroism at the wavelength of 1.62 μm and 1.91 μm, respectively. The influence of geometric parameters on circular dichroism is studied by involving single pixel changes in the chiral metasurface pattern. Simultaneous excitation and interference of multiple modes under different circular polarizations is found to be responsible for the strong CDA. The energy dissipation within the metasurfaces is further discussed. The proposed design method is promising to realize the on-demand design of chiral structures with high circular dichroism, and the chiral metasurfaces are very attractive for the applications in sensing, imaging and optoelectronics.

2. FORMULATION OF STRUCTURAL DESIGN WITH MICRO GENETIC ALGORITHM

According to the principle of micro genetic algorithm, optimization of the chiral metasurface initializes with random geometry in the top pattern layer of the metamaterial. The geometric information of structure is encoded into the chromosome, which is composed of binary numbers. In the discretized binary space, the binary numbers “one”s and "zero"s represent material and free space, respectively. The nanostructure pattern evolves toward the optimal pattern along the direction driven by the cost function, which evaluates the discrepancy between the CDA value of each generated nanostructure and the predefined target value. Let the cost function cast as $F = \sum_{\lambda}(1 - |A_{LCP} - A_{RCP}|)^2$, where A_{LCP} and A_{RCP} are the absorption of the nanostructure under the LCP and RCP incidence, respectively. Thus, $CDA = A_{LCP} - A_{RCP}$. The evolutionary optimization problem can be mathematically written as: minimize F, subject to $\nabla \times \nabla \times \boldsymbol{E} - \mu\omega^2\epsilon\boldsymbol{E} = 0$ and $\nabla \cdot \epsilon\boldsymbol{E} = 0$, where $\boldsymbol{E}$ denotes the electric field, ϵ the permittivity and μ the permeability. The formulated problem is then solved through the finite element method and cost value F is derived from the absorption spectra for each generated metasurface. Based on the value of F, the evolution loop will choose to update the chromosome information for new calculation or stop the loop until the predefined target is satisfied in the program.

In this work, the target performance is expected to present the high chirality over 0.5 in CDA for the designed metasurface under LCP and RCP incidence over a certain short wavelength range. To speed up the calculation in the optimization problem, we selected 10 equally spaced test wavelengths in the wavelength range between 1.5 μm to 1.75 μm (or between 1.75 μm to 2 μm). For increasing the anisotropic properties and further reducing the complexity in the calculation, the metasurface employs a non-square 15×11 array in the binary pattern with 2-fold rotation symmetry and intentionally defined gap space between four quadrants. The evolutional optimization is implemented by the micro genetic algorithm with a population of 20 chromosomes and the tournament selection for crossover for each generation. When achieving the valve value of the similarity among chromosomes, the algorithm takes the repopulation step to increase diversity and speed up the evolution without the need of mutation step. Eventually, with the convergence within 35 generations, this work obtains two types of chiral metasurface patterns with excellent CDA values satisfying the predefined target.

3. DESIGNED METAMATERIAL STRUCTURES WITH STRONG CIRCULAR DICHROISM

Metal-dielectric-metal (MDM) structure is used in our design by taking its advantage of the flexible design ability for the top metallic layer, which can be further enhanced by the geometry generating feature in the micro genetic optimization algorithm. Figure 1(a) presents the schematic of the designed metamaterial with chiral metasurface with strong circular dichroism. The designed metamaterial consists of a 55 nm-thick top gold (Au) layer with the Pattern A obtained from the optimization algorithm, a 145 nm-thick silica (SiO_2) spacer layer and a 200 nm-thick Au substrate. As the substrate is optically thick enough to eliminate the transmission through the designed nanostructure, the absorption is calculated as unity minus the reflection upon the incidence under LCP or RCP state. In Figure 1(b), it shows the top view of the designed chiral metasurface Pattern A with a 15×11 array composed of gold pixels with side $w = 64$ nm. The supercell Pattern A includes two types of components with 2-fold symmetry in general. Additionally, the material parameters in the simulation are taken from references for Au [29] and SiO_2 [30], respectively.

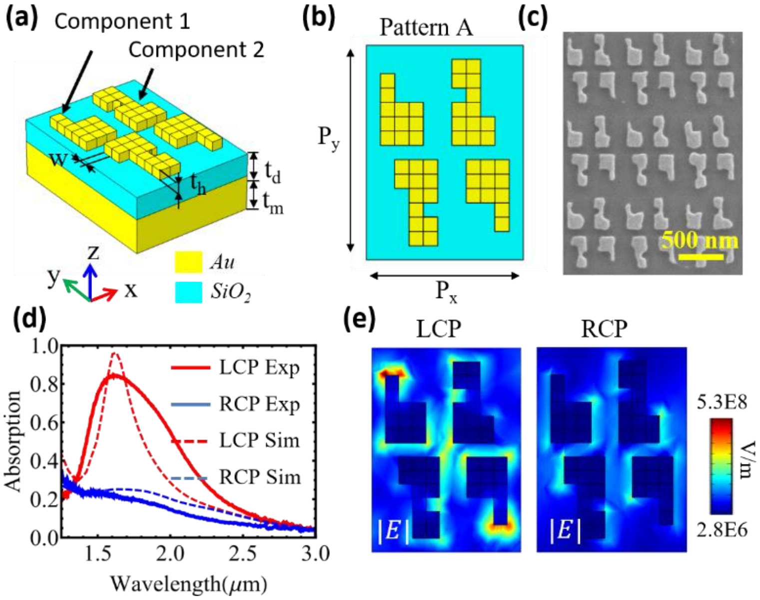

Figure 1. Designed chiral metasurface with strong chiral dichroism both in simulation and experiment. (a) Schematic of the designed chiral metasurface composed of top Au pattern layer (pattern A), SiO_2 spacer layer and Au substrate. The geometric parameters are denoted as w = 64 nm, t_h = 55 nm, t_d = 145 nm and t_m = 200 nm. (b) Top view of the designed pattern A with the period P_x = 704 nm and P_y = 960 nm. (c) SEM image of the fabricated nanostructure pattern A. (d) Experimental and simulated absorption spectra under LCP and RCP incidence at normal direction, respectively. (e) Normalized electric field distributions at the resonant wavelength 1.62 μm under LCP and RCP incidence, respectively, plotted at the surface of the top Au pattern.

To realize the designed chiral metasurface in the experiment, the gold and silica layers are deposited on the silicon wafer by using the magnetic sputtering and electron-beam evaporation, respectively. The nanostructure pattern array is milled on the top metallic layer of the Au-SiO_2-Au thin film through the focused ion beam (FIB) system (FEI Helios Nanolab 600, 30 kV, 9.7 pA). Scanning electron microscopy (SEM) image of the fabricated nanostructure Pattern A is shown in Figure 1(c), in which a slight variation in the geometric parameters can be observed compared with the designed structure. The geometric variations are attributed to the fabrication limitation of the FIB technique.

Furthermore, the fabricated nanostructure is characterized through the optical spectra response with the fourier transform infrared spectroscopy (FTIR, Nicolet 6700).

Figure 1(d) shows the measured and simulated absorption spectra (A_{LCP}, A_{RCP}) of the chiral metasurface under the LCP and RCP incidence at the normal direction, respectively. The simulated absorption spectra present strong circular dichroism where the Pattern A possesses a near perfect absorption (0.96) under the LCP incidence at the resonant wavelength of 1.62 µm and low absorption at its counterpart incidence. The chiral metasurface Pattern A exhibits a high CDA value of 0.71 at 1.62 µm while it turns out to be 0.63 in the experiment. The discrepancy between the prediction and the experiment mainly arises from the geometric variations in the fabrication, as well as the imperfect linear polarizer and quarter-wave plate used to generate the circular polarized wave. Figure 1(e) observes the localization of the electric field distribution $|E|$ and high contrast of the electric field intensity under the LCP and RCP excitations at the wavelength of 1.62 µm. Giant CDA is induced by the dichroic modes excited in the nanostructure under circular polarized wave. A detailed discussion is given in part 5.

Taking advantage of the flexibility in the optimization method with the micro genetic algorithm, this work determines to present one alternative chiral metasurface. The same geometric parameters and materials are employed in the optimization progress but with the target only different in the operating wavelength range. The new objective is to achieve the CDA value over 0.5 between 1.75 µm to 2 µm. Figures 2(a)-2(b) show the metamaterial nanostructure obtained from the optimization result. The supercell pattern B is also composed of two types of components with the 2-fold symmetry. A SEM image of the fabricated pattern B array is shown in Figure 2(c). The high chirality in the absorption spectra can be found in Figure 2(d), which presents the measured and simulated absorption spectra under the LCP and RCP incidence, respectively. For the LCP incident wave, the chiral metasurface generates a strong absorption around 0.94 at the resonant wavelength of 1.91 μm, which leads to the CDA value of 0.67 and 0.6 in simulation and experiment, respectively. As shown in Figure 2(e), upon the incidence of LCP wave, strong circular dichroic modes are excited between the gap of the four components in the chiral metasurface Pattern B, however, these modes are suppressed under the RCP incidence.

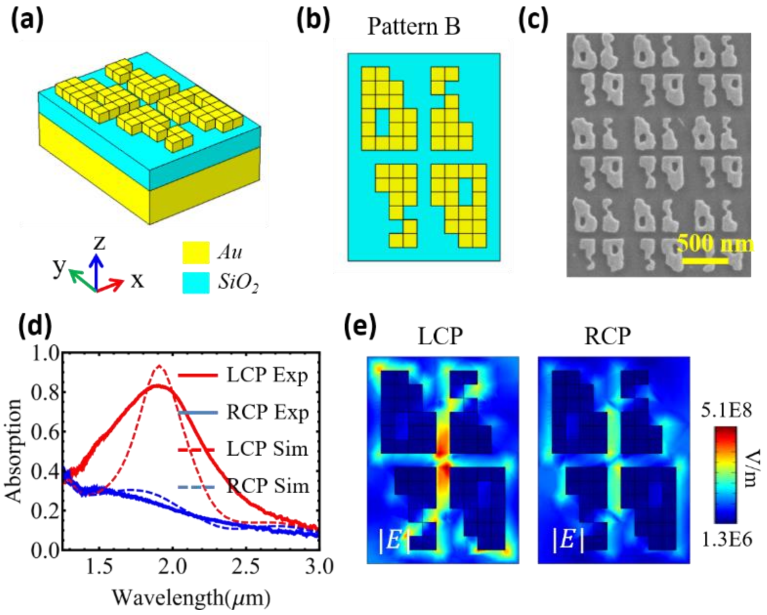

Figure 2. Alternatively designed chiral metasurface with strong circular dichroism both in simulation and experiment. (a) Schematic of the designed chiral metasurface with the same physical dimensions as in Figure 1(a). (b) Top view of the designed chiral metasurface pattern B. (c) SEM image of the fabricated chiral metasurface pattern B. (d) Experimental and simulated absorption spectra under LCP and RCP incidence at normal direction, respectively. (e) Normalized electric field distributions$|E|$ at the resonant wavelength 1.91 μm under LCP and RCP incidence, respectively, plotted at the surface of the top Au pattern.

4. INFLUENCE OF GEOMETRIC PARAMETERS INFLUENCING CIRCULAR DICHROISM

Geometric parameters of the designed metasurface is studied to investigate the robustness of the chiral performance and sensitivities on the geometric variations possibly caused by the fabrication progress. Taking the chiral metasurface Pattern A for an example, in Figures 3(a) and 3(b), we study the influence of increasing and decreasing the gap distance by one-pixel distance in x direction by shifting two components shown in the dashed blue box, respectively. As shown in Figure 3(d), the resonance peak in the absorption spectrum exhibits redshift to 1.67 μm with perfect LCP absorption and CDA of 0.74 under the LCP incidence for chiral metasurface Pattern A1. The excellent absorption performance arises from the increased confinement of the resonant modes due to decreased gap distance between the neighboring components. In contrast, Figure 3(e) shows slight blueshift to 1.61 μm with LCP absorption of 0.9 and CDA of 0.62 for the resonant wavelength because of the decreased confinement of the resonant modes as the increasing gap distance. Moreover, Figure 3(c) conducts the geometric alignment in plane with left shifting lower two components shown in the dashed blue box by one-pixel distance. Results of this alinement operation are plotted in Figure 3(f) showing blueshift to 1.6 μm with LCP absorption of 0.95 and CDA of 0.7, which indicates the modification of modes coupling resulted from the shift operation of components.

To reveal the influence of critical geometric features on the performance of the chirality, this work examines the cases of extending or shortening the lengths and widths of the supercell components by adding or removing pixels in the designed chiral metasurface patterns. Figure 3(g) adds one pixel (in the red dashed circle) to the component 1 of chiral metasurface pattern A, leading to obvious redshift to 1.86 μm with CDA of 0.34 shown in Figure 3(j). The degradation in the performance is attributed to the weaker modes coupling of component 1 resulted from the added pixel, which is discussed in detail in part 5. In comparison, one pixel is removed for the component 1 as shown in Figure 3(h), resulting in the blueshift of the LCP resonant peak to 1.42 μm with CDA of 0.45. Similarly, in Figure 3(i), this work also studies the pixel addition effect on component 2 of the nanostructure. The LCP absorption peak is shifted to 1.54 μm with CDA of 0.55. Consequently, geometric modification through adding or removing important geometric features can significantly degrade the circular dichroism of the

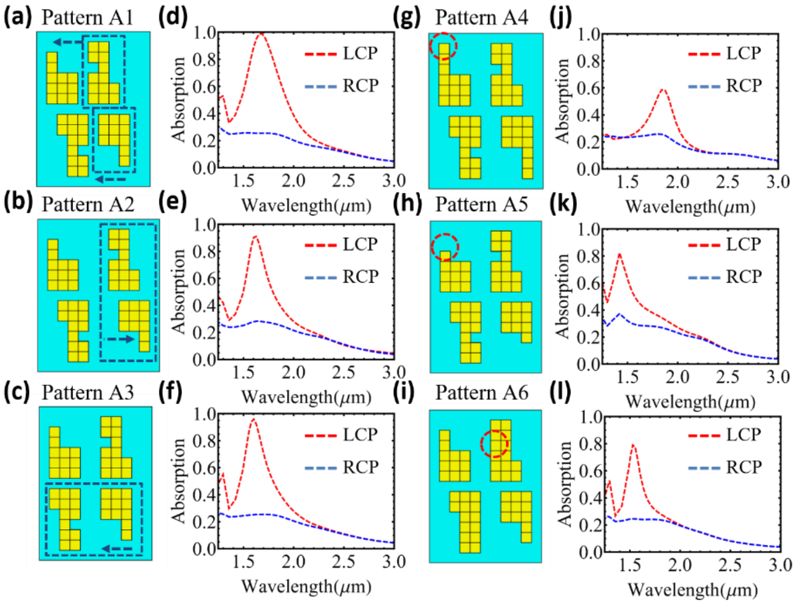

Figure 3. Investigation of influence on the chirality due to geometric variations. Schematic of (a) decreasing (b) increasing the gap distance in x direction and (c) geometric alinement by shifting two components shown in the dashed blue box. (d)–(f) show the absorption spectra under LCP and RCP incidence corresponding to the chiral metasurface pattern in (a)–(c). Schematic of geometric shape modification shown in red circle in (g)–(i) and the corresponding absorption spectra under LCP and RCP incidence.

designed nanostructure pattern compared with the relatively less influence from the shift or alignment of internal components. The geometric variations also explain the broaden peak and mismatch phenomena between the simulation and experiment results shown in Figure 1(d) and Figure 2(d).

5. CIRCULAR DICHROIC MODE ANALYSIS OF THE DESIGNED METAMATERIALS

To find the mechanism how the strong circular dichroism is generated, we conduct a further analysis on the circular dichroic mode distributions inside the designed chiral metasurface. Based on the chiral metasurface Pattern A, Figure 4(b) plots the absorption spectra under x and y polarized incidence at normal direction, respectively. Resonant peak is observed at the wavelength of 1.58 μm and 1.6 μm for x and y polarized absorption, respectively, which are close to the LCP resonant wavelength (1.62 μm). The electric field E_x distributions are presented in Figure 4(c) for the x-polarized incidence with a phase shift of −90° or 90° plotted at the wavelength of 1.62 μm, as well as the y-polarized incidence without phase shift. One can find that the two antiparallel diploe modes form one quadruple mode on each component within the supercell Pattern A. Moreover, when the metasurface is excited with circularly polarized light, the two plasmonic modes under x-polarized and y-polarized incidence are simultaneously excited with a relative phase delay of 90° or −90° and interfere with each other to generate the orthogonal RCP and LCP modes. As seen in the right panel of Figure 4(c), for LCP mode, two typical areas where the presented modes stem from the constructive interference of x-polarized and y-polarized modes are shown in red and blue dashed boxes; however, destructive interference is found for the RCP mode. Thus, electric field is highly enhanced under LCP excitation and extremely weak (mode intensity is around five times smaller) with the RCP excitation, resulting into the strong circular dichroism.

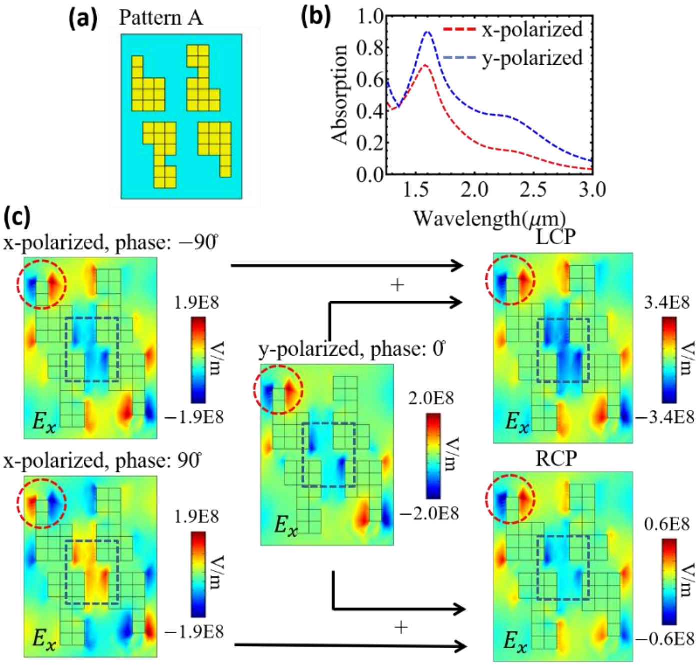

Figure 4. Circular dichroic modes analysis for the designed chiral metasurface pattern A. (a) Schematic of the top view of chiral metasurface pattern A. (b) Absorption spectrum under x and y polarized incidence at normal direction, respectively. (c) Conceptual schematic of the arising of circular dichroic modes. It shows the electric field distribution E_x under x-polarized incidence with phase shift of −90° or 90°, as well as E_x under y-polarized incidence without phase shift, resulting into the circular dichroic mode under LCP and RCP incidence, respectively. All modes are plotted at the surface of the top Au pattern at the wavelength of 1.62 μm.

With the purpose to understand performance degradation in chirality, circular dichroic mode analysis is also implemented for representative chiral metasurface Pattern A4. Different from Pattern A, Pattern A4 shows degraded CDA due to the geometric parameters' variation in extending the length of two components within the supercell by adding pixels. Figure 5(b) plots the absorption spectra under the linear polarization at x and y direction, respectively. Pattern A4 exhibits a lower absorption at the wavelength of 1.83 µm and 1.8 µm for x and y polarized incidence, respectively. Also, the x-polarized resonant absorption is stronger than y-polarized counterpart, rather than the inversed case as shown in the results of Pattern A (Figure 4(b)). In Figure 5(c), the electric field E_x distributions are shown for the x- and y-polarized incidence with different phase shifts at the wavelength of 1.86 µm, respectively. In comparison with Pattern A, the extended

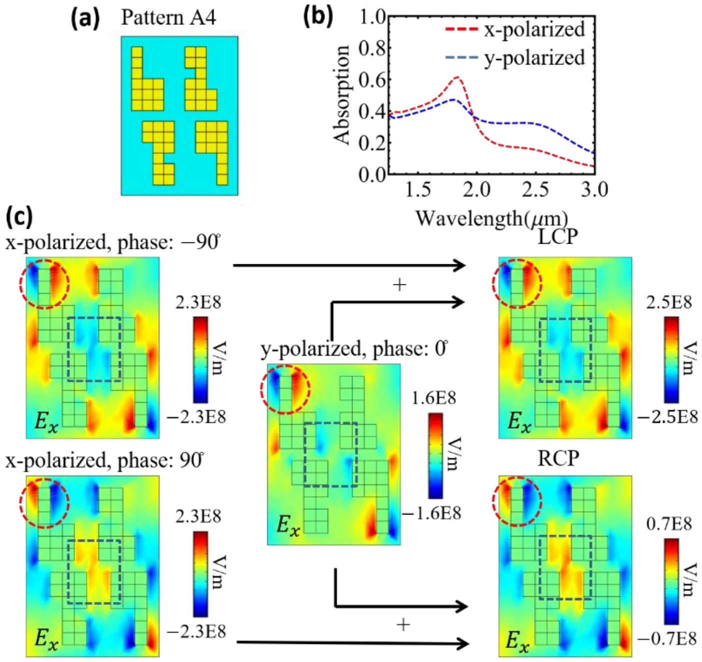

Figure 5. Circular dichroic modes analysis for the designed chiral metasurface pattern A4. (a) Schematic of the top view of chiral metasurface pattern A4. (b) Absorption spectrum under x and y polarized incidence at normal direction, respectively. (c) Conceptual schematic of the arising of circular dichroic modes. It shows the electric field distribution E_x under x-polarized incidence with phase shift of −90° or 90°, as well as E_x under y-polarized incidence without phase shift, resulting into the circular dichroic mode under LCP and RCP incidence, respectively. All modes are plotted at the surface of the top Au pattern at the wavelength of 1.86 µm.

length of supercell components from added pixels in Patten A4 causes the different field distribution and mode coupling, and hence a higher mode intensity under x-polarized incidence rather than y-polarized incidence. Similarly, when LCP light is illuminated, the LCP or RCP mode is generated based on the simultaneously excited and interfered x- and y-polarized light depending whether they are in phase or out of phase. However, for LCP incidence, due to the adverse influence brought by the geometric parameters variations, the electric field enhancement stemmed from the constructive interference is weakened compared with that of Pattern A. The resulted electric field intensity of the LCP mode exhibits only 3.5 times of that of the RCP excitation, generating a relatively degraded performance of the circular dichroism. Therefore, the chiral performance of the designed metasurface composed of binary pattern can be sensitive on the variations of critical geometric parameters.

For a full understanding the wave propagation and energy absorption inside the designed metasurfaces, we perform the investigation on the magnetic field distributions at certain cross sections of the Pattern A, located at red dashed line a-a and b-b in the x-z plane, respectively (Figure 6(a)). Figure 6(b) shows the cross-sectional magnetic field distribution H_y at position a-a at the wavelength of 1.62 μm. Magnetic dipoles are observed around the metallic material but showing a different modes distribution under LCP and RCP excitations. The magnetic field also induces stronger circulating currents represented by the black arrows between two components under the LCP excitation than those of the RCP excitation. Similarly, a more complex magnetic modes distribution can be found at position b-b shown in Figure 6(c), where the coupling between the two components is obvious as the middle gap is shorter for circulating current. When comparing the magnetic field intensity at two cross section locations, a stronger mode excitation and hence more contribution to the absorption can be found for cross section at position a-a. Furthermore, Figure 6(d) plots the time-averaged optical power dissipation

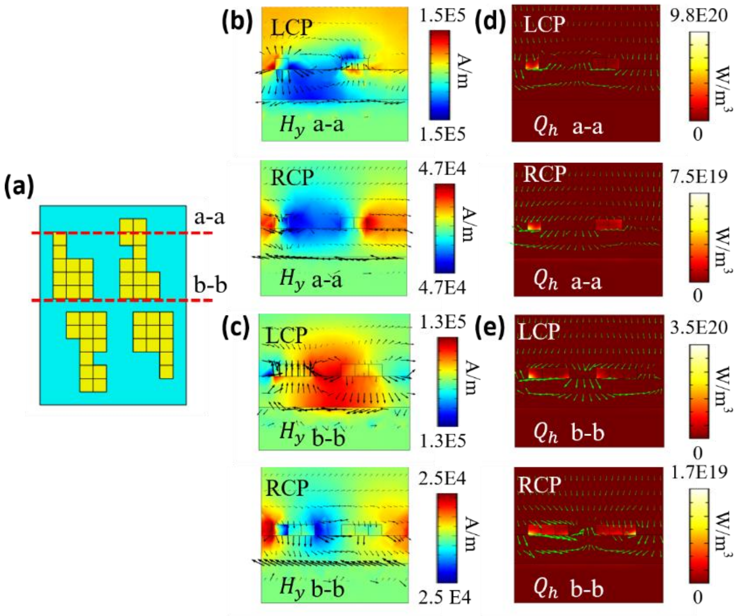

Figure 6. Mode analysis at side cross sections. Schematic of cross-section positions at a-a and b-b shown in (a). Cross-sectional magnetic field H_y distributions under LCP or RCP incidence located at position (b) a-a and (c) b-b in the x-z plane, respectively. The black arrows represent the direction and magnitude of the induced current density due to the magnetic field. Cross-sectional time-averaged optical power dissipation density Q_h distributions under LCP or RCP incidence located at position (d) a-a and (e) b-b, respectively. Green arrows describe the direction and magnitude of Poynting vector. All fields are plotted at the wavelength of 1.62 μm.

density Q_h distributions under LCP or RCP incidence located at position a-a at the wavelength of 1.62 μm. Q_h is calculated with the formula [31], $Q_\mathrm{h} = \epsilon_0 \omega \epsilon_m''(\omega)|\boldsymbol{E}|^2/2$, where ϵ_0 and ϵ_m'' denote the permittivity in vacuum and imaginary part of the permittivity of metal. The circularly polarized light flows into the nanostructure in the way depicted through the direction and magnitude of the Poynting vector (green arrows). Due to the stronger circular dichroic mode interactions, LCP excitation leads to a higher energy dissipation density compared with the RCP excitation. Similar energy dissipation phenomena can be observed in Figure 6(e) for cross-sectional position at b-b, however, the maximum dissipation density value under either LCP or RCP excitation is lower compared with that at location a-a due to the special modes distribution across the components.

6. CONCLUSION

In this work, plasmonic metasurface nanostructure is designed to realize strong circular dichroism in the absorption at near-infrared range by using the micro genetic algorithm optimization method. Two binary-patterned chiral metasurfaces obtained through the optimization method are demonstrated in the experiment with CDA value of 0.63 and 0.6, respectively. Chirality of the designed metasurfaces remains robust when the gap between the supercell components changes but is sensitive to the lengths and widths of the components with single pixel change. The presented strong CDA is explained as the excitation and suppression of multiple modes under different circular polarizations. The absorption of the incident light is further discussed through the energy dissipation density distributions. This work provides an effective method to realize the on-demand design of chiral structures with excellent performance, especially strong circular dichroism, which is promising in chemical and biological chiral sensing, chiral imaging and nonlinear optics.

ACKNOWLEDGEMENTS

The authors thank the support from ISC and MRC centers at Missouri S&T. This work was performed, in part, at the Center for Nanoscale Materials, a U.S. Department of Energy Office of Science User Facility, and supported by the U.S. Department of Energy, Office of Science, under Contract No. DE-AC02-06CH11357.

REFERENCES

[1] V. A. Fedotov, P. L. Mladyonov, S. L. Prosvirnin, A. V. Rogacheva, Y. Chen, and N. I. Zheludev, "Asymmetric Propagation of Electromagnetic Waves through a Planar Chiral Structure," Phys. Rev. Lett. 97, pp. 167401, 2006.

[2] W. Li, Z. J. Coppens, L. V. Besteiro, W. Wang, A. O. Govorov, and J. Valentine, "Circularly Polarized Light Detection with Hot Electrons in Chiral Plasmonic Metamaterials," Nat. Commun. 6, pp. 8379, 2015.

[3] L. Kang, S. Lan, Y. Cui, S. P. Rodrigues, Y. Liu, D. H. Werner, and W. Cai, "An Active Metamaterial Platform for Chiral Responsive Optoelectronics," Adv. Mater. 27, pp. 4377–4383, 2015.

[4] J. Hu, X. Zhao, Y. Lin, A. Zhu, X. Zhu, P. Guo, B. Cao, and C. Wang, "All-Dielectric Metasurface Circular Dichroism Waveplate," Sci. Rep. 7, pp. 41893, 2017.

[5] N. Liu and H. Giessen, "Three-Dimensional Optical Metamaterials as Model Systems for Longitudinal and Transverse Magnetic Coupling," Opt. Express 16, pp. 21233, 2008.

[6] Y. Cui, L. Kang, S. Lan, S. Rodrigues, and W. Cai, "Giant Chiral Optical Response from a Twisted-Arc Metamaterial," Nano Lett. 14, pp. 1021–1025, 2014.

[7] Y. Zhao, A. N. Askarpour, L. Sun, J. Shi, X. Li, and A. Alù, "Chirality Detection of Enantiomers Using Twisted Optical Metamaterials," Nat. Commun. 8, pp. 14180, 2017.

[8] J. K. Gansel, M. Thiel, M. S. Rill, M. Decker, K. Bade, V. Saile, G. Von Freymann, S. Linden, and M. Wegener, "Gold Helix Photonic Metamaterial as Broadband Circular Polarizer," Science. 325, pp. 1513–1515, 2009.

[9] M. Esposito, V. Tasco, F. Todisco, M. Cuscunà, A. Benedetti, D. Sanvitto, and A. Passaseo, "Triple-Helical Nanowires by Tomographic Rotatory Growth for Chiral Photonics," Nat. Commun. 6, pp. 6484, 2015.

[10] E. Plum, X. X. Liu, V. A. Fedotov, Y. Chen, D. P. Tsai, and N. I. Zheludev, "Metamaterials: Optical Activity without Chirality," Phys. Rev. Lett. 102, pp. 113902, 2009.

[11] E. Plum, V. A. Fedotov, and N. I. Zheludev, "Specular Optical Activity of Achiral Metasurfaces," Appl. Phys. Lett. 108, pp. 141905, 2016.

[12] Y. Chen, J. Gao, and X. Yang, "Direction-Controlled Bifunctional Metasurface Polarizers," Laser Photonics Rev. 12, pp. 1800198, 2018.

[13] A. Hoorfar, "Evolutionary Programming in Electromagnetic Optimization: A Review," IEEE Trans. Antennas Propag. 55, pp. 523–537, 2007.

[14] J. A. Bossard, L. Lin, S. Yun, L. Liu, D. H. Werner, and T. S. Mayer, "Near-Ideal Optical Metamaterial Absorbers with Super-Octave Bandwidth," ACS Nano 8, pp. 1517–1524, 2014.

[15] S. Jafar-Zanjani, S. Inampudi, and H. Mosallaei, "Adaptive Genetic Algorithm for Optical Metasurfaces Design," Sci. Rep. 8, pp. 11040, 2018.

[16] C. Y. Kao, S. Osher, and E. Yablonovitch, "Maximizing Band Gaps in Two-Dimensional Photonic Crystals by Using Level Set Methods," Appl. Phys. B Lasers Opt. 81, pp. 235–244, 2005.

[17] B. Vial and Y. Hao, "Topology Optimized All-Dielectric Cloak: Design, Performances and Modal Picture of the Invisibility Effect," Opt. Express 23, pp. 23551, 2015.

[18] S. K. Goudos and J. N. Sahalos, "Microwave Absorber Optimal Design Using Multi-Objective Particle Swarm Optimization," Microw. Opt. Technol. Lett. 48, pp. 1553–1558, 2006.

[19] S. Roy, S. D. Roy, J. Tewary, A. Mahanti, and G. K. Mahanti, "Particle Swarm Optimization for Optimal Design of Broadband Multilayer Microwave Absorber for Wide Angle of Incidence," Prog. Electromagn. Res. B 62, pp. 121–135, 2015.

[20] W. Ma, F. Cheng, and Y. Liu, "Deep-Learning-Enabled On-Demand Design of Chiral Metamaterials," ACS Nano 12, pp. 6326–6334, 2018.

[21] D. Liu, Y. Tan, E. Khoram, and Z. Yu, "Training Deep Neural Networks for the Inverse Design of Nanophotonic Structures," ACS Photonics 5, pp. 1365–1369, 2018.

[22] J. a Bossard, S. Yun, D. H. Werner, and T. S. Mayer, "Synthesizing Low Loss Negative Index Metamaterial Stacks for the Mid-Infrared Using Genetic Algorithms.," Opt. Express 17, pp. 14771–9, 2009.

[23] Z. Li, L. Stan, D. A. Czaplewski, X. Yang, and J. Gao, "Broadband Infrared Binary-Pattern Metasurface Absorbers with Micro-Genetic Algorithm Optimization," Opt. Lett. 44, pp. 114, 2018.

[24] C. Akturk, M. Karaaslan, E. Ozdemir, V. Ozkaner, F. Dincer, M. Bakir, and Z. Ozer, "Chiral Metamaterial Design Using Optimized Pixelated Inclusions with Genetic Algorithm," Opt. Eng. 54, pp. 035106, 2015.

[25] D.-H. Kwon, P. L. Werner, and D. H. Werner, "Optical Planar Chiral Metamaterial Designs for Strong Circular Dichroism and Polarization Rotation," Opt. Express 16, pp. 11802, 2008.

[26] Q. Hong, T. X. Wu, X. Zhu, R. Lu, and S.-T. Wu, "Designs of Wide-View and Broadband Circular Polarizers," Opt. Express 13, pp. 8318, 2005.

[27] S. Chakravarty, R. Mittra, and N. R. Williams, "Application of a Microgenetic Algorithm (MGA)to the Design of Broad-Band Microwave Absorbers Using Multiple Frequency Selective Surface Screens Buried in Dielectrics," IEEE Trans. Antennas Propag. 50, pp. 284–296, 2002.

[28] T. L. Pu, K. M. Huang, B. Wang, and Y. Yang, "Application of Micro-Genetic Algorithm to the Design of Matched High Gain Patch Antenna with Zero-Refractive-Index Metamaterial Lens," J. Electromagn. Waves Appl. 24, pp. 1207–1215, 2010.

[29] R. L. Olmon, B. Slovick, T. W. Johnson, D. Shelton, S. H. Oh, G. D. Boreman, and M. B. Raschke, "Optical Dielectric Function of Gold," Phys. Rev. B - Condens. Matter Mater. Phys. 86, pp. 235147, 2012.

[30] I. H. Malitson, "Interspecimen Comparison of the Refractive Index of Fused Silica," J. Opt. Soc. Am. 55, pp. 1205–1209, 1965.

[31] J. Hao, L. Zhou, and M. Qiu, "Nearly Total Absorption of Light and Heat Generation by Plasmonic Metamaterials," Phys. Rev. B 83, pp. 165107, 2011.

SECTION

2. CONCLUSION

Various novel optical properties have been realized with the artificially designed metamaterials in terms of enormous design methods and material configurations. In order to facilitate the development and evolution in the field of metamaterial absorbers and emitters, we expect to improve the design methods and explore the physical mechanisms.

This work is featured in three aspects: (1) the simple structure design with aluminum and tungsten materials for the metamaterial absorbers and emitters through periodic structures, (2) engineering the thermal emission properties via the quasi-periodic metal-dielectric multilayer metamaterials, (3) improve the design method beyond the traditional design method toward broadband metasurface absorber and metasurface with giant circular dichroism by the micro genetic algorithm.

We focus on the design of wavelength-selective metamaterial absorbers and emitters which are promising in various applications covering visible and mid-infrared range. Five projects are arranged in the work. In project one, we demonstrate an all-metal structural color printing platform based on aluminum plasmonic metasurfaces using a simple, one-step focused ion beam milling process on aluminum surface. We print image with high resolution and high color performance. The excellent performance is explained as the excitation of plasmonic electric and magnetic dipole resonances.

In project two, wavelength-selective mid-infrared metamaterial absorber and emitter is designed based on single-sized and double-sized unit cells patterns with tungsten cross resonators. We also study the characteristics of absorption and impedance spectra for different unit cell patterns through an equivalent RLC circuit model. At last, we conduct thermal analysis for absorbers and energy conversion efficiency for emitters.

In the third project, we theoretically and experimentally investigate thermal emission properties for three types of metal-dielectric multilayer stacks, Periodic multilayer, Thue-Morse multilayer and Fibonacci multilayer stacks. Moreover, we analyze the dispersion relations of the designed metamaterials in the wave vector resolved space. $\omega_0 - k_z$ dispersion space.

In the project four, we develop the design of the W-Al_2O_3-W three-layer electromagnetic absorber toward broadband applications in the mid-infrared range using genetic algorithm and explain the broadband absorption performance with multiple resonances in the nanostructure.

In the last project, the micro-genetic optimization method is employed to design the binary metasurfaces with strong circular dichroism in the absorption. The excitation and interferences of the modes under LCP and RCP incidence are found to be responsible for the excellent performance.

In summary, through five projects presented in this dissertation, the electromagnetic properties of the metamaterial absorbers and emitters are theoretically and experimentally studied. The designed structures are demonstrated to be feasible and versatile to achieve exciting optical properties toward electrical and optical applications with compact and miniature requirements in future. Therefore, the work is believed to boost the development and promising applications in the field of metamaterials.

BIBLIOGRAPHY

[1] C. M. Watts, X. Liu, and W. J. Padilla, "Metamaterial Electromagnetic Wave Absorbers," Adv. Mater. 24, pp. OP98-120, OP181, 2012.

[2] Y. Cui, Y. He, Y. Jin, F. Ding, L. Yang, Y. Ye, S. Zhong, Y. Lin, and S. He, "Plasmonic and Metamaterial Structures as Electromagnetic Absorbers," Laser Photonics Rev. 8, pp. 495–520, 2014.

[3] http://www.ska-olska.pl/sites/default/files/imagecache/500wys/lab/spectrum.png. Terahertz - to see the invisible," July 2013.

[4] N. I. Landy, S. Sajuyigbe, J. J. Mock, D. R. Smith, and W. J. Padilla, "Perfect Metamaterial Absorber," Phys. Rev. Lett. 100, pp. 1–4, 2008.

[5] X. Liu, T. Starr, A. F. Starr, and W. J. Padilla, "Infrared Spatial and Frequency Selective Metamaterial with Near-Unity Absorbance," Phys. Rev. Lett. 104, 2010.

[6] J. Zhu, Z. Ma, W. Sun, F. Ding, Q. He, L. Zhou, and Y. Ma, "Ultra-Broadband Terahertz Metamaterial Absorber," Appl. Phys. Lett. 105, pp. 021102, 2014.

[7] H. Deng, Z. Li, L. Stan, D. Rosenmann, and D. Czaplewski, "Broadband Perfect Absorber Based on One Ultrathin Layer of Refractory Metal," Opt. Lett. 40, pp. 2592–2595, 2015.

[8] N. T. Q. Hoa, P. D. Tung, P. H. Lam, N. D. Dung, and N. H. Quang, "Numerical Study of an Ultrabroadband, Wide-Angle, Polarization-Insensitivity Metamaterial Absorber in the Visible Region," J. Electron. Mater. 47, pp. 2634–2639, 2018.

[9] K. Yao and Y. Liu, "Plasmonic Metamaterials," Nanotechnol. Rev. 3, pp. 177–210, 2014.

[10] L. P. Wang and Z. M. Zhang, "Wavelength-Selective and Diffuse Emitter Enhanced by Magnetic Polaritons for Thermophotovoltaics," Appl. Phys. Lett. 100, pp. 063902, 2012.

[11] H. Wang and L. Wang, "Perfect Selective Metamaterial Solar Absorbers," Opt. Express 21, pp. A1078–A1093, 2013.

[12] S. Molesky, C. J. Dewalt, and Z. Jacob, "High Temperature Epsilon-near-Zero and Epsilon-near-Pole Metamaterial Emitters for Thermophotovoltaics," Opt. Express 21, pp. A96, 2013.

[13] Y. Jin, S. Xiao, N. A. Mortensen, and S. He, "Arbitrarily Thin Metamaterial Structure for Perfect Absorption and Giant Magnification," Opt. Express 19, pp. 11114, 2011.

[14] J. G. Fleming, S. Y. Lin, I. El-Kady, R. Biswas, and K. M. Ho, "All-Metallic Three-Dimensional Photonic Crytal with a Large Infrared Bandgap," Nature 417, pp. 52–55, 2002.

[15] V. Rinnerbauer, Y. X. Yeng, W. R. Chan, J. J. Senkevich, J. D. Joannopoulos, M. Soljačić, and I. Celanovic, "High-Temperature Stability and Selective Thermal Emission of Polycrystalline Tantalum Photonic Crystals," Opt. Express 21, pp. 11482, 2013.

[16] D. Liu, Y. Gao, A. Tong, and S. Hu, "Absolute Photonic Band Gap in 2D Honeycomb Annular Photonic Crystals," Phys. Lett. Sect. A Gen. At. Solid State Phys. 379, pp. 214–217, 2015.

[17] H. MacHhadani, Y. Kotsar, S. Sakr, M. Tchernycheva, R. Colombelli, J. Mangeney, E. Bellet-Amalric, E. Sarigiannidou, E. Monroy, and F. H. Julien, "Terahertz Intersubband Absorption in GaN/AlGaN Step Quantum Wells," Appl. Phys. Lett. 97, pp. 191101, 2010.

[18] D. Korobkin, Y. A. Urzhumov, B. Neuner, C. Zorman, Z. Zhang, I. D. Mayergoyz, and G. Shvets, "Mid-Infrared Metamaterial Based on Perforated SiC Membrane: Engineering Optical Response Using Surface Phonon Polaritons," Appl. Phys. A Mater. Sci. Process. 88, pp. 605–609, 2007.

[19] R. W. Wood, "XLII. *On a Remarkable Case of Uneven Distribution of Light in a Diffraction Grating Spectrum*," Philos. Mag. Ser. 6 4, pp. 396–402, 1902.

[20] N. Bonod, G. Tayeb, D. Maystre, S. Enoch, and E. Popov, "Total Absorption of Light by Lamellar Metallic Gratings," Opt. Express 16, pp. 15431–15438, 2008.

[21] H. Deng, T. Wang, J. Gao, and X. Yang, "Metamaterial Thermal Emitters Based on Nanowire Cavities for High-Efficiency Thermophotovoltaics," J. Opt. (United Kingdom) 16, 2014.

[22] S. Zhong and S. He, "Ultrathin and Lightweight Microwave Absorbers Made of Mu-near-Zero Metamaterials," Sci. Rep. 3, pp. 2083, 2013.

[23] J.-J. Greffet and M. Nieto-Vesperinas, "Field Theory for Generalized Bidirectional Reflectivity: Derivation of Helmholtz’s Reciprocity Principle and Kirchhoff’s Law," J. Opt. Soc. Am. A 15, pp. 2735, 1998.

[24] H. Peng, Y. Luo, X. Ying, Y. Pu, Y. Jiang, J. Xu, and Z. Liu, "Broadband and Highly Absorbing Multilayer Structure in Mid-Infrared," Appl. Opt. 55, pp. 8833, 2016.

[25] T. Søndergaard, S. M. Novikov, T. Holmgaard, R. L. Eriksen, J. Beermann, Z. Han, K. Pedersen, and S. I. Bozhevolnyi, "Plasmonic Black Gold by Adiabatic Nanofocusing and Absorption of Light in Ultra-Sharp Convex Grooves," Nat. Commun. 3, pp. 969, 2012.

[26] Y. Cui, J. Xu, K. Hung Fung, Y. Jin, A. Kumar, S. He, and N. X. Fang, "A Thin Film Broadband Absorber Based on Multi-Sized Nanoantennas," Appl. Phys. Lett. 99, 2011.

[27] P. Liu and T. Lan, "Wide-Angle, Polarization-Insensitive, and Broadband Metamaterial Absorber Based on Multilayered Metal–Dielectric Structures," Appl. Opt. 56, pp. 4201–4205, 2017.

[28] P. Bouchon, C. Koechlin, F. Pardo, R. Haïdar, and J.-L. Pelouard, "Wideband Omnidirectional Infrared Absorber with a Patchwork of Plasmonic Nanoantennas," Opt. Lett. 37, pp. 1038–1040, 2012.

[29] A. K. Azad, W. J. M. Kort-Kamp, M. Sykora, N. R. Weisse-Bernstein, T. S. Luk, A. J. Taylor, D. A. R. Dalvit, and H. T. Chen, "Metasurface Broadband Solar Absorber," Sci. Rep. 6, pp. 20347, 2016.

[30] F. Ding, Y. Jin, B. Li, H. Cheng, L. Mo, and S. He, "Ultrabroadband Strong Light Absorption Based on Thin Multilayered Metamaterials," Laser Photonics Rev. 8, pp. 946–953, 2014.

[31] D. Ji, H. Song, X. Zeng, H. Hu, K. Liu, N. Zhang, and Q. Gan, "Broadband Absorption Engineering of Hyperbolic Metafilm Patterns," Sci. Rep. 4, pp. 4498, 2014.

[32] K. Kumar, H. Duan, R. S. Hegde, S. C. W. Koh, J. N. Wei, and J. K. W. Yang, "Printing Colour at the Optical Diffraction Limit," Nat. Nanotechnol. 7, pp. 557–561, 2012.

[33] W. Wang, D. Rosenmann, D. A. Czaplewski, X. Yang, and J. Gao, "Realizing Structural Color Generation with Aluminum Plasmonic V-Groove Metasurfaces," Opt. Express 25, pp. 20454–20465, 2017.

[34] E. Rephaeli and S. Fan, "Absorber and Emitter for Solar Thermo-Photovoltaic Systems to Achieve Efficiency Exceeding the Shockley-Queisser Limit," Opt. Express 17, pp. 15145, 2009.

[35] H. Wang, J. Y. Chang, Y. Yang, and L. Wang, "Performance Analysis of Solar Thermophotovoltaic Conversion Enhanced by Selective Metamaterial Absorbers and Emitters," Int. J. Heat Mass Transf. 98, pp. 788–798, 2016.

[36] N. Liu, M. Mesch, T. Weiss, M. Hentschel, and H. Giessen, "Infrared Perfect Absorber and Its Application as Plasmonic Sensor," Nano Lett. 10, pp. 2342–2348, 2010.

[37] K. Chen, R. Adato, and H. Altug, "Dual-Band Perfect Absorber for Multispectral Plasmon-Enhanced Infrared Spectroscopy," ACS Nano 6, pp. 7998–8006, 2012.

[38] M. F. Duarte, M. A. Davenport, D. Takbar, J. N. Laska, T. Sun, K. F. Kelly, and R. G. Baraniuk, "Single-Pixel Imaging via Compressive Sampling: Building Simpler, Smaller, and Less-Expensive Digital Cameras," IEEE Signal Process. Mag. 25, pp. 83–91, 2008.

[39] S. Savo, D. Shrekenhamer, and W. J. Padilla, "Liquid Crystal Metamaterial Absorber Spatial Light Modulator for THz Applications," Adv. Opt. Mater. 2, pp. 275–279, 2014.

VITA

Zhigang Li was born in Xuchang City, Henan province, China. He received his Bachelor of Engineering degree and Master of Engineering degree in Materials Science and Engineering in 2011 and 2014, respectively, from Huazhong University of Science and Technology, Wuhan, China. In July 2019, he received his Doctor of Philosophy in Mechanical Engineering from Missouri University of Science and Technology, Rolla, Missouri, USA. His research focused on nanophotonics and metamaterials design towards applications in energy harvesting by thermovoltaics and infrared sensing, color printing with super resolution at microscale as well as optimization method in nanostructure design.